


Winter 2-23-2019

Development of a Counter-Flow Thermal Gradient Microfluidic Device

Shayan Davani

Follow this and additional works at: <https://digitalcommons.latech.edu/dissertations>

 Part of the [Nanoscience and Nanotechnology Commons](#), [Other Biomedical Engineering and Bioengineering Commons](#), and the [Other Mechanical Engineering Commons](#)

Recommended Citation

Davani, Shayan, "" (2019). *Dissertation*. 17.
<https://digitalcommons.latech.edu/dissertations/17>

This Dissertation is brought to you for free and open access by the Graduate School at Louisiana Tech Digital Commons. It has been accepted for inclusion in Doctoral Dissertations by an authorized administrator of Louisiana Tech Digital Commons. For more information, please contact digitalcommons@latech.edu.

**DEVELOPMENT OF A COUNTER-FLOW THERMAL
GRADIENT MICROFLUIDIC DEVICE**

by

Shayan Davani, M.S.

A Dissertation Presented in Partial Fulfillment
of the Requirements of the Degree
Doctor of Philosophy

COLLEGE OF ENGINEERING AND SCIENCE
LOUISIANA TECH UNIVERSITY

February 2019

LOUISIANA TECH UNIVERSITY
THE GRADUATE SCHOOL

DECEMBER 18, 2018

Date

We hereby recommend that the dissertation prepared under our supervision by
Shayan Davani, M.S.

entitled **Development Of A Counter-Flow Thermal Gradient Microfluidic Device**

be accepted in partial fulfillment of the requirements for the Degree of
Doctor of Philosophy in Engineering

Supervisor of Dissertation Research

Head of Department
Engineering

Department

Recommendation concurred in:

Advisory Committee

Approved:

Director of Graduate Studies

Dean of the College

Approved:

Dean of the Graduate School

ABSTRACT

This work presents a novel counter-flow design for thermal stabilization of microfluidic thermal reactors. In these reactors, precise control of temperature of the liquid sample is achieved by moving the liquid sample through the thermal zones established ideally through the conduction in the solid material of the device. The goal here is to establish a linear thermal distribution when there is no flow and to minimize the temperature change at flow condition. External convection as well as internal flow-induced effects influence the prescribed thermal distribution. The counter-flow thermal gradient device developed in this study is capable of both stabilizing the thermal disturbance caused by the flow as well as establishing a significantly linear distribution. A temperature ramp rate of up to 102 °C/sec was achieved for a 30 ml/hr flow rate. This configuration removes the obstacles in the way of performing temperature sensitive biological processes such as PCR and DNA melt analysis at remarkably shorter time.

Mathematical modeling including the analytical models as well as simulations was performed for a better understanding of the transport phenomena occurring in the designed microfluidic devices. External convection impact on the uniformity and linearity of the thermal distribution and the ways for minimizing it were investigated experimentally, analytically, and numerically. Also, the dissipation of a small thermal event generated from an exothermic mixing in a continuous flow thermal sensing system

was investigated, and a novel numerical model was developed for suggesting the optimum location for sensing the heat using a thermoelectric sensor.

APPROVAL FOR SCHOLARLY DISSEMINATION

The author grants to the Prescott Memorial Library of Louisiana Tech University the right to reproduce, by appropriate methods, upon request, any or all portions of this Dissertation. It is understood that “proper request” consists of the agreement, on the part of the requesting party, that said reproduction is for his personal use and that subsequent reproduction will not occur without written approval of the author of this Dissertation. Further, any portions of the Dissertation used in books, papers, and other works must be appropriately referenced to this Dissertation.

Finally, the author of this Dissertation reserves the right to publish freely, in the literature, at any time, any or all portions of this Dissertation.

Author _____

Date _____

DEDICATION

I would like to dedicate my dissertation to my family and many friends. I wish to express special gratitude to my dear wife, Farnaz who not only supported me but also contributed a lot to this work.

Finally I would like to dedicate this work to my dear parents who have constantly supported me throughout these years.

TABLE OF CONTENTS

ABSTRACT	iii
APPROVAL FOR SCHOLARLY DISSEMINATION	v
DEDICATION	vi
LIST OF FIGURES	xii
LIST OF TABLES	xix
ACKNOWLEDGMENTS	xx
CHAPTER 1 INTRODUCTION	1
1.1 Precision Microfluidic Temperature Control via Spatial Thermal Non-uniformities	2
1.2 Thermal Uncertainty Due to Gradient Non-linearity	3
1.3 Thermal Uncertainty Due to Internal Advection Caused by Flow	5
1.4 Advantages of Linear Thermal Gradient	6
1.5 Applications of Thermal Gradient Microfluidic Temperature Control	6
1.5.1 Continuous-Flow PCR	6
1.5.2 Continuous-Flow Melt Analysis	7
1.5.3 Iso-flux Calorimetry	8
1.6 Overview	8
CHAPTER 2 CONVECTION EFFECT ON PERFORMANCE OF THE THERMAL GRADIENT CHIP	11
2.1 Introduction	12
2.2 Analytical Solution	15
2.3 Natural convection	24

2.3.1	Theory	24
2.3.2	Experiment	26
2.3.3	Temperature dependency of natural convection coefficient	29
2.3.4	Pressure dependency of natural convection coefficient	31
2.4	Conclusion	34
CHAPTER 3 DETECTING THERMAL ASYMMETRY IN MICROFLUIDICS FOR SENSOR APPLICATIONS: CRITICAL DESIGN CONSIDERATIONS AND OPTIMIZATION		36
3.1	Introduction.....	37
3.2	Experimental Methods	39
3.2.1	Microfluidic Device Fabrication	40
3.2.2	Thermopile Sensor Fabrication	41
3.2.3	Experimental Setup	42
3.2.4	Experimental Procedure	43
3.3	Numerical Simulation	44
3.3.1	Model Geometry.....	44
3.3.2	Governing Equations.....	45
3.3.3	Boundary Conditions	48
3.3.4	Analysis of Numerical Results	49
3.4	Results and Discussion.....	50
3.4.1	Shifting the Mixing Location by Adjusting the Flow Ratios	50
3.4.2	Bolus Mixing	51
3.4.3	Continuous Mixing for a Steady State Response	52
3.4.4	Validation of the Numerical Model	53
3.4.5	The Relationship between Flow Rate and Optimum Thermopile Location ..	55
3.4.6	Effect of Flow Ratio.....	60

3.5	Conclusion	62
CHAPTER 4 3-D NUMERICAL SOLUTION OF EXOTHERMIC MIXING OF WATER/ETHANOL IN Y-SHAPED MICROCHANNELS		64
4.1	Introduction.....	64
4.2	Methods.....	68
4.2.1	Heat of Mixing.....	68
4.2.2	Viscosity and Density	72
4.3	Discussion	73
4.3.1	Sources of Asymmetry	73
4.4	Conclusion	77
CHAPTER 5 COUNTER-FLOW THERMAL GRADIENT MICROFLUIDIC DEVICE FOR THERMAL STABILIZATION		79
5.1	Introduction.....	79
5.1.1	Flow-induced Effects	79
5.2	Analytical Approach	83
5.2.1	1-D Analytical Model	83
5.2.1.1	Boundary conditions.....	86
5.2.1.2	Results and discussions	87
5.3	Design and Fabrication of a Counter-flow Chip	91
5.3.1	Design	92
5.3.1.1	Chip Design.....	92
5.3.1.2	Microchannel Design.....	93
5.3.1.3	Photomask	96
5.3.2	Hard Mask Fabrication.....	98
5.3.3	Photolithography	99
5.3.4	KOH Wet Etching	101

5.3.4.1	Wet etching set-up	103
5.3.4.2	Outcome	104
5.3.4.3	Residual hard mask removal	107
5.3.5	Chip Assembly	107
5.3.5.1	Bonding techniques	109
5.3.5.2	Wafer dicing.....	111
5.3.5.3	Chip bonding using SU-8.....	111
5.3.5.4	Attachment of inlets and outlets	115
5.4	Thermal Gradient Experiment	116
5.4.1	Experimental Set Up and Procedure	117
5.5	Experimental Results.....	122
5.5.1	Ramp Rate.....	122
5.5.2	IR Thermal Data Analysis	122
5.5.3	Linearity of the Distributions	123
5.5.4	Regional Temperature Variation due to Flow	126
5.6	Conclusion	130
CHAPTER 6 COUNTER-FLOW 3-D SIMULATION.....		131
6.1	Introduction.....	131
6.2	Governing Equations.....	134
6.3	Model Geometry.....	135
6.4	Boundary Conditions.....	137
6.5	Validation.....	139
6.5.1	Validation Procedure.....	139
6.5.2	Thermal Contours.....	140
6.5.3	Centerline Temperature.....	143

6.6	Results and discussion.....	144
6.6.1	Constant T Instead of Constant Q	144
6.6.2	Temperature in the Layers of the Chip	146
6.6.3	Thermal Distribution in the Depth	149
6.6.4	The Optimum Flow Rate for the Highest Signal.....	152
6.7	Conclusion	154
CHAPTER 7 CONCLUSION AND FUTURE WORK.....		155
7.1	Conclusion	155
7.1.1	Achievements	155
7.2	Future Work.....	156
APPENDIX A MATLAB CODE FOR 1-D COUNTER-FLOW MODEL		159
BIBLIOGRAPHY		161

LIST OF FIGURES

Figure 2-1: Schematic of the thermal gradient set up consisting of heater 1 set at 120 °C, a glass microfluidic chip, and heater 2 set at 45 °C.	14
Figure 2-2: IR image of the set up under thermal gradient generated by two heaters set at 120 °C and 45 °C plotted for three ROIs denoted by lines 3,4, and 5.	14
Figure 2-3: Temperature distribution due to pure conduction (top) compared to a distribution due to both conduction and convection (bottom). Simulation result was used.	15
Figure 2-4: Schematic of the geometry and the differential control volume defined for applying the conservation of energy on a rectangular prism.....	16
Figure 2-5: Comparison between the results of analytical model and the 3-D model. Temperature was evaluated at x=5mm in y direction.	19
Figure 2-6: Four categories of thermal gradient affected by external convection: a) $h_1=1, h_2=1 \text{ W/m}^2\cdot\text{K}$ b) $h_1=20, h_2=1 \text{ W/m}^2\cdot\text{K}$ c) $h_1=20, h_2=20 \text{ W/m}^2\cdot\text{K}$ d) $h_1=1, h_2=20 \text{ W/m}^2\cdot\text{K}$	20
Figure 2-7: Four categories of thermal gradient affected by external convection: a) $h_1=1, h_2=1 \text{ W/m}^2\cdot\text{K}$ b) $h_1=20, h_2=1 \text{ W/m}^2\cdot\text{K}$ c) $h_1=20, h_2=20 \text{ W/m}^2\cdot\text{K}$ d) $h_1=1, h_2=20 \text{ W/m}^2\cdot\text{K}$	21
Figure 2-8: Temperature distribution along the centerline of the chip plotted for the convection coefficients of 0, 10, 25, and 50 $\text{W/m}^2\cdot\text{K}$. The abscissa here refers to the x-direction as indicated in x-axis here refers to Figure 2-3.	22
Figure 2-9: Impact of convection coefficient on the size of PCR window and its location. The red and blue color corresponds to the location of average $T=95 \text{ }^\circ\text{C}$ and $T=60 \text{ }^\circ\text{C}$ respectively. Distance between the location of these temperatures is defined by parameter L at no convection and parameter L', under the convection. Right axis denotes the ratio L'/L demonstrating the impact of h on PCR window.	23
Figure 2-10: Actual IR images showing the PCR window for a chip inside and outside an enclosure	24

Figure 2-11: Picture of set up used for measuring the natural convection coefficient under vacuum. The cylindrical aluminum block is mounted on a solid PDMS pad by a thin plastic rod (in order to reduce conduction). Two thermocouples are attached to the data logger: one measures the ambient temperature, and the other one measures the temperature of the block.	27
Figure 2-12: dimensionless temperature of the block over time for normal pressure, a moderate vacuum (1000 milliTorr) and a higher vacuum level (300 milliTorr).....	28
Figure 2-13: Experimental and numerical results for the gradual cooling of a cylindrical block oriented vertically due to natural convection.	30
Figure 2-14: Analytical, experimental, and simulation results for temperature dependency of convection coefficient around a heated vertical cylindrical block.	31
Figure 2-15: Convection coefficient on a vertical wall as a function of pressure evaluated by simulation and Equation 2-32	32
Figure 2-16: Thermal contours around the heated cylinder at normal pressure and 300 milliTorr	33
Figure 3-1: (a) Diagram of the microfluidic device fabrication. The microchannel is formed by sandwiching a patterned polymer tape between two glass blanks. PDMS ports are added where tubing will connect to the inlets/outlet of the microchannel. The thermopile is placed on the exterior of the device, opposite the flow channel (b) Photo of a Sb/Bi thermopile used for these experiments. (c) Photo of an assembled device.	41
Figure 3-2: The dimensions and materials of the conjugate heat transfer model developed in Fluent. This orientation is inverted from the orientation shown in Fig 3-1a and 3-1c	45
Figure 3-3: Photographs of three images of different flow configurations within the microchannel. Coloring dye and image enhancing was used to better visualize the flow streams. The images on the left are photos of a microfluidic device without the thermopile; those on the right are of a device with a thermopile positioned as in Figure 3-1c . These latter photos are high-zoom to show the thermopile detail with respect to the liquid flows.	51
Figure 3-4: Thermopile output for a bolus injection of ethanol.....	52
Figure 3-5: For the continuous-mixing experiments, the two inlet syringe pumps were programmed to change the flow ratios of the two liquid streams and regular intervals. For this thermopile output data shown here, the total volumetric flow rate for both streams combined was 200 $\mu\text{l}/\text{min}$	53

- Figure 3-6:** Representative results from the numerical simulations of the water/ethanol mixing. (a) shows the concentration distribution, and (b) shows the temperature distribution for the specific case of W4:E1 @ 400 $\mu\text{l}/\text{min}$ total volumetric flow.54
- Figure 3-7:** A comparison between the Y-junction flow interfaces for a W4:E1 flow ratio for the numerical (detail from **Figure 3-6a**) and the experimental (detail from **Figure 3-3**) results reveals strong qualitative correlation.54
- Figure 3-8:** A comparison between the numerical and experimental results for four flow ratios at each of three flow rates (12 total combinations). Each graph corresponds to a specific total volumetric flow rate (W+E); each curve within each graph corresponds to a different flow ratio. The discrete points indicate the experimental data; the dotted/dashed lines indicate the corresponding numerical data. To filter out the effect of baseline drift in the experimental data (observable in **Figure 3-5**), the y-axes for these graphs define 0mV to be the W1:E1 condition (for both the experimental and numerical results). To compare the rise times for all conditions, the x-axes for these graphs define 0s as the last moment of stabilized W1:E1 voltage before changing to its new stabilized voltage at a different flow ratio (e.g. 196, 436, 675, and 915 seconds in **Figure 3-5**).55
- Figure 3-9:** The predicted thermopile voltage for two highly asymmetric flows (W1:E4 and W4:E1) as a function of thermopile position along the microchannel. The x-axis denotes the distance between the center of the thermopile (which is 10 mm in length) and the base of the Y-junction channel where the two streams first meet.56
- Figure 3-10:** For each of these six representative flow ratios, the left-hand vertical axis indicates the maximum voltage as a function of flow rate; the right-hand vertical axis indicates where within the channel the thermopile must be to measure this maximum voltage.58
- Figure 3-11:** Comparison between the predicted thermopile voltage as a function of flow rate for two thermopile locations. The optimum configuration for low flow rates (<600 $\mu\text{l}/\text{min}$) has the center of the thermopile located only 1.5 mm downstream from the Y-junction. The inset reveals the linear relationship between the signal and flow rate at low flows. The flow ratio for this simulation is W1:E4.60
- Figure 3-12:** Thermopile voltage as a function of flow ratio, for several flow rates (W+E). When the mixing interface is shifted toward the water inlet, the voltage will be more positive; toward the ethanol inlet, more negative.61
- Figure 4-1:** a) The schematic of the transition in the structure of water/ethanol mixture (schematics were reproduced from [49] b) enthalpy of mixing based on the sixth order fitted equation of Peeters.69

Figure 4-2: Temperature difference between two lines overlaying the thermopile location calculated using enthalpy modification (dashed lines) and source term (dotted lines with markers) for different ratios of water and ethanol. The temperature difference was plotted all along the channel (as indicated in Figure 3-2).	70
Figure 4-3: Enthalpy of mixing plotted at different sections of the channel.....	71
Figure 4-4: Source term corresponding to the heat of mixing, plotted at different sections of the channel.	72
Figure 4-5: Viscosity and density of the mixture as a function of ethanol mass fraction (figure reproduced from Mauri).	73
Figure 4-6: Impact of reversing the factors accounting for the asymmetry in the temperature of the co-flow. Again, temperature difference between two lines overlaying the thermopile location was plotted over the length of the channel.....	75
Figure 4-7: Thermal contour of the microchannel chip when the source term is defined in a way that its pick is toward the ethanol side (water and ethanol sides are as demonstrated in Figure 3-2).	77
Figure 5-1: Geometry of the microchannel from the model depicting the pattern and its location with respect to the two heaters. a) side view b) front view [2]	81
Figure 5-2: Schematic of the 1-D model	84
Figure 5-3: Temperature of each layer is dictated by the 1-D conduction when the heater is attached to one end.....	87
Figure 5-4: Thermal distribution in the glass/silicon counter-flow model at 10ml/hr from analytical and simulation plotted for different layers (wall 1, channel 1, interface, channel 2, wall 2). The right picture is magnified.	89
Figure 5-5: Thermal distribution of the layers along a glass/quartz counter-flow under no flow, flow of 10 ml/hr, and 20 ml/hr	90
Figure 5-6: Thermal distribution of the layers along a glass/silicon counter-flow under no flow, flow at 10ml/hr and, 20ml/hr	91
Figure 5-7: Impact of the width on the temperature difference between two fixed points.....	93
Figure 5-8: Schematic of two microfluidic designs for the thermoelectric sensing a) merging b) parallel	94
Figure 5-9: a) Front side of the chip b) Back side of the chip.....	95

Figure 5-10: Photomask layout including the final pattern (plotted in green color) and the guidelines.....	97
Figure 5-11: Alignment marks designed in a large and a small set	98
Figure 5-12: Wafer with the patterned oxide as the hard mask. The bluish color shows the oxide and the gray color represents the silicon	101
Figure 5-13: KOH wet etching set up.....	104
Figure 5-14: A 3-D microscope image of the etched channel on front the side of the wafer. Top picture shows the top view of the etched channel (maximum height demonstrated by red color, minimum by dark blue). The bottom picture shows the profile of the etched channel probed along line 1 shown in the top picture. The difference between the highest and the lowest depth is about 68 μm	105
Figure 5-15: 3-D microscope image of the etched channel on the back side of the wafer. The two parallel thick black lines in the top picture show the anisotropic walls of the etched channel. The roughness of the etched surface of the channel can be seen in the top view. The profile of the probed line 1 is shown in the bottom picture. The etch depth is about 55 μm	106
Figure 5-16: Schematic of the two contact imprinting methods for transferring SU-8 to an etched surface [95].....	113
Figure 5-17: Picture of the setup used for GS experiment. The heat sink in ice/water was used to sink the heat and generate a gradient of 40 $^{\circ}\text{C}/\text{chip}$	118
Figure 5-18: Temporal plot of an ROI in the GQDF experiment. Flow rates of 1, 2, 4, ... 20 ml/hr were used in each syringe pumps. The system is approximately in steady-state when the curve plateaus.	119
Figure 5-19: Temporal plot of an ROI in the GQCF experiment. Flow rates of 2, 4, 6, ... , 20 ml/hr were used in each syringe pumps.	121
Figure 5-20: Schematic of the areas defined for the linearity measure. The 20 mm "parallel flow region" is where the results are evaluated in this chapter.	124
Figure 5-21: Linearity measure for GGCF and GGDF at different flow rates evaluated at the centerline of the parallel region (Figure 5-20)	124
Figure 5-22: Linearity measure for GQCF and GQDF at different flow rates	125
Figure 5-23: Linearity measure for GGCF and GGDF at different flow rates	125
Figure 5-24: Temperature difference map between the 10 ml/hr flow rate and no plotted for GGDF and GGCF chips from the IR data. The maximum decrease of each chip is shown by arrows pointing to the color bar.	126

Figure 5-25: Temperature difference between the flow condition of 20 ml/hr and the no flow condition plotted from the IR data of the six configurations. The same colormap was used for all the chips for better comparison.	127
Figure 5-26: Temperature change due to flow evaluated at different regions. ΔT was evaluated at a 4 mm square located on bottom, middle, and top marked by \diamond bottom, * middle, and \circ top respectively as demonstrated on top figure	129
Figure 6-1: CAD of the microfluidic chip with heater attached on back, plotted in the SpaceClaim (Ansys, PA, USA). The orange strip on top is the heater. Bottom figure shows the cross section of the chip at the channels proximity.	136
Figure 6-2: Meshed geometry in the Gambit (Fluent®, PA, USA)	137
Figure 6-3: Thermal gradient of the exterior surface of the GGCF chip (top surface of Figure 6-1) when there is no flow (left) Simulation (right) Experimental.....	140
Figure 6-4: Thermal gradient of the exterior surface of the GGCF chip when there is no flow (left) Simulation (right) Experimental	140
Figure 6-5: Thermal gradient of exterior surface of the GGDF chip affected by flow at 10 ml/hr (left) Simulation (right) Experimental	141
Figure 6-6: Thermal gradient of exterior surface of the GQCF chip when there is no flow (left) Simulation (right) Experimental.....	141
Figure 6-7: Thermal gradient of exterior surface of the GQCF chip affected by flow at 10 ml/hr (left) Simulation (right) Experimental	142
Figure 6-8: Thermal gradient of exterior surface of the GQDF chip affected by flow at 10 ml/hr (left) Simulation (right) Experimental	142
Figure 6-9: Thermal gradient of exterior surface of the GSCF chip when there is no flow (left) Simulation (right) Experimental.....	142
Figure 6-10: Thermal gradient of exterior surface of the GSCF chip affected by flow at 10 ml/hr (left) Simulation (right) Experimental	143
Figure 6-11: Thermal gradient of exterior surface of the GSDF chip affected by flow at 10 ml/hr (left) Simulation (right) Experimental	143
Figure 6-12: Temperature along the centerline of GGCF chips from the simulation and experimental plotted for (left) No flow (right) 10 ml/hr plotted along the centerline of the exterior surface in the y-direction indicated in Figure 6-1	144
Figure 6-13: Temperature along the centerline of GGDF chips from the simulation and experimental plotted for (left) No flow (right) 10 ml/hr plotted along the centerline of the exterior surface in y-direction as indicated in Figure 6-1	144

- Figure 6-14:** Comparison between the constant temperature and constant heat flux condition under the flow of 10ml/hr (left) GGDF and (right) GGCF. The temperature profile was plotted along the centerline of the exterior surface of the chip (y-direction) as indicated in **Figure 6-1** 145
- Figure 6-15:** Thermal distribution of the GGCF layers plotted along the centerline of the layers of the chip (in y-direction) passing the middle of each layer (as indicated in **Figure 6-1**) for flow rates of (left)10ml/hr (right) 20ml/hr 147
- Figure 6-16:** Thermal distribution of the GSCF layers plotted along the centerline of the layers of the chip (in y-direction) passing the middle of each layer (as indicated in **Figure 6-1**) for flow rates of (left)10ml/hr (right) 20ml/hr 147
- Figure 6-17:** Thermal distribution of the GGCF layers plotted along the channel line (indicated and showed in **Figure 6-1**) instead of the centerline in y-direction, for flow rates of 10ml/hr (left) and 20ml/hr (right) 148
- Figure 6-18:** Thermal distribution of the GSCF layers plotted along the channel line (indicated and showed in **Figure 6-1**) instead of the centerline in y-direction, for flow rates of 10ml/hr (left) and 20ml/hr (right) 149
- Figure 6-19:** Thermal distribution of the GSCF in the depth of the chip (z direction in **Figure 6-1**) plotted over different flow rates 150
- Figure 6-20:** Thermal distribution of the GGCF in the depth of the chip (z direction in **Figure 6-1**) plotted over different flow rates 150

LIST OF TABLES

Table 4-1: Material properties of water and ethanol	74
Table 5-1: Material properties of common candidates for microfluidic fabrication	109
Table 5-2: Summary of the three type of microfluidic chip fabricated and used in this study	117
Table 6-1: ΔT_{ch} evaluated for GG and GS chips at different flow rates.	151

ACKNOWLEDGMENTS

I would like to acknowledge my advisor, Dr Niel Crews, from whom I learned a lot in many ways. I admire the way he builds excellent relationships with his students based on true friendship. Our weekly meetings and conversations about many topics (science, engineering, politics, culture ...) have always been one of the most pleasurable moments for me during these five years.

I would like to thank Davis Bailey, who spent a lot of time answering my questions so patiently and generously. I appreciate all the technical assistance I received from him during the fabrication phase. I would also like to thank Mr Chapman for his exceptional enthusiasm in delivering his knowledge and expertise.

Finally, I thank all my lab mates: Collin Tranter, Varun Kopparchy, Gergana Nestrova, Thomas Holland and my committee members: Dr Leland Weiss, Dr ShengnianWang, Dr Arden Moore, and Dr Bryant Hollins.

CHAPTER 1

INTRODUCTION

The focus of this study is on improving the thermal performance of a microflow thermal reactor. Such a class of reactors works under the following principle: fluids flowing through a microchannel experience heating and/or cooling by contact with the solid walls, which are maintained under a precisely controlled spatial temperature distribution. A complex medley of thermal effects contributes to this performance, such as conduction through the solid material in which the microchannel is embedded, ambient convection around the microdevice, and advection/convection/conduction inside the microchannels. The focus of this project contains two parts: #1) achieving a known and controllable linear temperature distribution across the microchannel region of the microdevice that is stable in time under no-flow conditions, and #2) predicting and minimizing any changes in this temperature distribution caused by microchannel flow.

The emergence of microfluidics is a product of the miniaturization technologies developed originally for the semiconductor industry. Microfluidic processing methods and technologies have been embraced especially in the biological and chemical fields for operational advantages such as the reduced sample size and the superior control over the fluid handling. However the development was not limited only to improving these aspects, but also in the integration of microfluidics with other proportionally miniaturized components toward the direction of developing small systems and subsequently portable

devices capable of performing multiple tasks. Lab-on-a-chip devices are a representative of this class resembling a small laboratory for performing the biological or chemical processes and analyzing the outcome. Although the excellent control over the flow and transport of mass due to the small size and the laminar nature of the flow seem to be the most fascinating characteristic of microfluidics, precise control over the temperature of the fluid is a crucial part of many biomedical and chemical applications. Unfortunately, the impact of flow-induced effects has been largely ignored within the scientific community, although this can be quite severe depending on the thermal properties of the materials used in lab-on-a-chip devices. This prevailing ignorance is likely due to the difficulty of observing microscale thermal behavior, as well as the false assumption that fluid flow at the microscale does not influence the broad thermal state of the microsystem.

1.1 Precision Microfluidic Temperature Control via Spatial Thermal Non-uniformities

Suppose that a plug of fluid with infinite thermal diffusivity and no internal heat generation is flowing through a channel (or pipe) with velocity \vec{V} , and that the channel walls experience a steady-state temperature field $T_s(\vec{r})$. The temperature of the liquid is going to be the same as the temperature of the field. The temperature of the liquid and its temporal change are:

$$T_f = T_s \quad \& \quad \frac{dT_f}{dt} = \vec{V} \cdot \nabla T_s \quad \text{Eq. 1-1}$$

So, instead of heating the fluid and waiting for the equilibrium to be achieved, one can induce a rapid thermal change by either moving the fluid at a very high flow rate or

moving it at lower velocity but in a steeper thermal gradient. Thus, information about the local temperature of the field does not by itself provide the temperature of the fluids, but it defines the temporal temperature change when the velocity is known as well. This is the idea behind the spatial heating of a flowing liquid. Therefore, precise control over the temperature map along with the precise control over the velocity (both magnitude and direction) allows the precise control over the temperature of the fluid.

1.2 Thermal Uncertainty Due to Gradient Non-linearity

In practice, the temperature field will be comprised of either:

- isothermal zones of dissimilar temperatures with gradients between them, or
- one or more gradient zones, with no isothermal regions.

The small size of the microfluidic chips allows rapid and customized thermal distribution in the solid, and also makes it challenging to characterize the local temperature distribution. For this reason, a complex thermal distribution in the solid makes it difficult to predict or measure the local temperature of the fluid. The simplest multi-temperature configuration is a single linear (in 1D) thermal gradient. This not only reduces the complexity of quantifying the temperature with precision at even the sub-millimeter scale, but also implies simple and known boundary conditions to the fluid: constant temperature, when the fluid moves normally to the gradient and constant heat flux when the fluid moves parallel to the gradient.

Theoretically, a steady-state linear thermal gradient can be established by attaching two heaters to the two ends of a solid block. However, the ideal linear gradient can be distorted when the material is exposed to the external convection. The extent of this distortion can be evaluated using the non-dimensional Biot number:

$$Bi \equiv \frac{\text{convection}}{\text{conduction}} = \frac{hL}{k} \quad \text{Eq. 1-2}$$

where, h is the convection coefficient, L is the characteristic length, and k is the thermal conductivity of the solid. For $Bi \ll 1$, the thermal distribution is predominantly governed by the conduction resulting in a linear thermal gradient.

Additionally, the condition described in the previous section 1.1 is an ideal scenario considering the fluid as a 1-D entity; in reality, the thermal conductivity of most fluids is low ($0.6 \text{ w/m}^2 \cdot \text{K}$ for water) and therefore, the assumption of uniform distribution is not valid even at the low-velocity laminar flow. Furthermore, under flow conditions, the physical properties of the fluid, its velocity, thermal boundary condition and even the distance from the inlet of the channel all contribute to a 2-D or 3-D thermal distribution in the flow. The temperature of the fluid in contact with the channel wall is the same as the local temperature of the wall dictated by the thermal field. However, the temperature of the fluid within the channel but NOT in contact with the wall is different. This is due to both the velocity profile and the slow molecular diffusion in the cross section of the channel. The impactful parameters for the distribution of the fluid can be evaluated from the fully-developed solution of internal flow in a circular channel with constant Q boundary condition [1]:

$$T_m = T_s - \frac{11}{48} \frac{u_m r_0^2}{\alpha} \left(\frac{dT_m}{dx} \right) \quad \text{Eq. 1-3}$$

where T_s is the wall temperature (solid temperature), u_m and T_m are the mean velocity and mean temperature of the flow, and α is the fluid thermal diffusivity. This equation suggests that the temperature variation within a cross-section of the channel is small when the mean velocity is low, thermal diffusivity α is high, or the hydraulic diameter of

the channel is small. Thus, the miniaturization of the flow path through the implementation of microfluidic devices and technologies provides significant thermal control and stability. However, the degree to which miniaturization can be achieved remains limited by any manufacturing constraints as well as any interface issues with the other fluidic or detection elements of the system.

Despite all the imperfections, as long as the temperature field is stable and known, a sample fluid experiences a stable but non-linear spatial temperature as it travels in the microchannel.

1.3 Thermal Uncertainty Due to Internal Advection Caused by Flow

In all the analysis described in the section 1.2 and 1.3, the assumption was that the temperature of the microfluidic device (solid substrate) is not affected by the flow. This assumption is reasonable when the thermal mass of the fluid is very small (e.g. a plug of fluid in the channel) as long as the substrate has a high thermal conductivity. However, this is not typical among microfluidic devices and particularly in biomedical microfluidic applications. Therefore, it is important to consider the mutual influence of the fluid on the solid as well as the solid on the fluid. The importance of the fluid increases with the flow rate. The impact of the fluid on distortion of the solid thermal distribution was demonstrated both experimentally and numerically by Crews et al [2]. They also showed that counter-flow configuration can reduce this effect. Thomas et al [3] conducted a parametric study to investigate the important operational parameters on a continuous flow thermal gradient with a serpentine microchannel of 500 x 500 μm cross section. They demonstrated that flow rate is the most significant factor that affects the thermal stability of the device.

1.4 Advantages of Linear Thermal Gradient

Microfluidic thermal reactors are commonly designed with varied thermal zone configurations. The focus of this dissertation is on the configuration that consists of a single thermal zone characterized by a steady-state and linear 1-dimensional (1-D) temperature gradient. This is considered the most desirable for the following three reasons:

1. Fluid flowing with a constant velocity with respect to the orientation of a linear thermal gradient will experience iso-flux heat transfer. Other than the conventional quasi-equilibrium case, which is either slow or inaccurate (never neither), iso-flux heat transfer is the only case that can be solved analytically.
2. A linear thermal distribution is the most predictable spatial thermal map. Being linear, the temperature at any location within the microdevice can be interpolated with high precision from only two embedded temperature sensors that bind the region of interest. This is especially important when fluorescence imaging techniques are integrated with the thermal map of the device [4].
3. A linear gradient is the widest thermal distribution that can be established through conduction (without internal heat generation). Such a distribution allows maximum usage of the microfluidic chip and is of particular importance when optical characterization techniques are involved.

1.5 Applications of Thermal Gradient Microfluidic Temperature Control

1.5.1 Continuous-Flow PCR

The polymerase chain reaction (PCR) is the most universal laboratory process in the field of molecular biology. PCR is a biological reaction for amplifying the DNA. PCR

can be done within microscale thermal reactors at a dramatically shorter time due to intrinsic advantages of microfluidics. It can be performed on well-based or on continuous flow PCR chips [5]. Continuous-flow PCR was first developed on a microfluidic chip by Kopp et al. [6]. Three heaters were used to maintain three isothermal zones. Other researchers modified this system by using different geometry [7] or chip material [8]. Cross talk between different thermal zones is the major problem with this design, as it restricts further device miniaturization and also cannot abide high flow rates [2, 5]. In other words, isolating different temperature zones is challenging and not ideal.

In contrast, Crews et al. [9] took advantage of the cross talk between the different zones by designing a single thermal zone controlled by two heaters, thereby dismissing the need for isolation and additional heater control. Moreover, customized thermal ramp rates consistent with the kinetic of each PCR step was achieved through the smart design of the microchannel (defining the relative velocity of the fluid with respect to the gradient).

1.5.2 Continuous-Flow Melt Analysis

The integration of analytical components and these microfluidic devices is a fundamental aspect of lab-on-a-chip system development. For example, Lagally et al. have integrated capillary electrophoresis to analyze the PCR product [10]; Nakayama et al. have used fluorescence imaging technique to characterize the amplification result of the PCR on chip [11]; For spatial PCR – which can occur an order of magnitude faster due to the gradient thermocycling – the analysis of the PCR product can be achieved only if the fluorescent and the thermal map of the microdevice are correlated. Crews et al. [4]

performed the simultaneous PCR and melt analysis during the DNA amplification by continuously observing the fluorescence and correlating the temperature/fluorescence at each cycle. This "spatial" melt analysis is the alternative of time-domain melt analysis [12] realized only by accurate spatial thermal heating of the fluid in the thermal gradient system.

1.5.3 Iso-flux Calorimetry

The concept of a stable linear thermal gradient is a key step toward the realization of a microfluidic calorimeter that has the ability of sensing a small thermal event taking place within a large thermal gradient. The distinct anisotropic design of a thin-film thermoelectric sensor proposed and applied by Crews et al. [13] has proven such a capability. Thin film thermopile sensors are MEMS sensors operating based on the Seebeck effect, and they convert the temperature difference between each pair of junctions to voltage. The proposed sensor is blind to symmetrical thermal variations caused by either large thermal gradients which are generated intentionally, or any unwanted disturbance as long as it affects the reference and measuring junctions similarly. Such common-mode signal rejection is achieved simply by positioning the junction pairs parallel to the isothermal lines.

1.6 Overview

In Chapter 2, a microfluidic thermal gradient chip is treated as a solid block subject to a thermal gradient by two heaters attached from top and bottom without considering the microchannel resembling the actual device under no flow condition. After understanding the physics of the problem by presenting a powerful analytical solution along with the IR thermography of the actual chip, attempts will be performed to

minimize the external convection as the main source of disturbing the linear thermal gradient. Experimental, 3-D modeling, and analytical relationships will be used to evaluate the practical limits for reducing the convection and presenting the guidelines.

In Chapter 3, a continuous flow microfluidic thermal sensor detecting the heat of mixing generated at the interface of two laminar side-by-side flows using the anisotropic thermoelectric sensor is studied experimentally and numerically. The impact of the operational parameters such as flow ratio between the two streams and flow rate in generating the thermal asymmetry is investigated. The entirety of chapter 3 has been accepted in *International Journal of Heat and Mass Transfer* with Varun Koppa and Niel Crews. Chapter 4 supplements Chapter 3 with deeper theoretical investigation of the transport phenomena occurring in the microchannel exploring the conditions for thermal symmetry (the equivalent of zero voltage in the thermal sensor). The argument made in this chapter is a justification of the final design of the "counter-flow thermal gradient microfluidic chip" which is the subject of Chapter 5 and Chapter 6.

In Chapter 5, the concept of counter-flow microfluidic for minimizing the flow-induced disturbance in the thermal gradient is explained. Design and fabrication of hybrid counter-flow thermal gradient devices is explained. Performance of the counter-flow is compared with the non counter-flow design over a wide range of flow rates and for three materials representing three levels of thermal conductivity.

The counter-flow designed for the thermal stability of the microfluidic devices is a novel design, and to the knowledge of the author, there is no other work dedicated to it to this date. The idea of counter-flow heat exchangers is mature in both science and technology; moreover, the miniaturized heat exchanger for the enhanced heat transfer

from a solid surface using a working fluid has been an active field of research from the emergence of the microfluidics. However, the usage of the microfluidic counter-flow and consequently the design proposed in this study differ *fundamentally* from what has been done in the literature. This is because prior methods have focused on temperature *change* rather than temperature *stabilization*. Here, the designed thermal map is a temperature gradient, and the counter-flow is used to eliminate thermal advection. Other novel features of this research include an intentional non-zero thermal resistance between the counter-flow channels (in order to maintain the axial gradient with low power) and also constraining the heat transfer between counter-flow channels to just a single dimension. Moreover, the 2.5 D geometry of the microfluidic device (which is probably the most common geometry in the microfluidic reactors) raises fundamental heat transfer questions that have not been answered before.

In Chapter 6, the microfluidic devices of Chapter 5 are simulated, and the results are validated with the IR thermography data of the actual devices. The devices are then investigated under other operating conditions. Also, thermal distribution inside the chip including the flow channels is analyzed.

CHAPTER 2

CONVECTION EFFECT ON PERFORMANCE OF THE THERMAL GRADIENT CHIP

The objective of this chapter is to study the effect of pressure on convective heat transfer in mesoscale microfluidic systems. First, an analytical solution will be developed to demonstrate the adverse impact of convection coefficient on the temperature distribution in a mesoscale thermal gradient chip. Scale analysis was performed to deduct the role of pressure in reducing the convection coefficient. Comprehensive simulations were performed to achieve further understanding of the role of pressure. The proposed numerical model was validated by comparing simulated with experimental results for the classic natural convection problem of an isothermal vertical cylinder. Our results agree with those of other researchers who have used analytic, semi-analytic methods [1, 14] for a wide range of Rayleigh numbers. However, analytical solutions are based on some assumptions and simplifications that are invalid at low vacuum pressures. Therefore, they are not able to predict the accurate convection coefficient for low pressures. In contrast, the numerical model used here does not collapse in a high vacuum. A relationship between pressure and convection behavior was obtained for pressure levels down to 10 Pascals, a pressure at which the thickness of the boundary layer is comparable with the characteristic length of the geometry.

Some practical findings of this work include the degree of instability of the air that can cause non-uniformity of the temperature variation. Enclosing the device in an insulating box helps it be more stable. However, natural convection currents due to heaters cause non-uniformities in the temperature distribution. In fact, convection on the edge of glass generates parabolic distribution isothermal lines, while the convection on the glass front and back faces causes a nonlinear temperature gradient between two heaters.

These and other features of the system are discussed and generalized broadly for application in other mesoscale systems.

2.1 Introduction

Convection is a heat transfer mechanism occurring when a moving fluid experiences temperature variation from an external boundary [15]. Convection is often classified as either forced or natural/free convection. *Forced convection* occurs when the fluid in contact with the boundary (solid wall) is forced externally (e.g. using a fan or pump). *Natural convection* or *free convection* occurs when the fluid moves by itself as it experiences the temperature gradient at the boundary. These gradients produce a change in fluid density that gives rise to buoyancy forces. In many cases, both convection types exist, and the *mixed convection* term is used [1, 14].

Although either forced or free convection can be exploited in heated devices as an efficient cooling mechanism (in a heat sink), there are instances where it is not favorable (e.g. precise thermal conductivity measurement of a sample). For most of the thermal systems in which convection is not favorable, the main goal is to transfer heat through the *conduction*. An example of usefulness of convection in a microfluidic device is a

buoyancy driven thermocycler for PCR developed by Krishnan et al. [16] where natural convection is the driving force replacing an external pump. An example of the adverse effect of convection is the thermal gradient PCR device developed by Crews et al [9]. The objective of this latter work was to create a microflow-based iso-flux condition through conduction; any convection was found to disrupt that iso-flux performance.

The non-dimensional number Biot, $Bi \equiv hL/K$ compares the roles of convection and conduction in affecting the thermal behavior of a device. Convection can be neglected for very small Biot numbers. Since for the most common materials used in the fabrication of microfluidic devices such as glass and polymers, the conduction coefficients are small, even for a typical convection coefficient the Biot number is not small enough to render the convection effect negligible.

In order to investigate how convection affects the performance of a thermal gradient device, IR images of the thermal gradient across the microfluidic chip surface were examined. An example of this non-contact thermal data is shown in **Figure 2-1**. For these experiments, two heaters (one on each long edge of the device) were set at 120 °C and 45 °C. The schematic of the setup is shown in **Figure 2-2**. As can be observed, the temperature distribution along the heaters is parabolic rather than uniform, and the temperature distribution between the top and bottom of the glass is hyperbolic instead of linear.

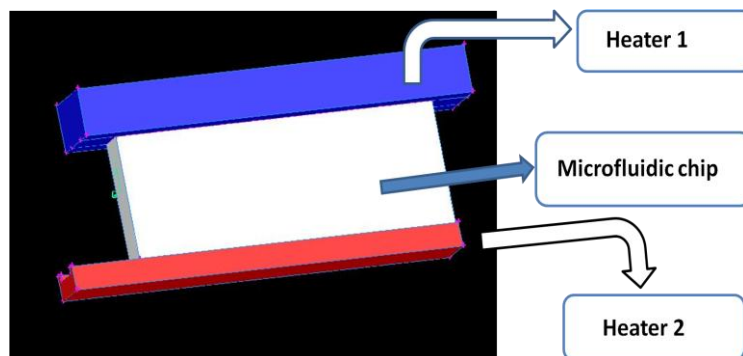


Figure 2-1: Schematic of the thermal gradient set up consisting of heater 1 set at 120 °C, a glass microfluidic chip, and heater 2 set at 45 °C.

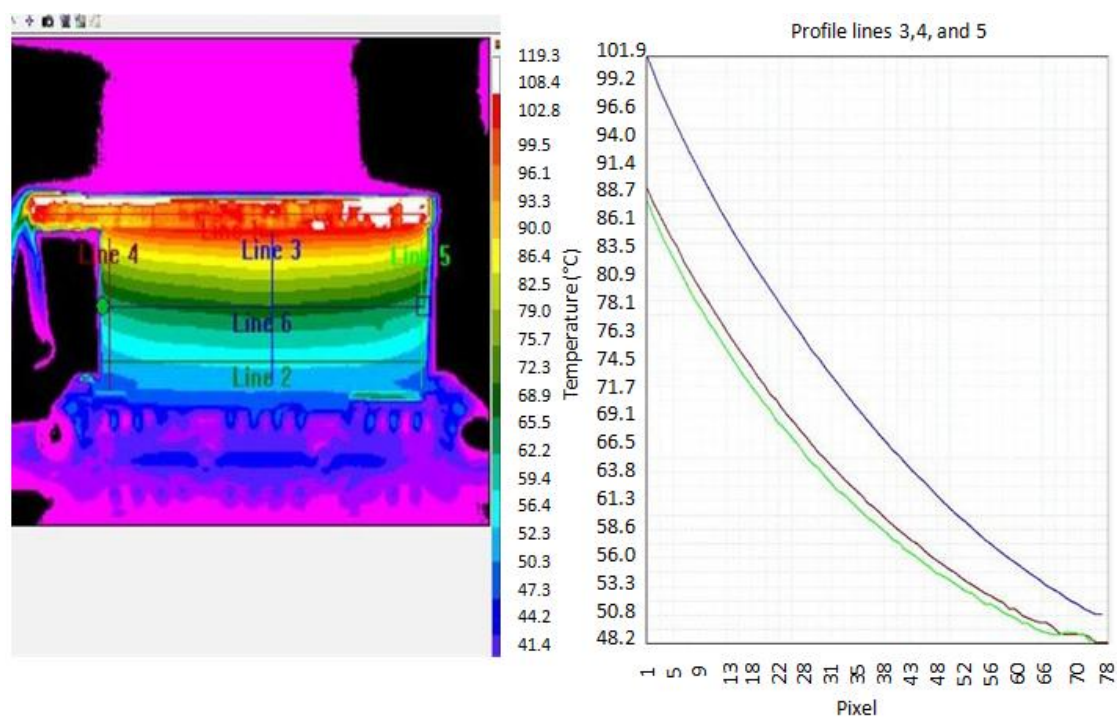


Figure 2-2: IR image of the set up under thermal gradient generated by two heaters set at 120 °C and 45 °C plotted for three ROIs denoted by lines 3,4, and 5.

The ideal temperature distribution compared to a distribution in the presence of convection is demonstrated in **Figure 2-3:**

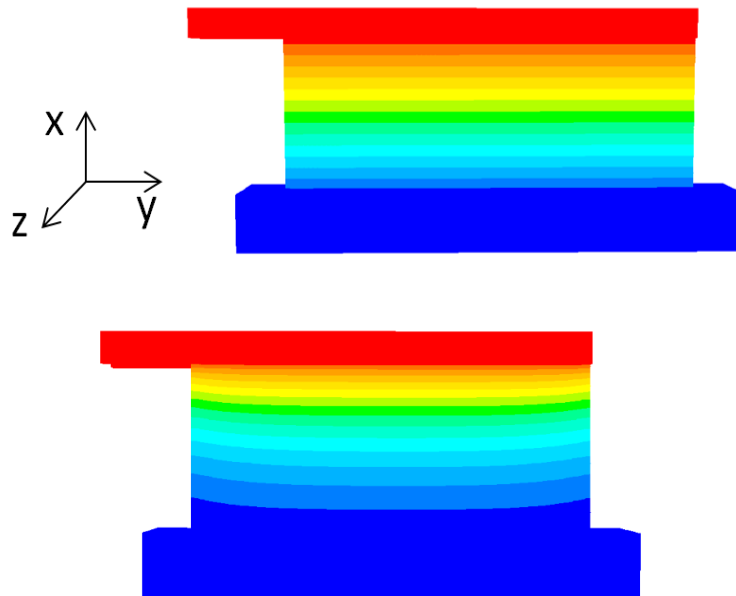


Figure 2-3: Temperature distribution due to pure conduction (top) compared to a distribution due to both conduction and convection (bottom). Simulation result was used.

To quantify the impact of convection, an analytical solution was developed to study these thermal characteristics. This next section provides details on this effort.

2.2 Analytical Solution

Consider a rectangular prism with width, length, and thickness of W , R , and t respectively as shown in **Figure 2-4**:

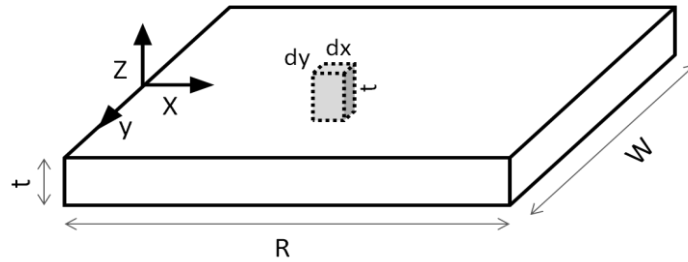


Figure 2-4: Schematic of the geometry and the differential control volume defined for applying the conservation of energy on a rectangular prism

If it is assumed that the thickness t is very small compared to other dimensions and conduction in the Z direction is neglected, this analysis represents the temperature averaged in Z direction. With these assumptions, an element of thickness (t) and cross section dimensions of dx and dy is defined as shown in the **Figure 2-4**. From Taylor expansion of conduction, heat rate in the X and Y directions are:

$$\dot{Q}_{x+dx} = \dot{Q}_x + \frac{\partial \dot{Q}_x}{\partial x} dx \quad \text{Eq. 2-1}$$

$$\dot{Q}_{y+dy} = \dot{Q}_y + \frac{\partial \dot{Q}_y}{\partial y} dy \quad \text{Eq. 2-2}$$

and from Fourier's law:

$$\dot{Q}_x = -kA_x \frac{\partial T}{\partial x} = -ktdy \frac{\partial T}{\partial x} \quad \text{Eq. 2-3}$$

$$\dot{Q}_y = -kA_y \frac{\partial T}{\partial y} = -ktdx \frac{\partial T}{\partial y} \quad \text{Eq. 2-4}$$

where k is the thermal conductivity of the block. Also, for the surface of the element exposed to air, according to Newton's law of cooling:

$$\dot{Q}_{conv} = h_1(T - T_\infty)A_c = 2h_1dxdy(T - T_\infty) \quad \text{Eq. 2-5}$$

where h_1 is the convection coefficient on the XY -plane (wide surface of the block).

Conservation of energy for the defined differential element can be written as:

$$\dot{Q}_x + \dot{Q}_y = \dot{Q}_{x+dx} + \dot{Q}_{y+dy} + \dot{Q}_{conv} \quad \text{Eq. 2-6}$$

After simplifying, **Eq. 2-6** reduces to:

$$\frac{\partial^2 T}{\partial x^2} + \frac{\partial^2 T}{\partial y^2} - \frac{2h_1}{kt}(T - T_\infty) = 0 \quad \text{Eq. 2-7}$$

If the parameters $\theta = T - T_\infty$, and $m^2 = 2h_1/kt$ are defined, then **Eq. 2-7** can be re-written as:

$$\frac{\partial^2 \theta}{\partial x^2} + \frac{\partial^2 \theta}{\partial y^2} - m^2 \theta = 0 \quad \text{Eq. 2-8}$$

boundary conditions for **Eq. 2-8** are :

$$\theta(0, y) = \theta_L \quad \text{and} \quad \theta(R, y) = \theta_H \quad \text{Eq. 2-9}$$

$$\frac{\partial \theta}{\partial y}(x, w/2) = -\frac{h_2}{k} \theta(x, w/2) \quad \text{and} \quad \frac{\partial \theta}{\partial y}(x, 0) = 0 \quad \text{Eq. 2-10}$$

where h_2 is the convection coefficient of the fluid on the YZ-plane (thin edge). **Eq. 2-8** is a Partial Differential Equation (PDE) with non-homogeneous boundary condition due to the convection. To solve this equation, we can assume that

$$\theta(x, y) = \varphi(x) + V(x, y) \quad \text{Eq. 2-11}$$

such that $\varphi(x)$ satisfies the boundary condition in x-direction.

$$\frac{\partial^2 \varphi}{\partial x^2} - m^2 \varphi = 0, \quad \varphi(0) = \theta_L, \quad \text{and} \quad \varphi(R) = \theta_H \quad \text{Eq. 2-12}$$

Eq. 2-12 is the governing equation of a 1-D fin of straight cross section. Solving **Eq. 2-**

12 with regards to its boundary conditions leads to:

$$\varphi(x) = Ae^{mx} + Be^{-mx} \quad \text{Eq. 2-13}$$

where

$$B = \frac{\theta_L e^{mR} - \theta_H}{2 \sinh mR} \quad \text{and} \quad A = \frac{\theta_H - \theta_L e^{mR}}{2 \sinh mR} \quad \text{Eq. 2-14}$$

Inserting $\varphi(x)$ into **Eq. 2-11** simplifies it to:

$$\frac{\partial^2 V}{\partial x^2} + \frac{\partial^2 V}{\partial y^2} - m^2 V = 0 \quad \text{Eq. 2-15}$$

Given $V(x, y) = X(x)Y(y)$, the equation is reduced to:

$$\frac{X''}{X} + \frac{Y''}{Y} - m^2 = 0 \quad \text{Eq. 2-16}$$

So, **Eq. 2-15** can be solved using the method of separation of variables. Separating it by defining the parameters l^2 and λ^2 :

$$\frac{X''}{X} = -\lambda^2 \quad \text{and} \quad \frac{Y''}{Y} = m^2 + \lambda^2 = l^2 \quad \text{Eq. 2-17}$$

and obtaining the boundary conditions by plugging **Eq. 2-11** into **Eq. 2-10**,

$$\frac{\partial V}{\partial y}(x, w/2) = -\frac{h_2}{k} [\varphi(x) + V(x, w/2)] \quad \text{and} \quad \frac{\partial V}{\partial y}(x, 0) = 0 \quad \text{Eq. 2-18}$$

Solution of **Eq. 2-15** is:

$$V(x, y) = \sum_{n=1}^{\infty} 2C_n \cosh ly \sin \frac{n\pi}{R} x \quad \text{Eq. 2-19}$$

$$C_n = \frac{\psi_n}{\left(\frac{-2k}{h_2}\right) \left(l \sinh \frac{lw}{2} + \frac{h_2}{k} \cosh \frac{lw}{2}\right)} = \quad \text{Eq. 2-20}$$

where

$$\psi_n = \frac{2(AH + QR)}{R} \quad \text{Eq. 2-21}$$

and

$$H = \frac{\frac{n\pi}{m^2 R} [e^{mR} (-1)^n - 1]}{\left[1 + \left(\frac{n\pi}{mR}\right)^2\right]} \quad \text{Eq. 2-22}$$

$$Q = \frac{\frac{-n\pi}{m^2 R} [e^{-mR} (-1)^n - 1]}{\left[1 + \left(\frac{n\pi}{mR}\right)^2\right]}$$

so, the temperature distribution is :

$$T(x, y) = T_{\infty} + \varphi(x) + V(x, y) \quad \text{Eq. 2-23}$$

Although an elaborate 3-D solution of the problem provides the temperature distribution in the thickness of the chip additionally, this comparatively simple solution explains the role of key parameters such as convection coefficient, thermal conductivity, and dimensions in the behavior of a thermal gradient chip. The results are in very good agreement with an elaborate 3-D model solved in Fluent for a glass microfluidic chip with dimensions, $W \cdot R \cdot t$ of 45, 22, and 4 mm and a thermal conductivity of 1.38 W/m·K. Figure 2-5 compares the analytical and numerical temperature plotted along the line $x=5\text{mm}$. (directions are shown in **Figure 2-3**)

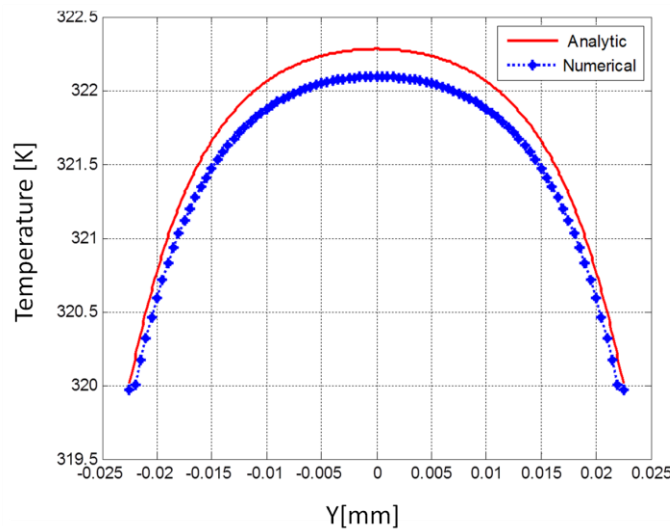


Figure 2-5: Comparison between the results of analytical model and the 3-D model. Temperature was evaluated at $x=5\text{mm}$ in y direction.

One interesting characteristic of this solution is that two different convection coefficients are defined on the XY and XZ plane faces. This is useful in a sense that it differentiates the convection on the edges from the convection on the large front and back

faces of the chip. In fact, the way the convection affects the distribution is different on the edges. This is demonstrated in **Figure 2-6** for four combinations of low and high convection coefficients. Lower values of convection coefficient can be achieved by local insulation on the edges or by putting the enclosure walls in proximity of the edges.

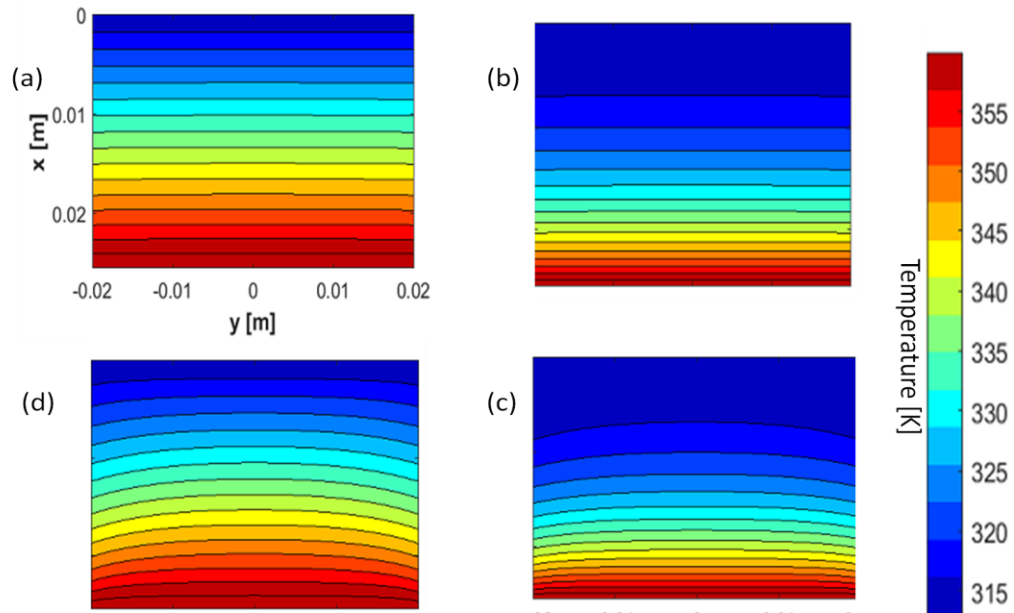


Figure 2-6: Four categories of thermal gradient affected by external convection: a) $h_1=1, h_2=1 \text{ W/m}^2\cdot\text{K}$ b) $h_1=20, h_2=1 \text{ W/m}^2\cdot\text{K}$ c) $h_1=20, h_2=20 \text{ W/m}^2\cdot\text{K}$ d) $h_1=1, h_2=20 \text{ W/m}^2\cdot\text{K}$

In the cases (a) and (c), isothermal lines are equally spaced showing a linear distribution in y direction between the heaters, while the cases (b) and (d) show a parabolic distribution. In the cases (c) and (d), edge effects have made the isothermal lines bent near the edges (parabolic in x direction) while they are almost straight in the cases (a) and (b). Similar outcome was obtained from Fluent simulations which is demonstrated in **Figure 2-7**.

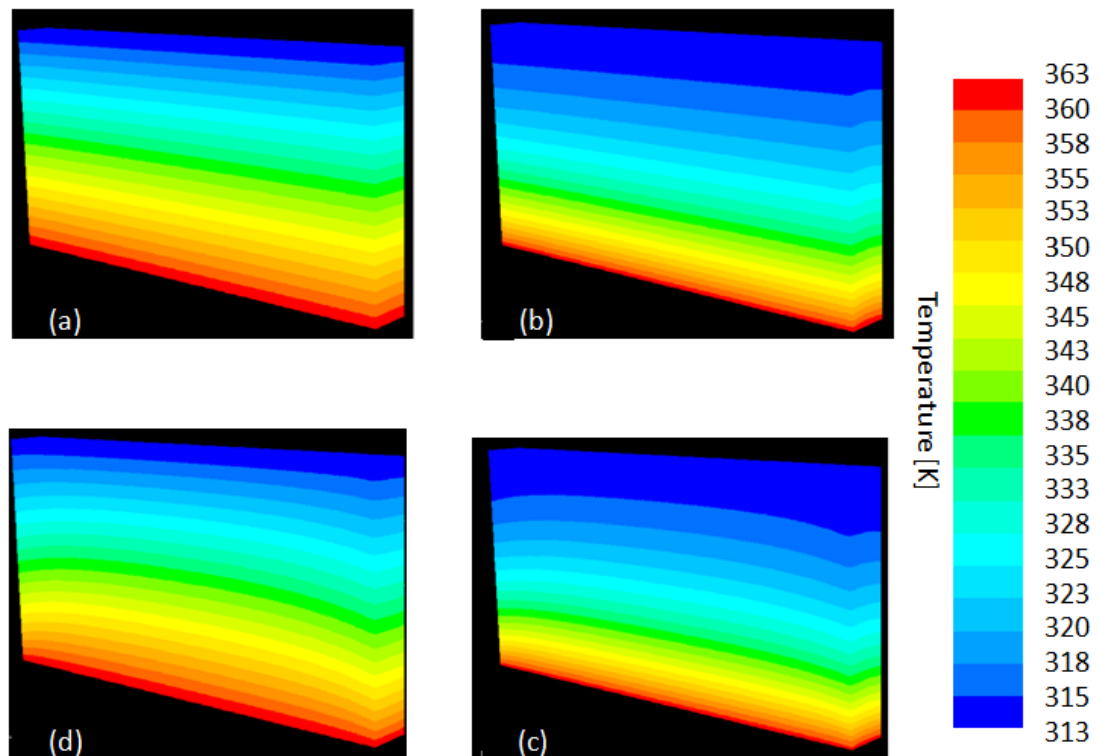


Figure 2-7: Four categories of thermal gradient affected by external convection: a) $h_1=1, h_2=1 \text{ W/m}^2\cdot\text{K}$ b) $h_1=20, h_2=1 \text{ W/m}^2\cdot\text{K}$ c) $h_1=20, h_2=20 \text{ W/m}^2\cdot\text{K}$ d) $h_1=1, h_2=20 \text{ W/m}^2\cdot\text{K}$

If a uniform convection is assumed all around the chip, the impact of convection coefficient on the deviation from the linear temperature distribution along the chip can be evaluated using the analytical solution:

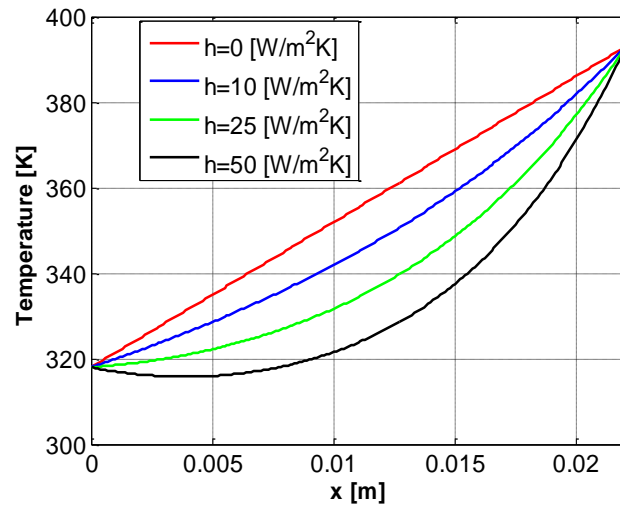


Figure 2-8: Temperature distribution along the centerline of the chip plotted for the convection coefficients of 0, 10, 25, and 50 $\text{W}/\text{m}^2\cdot\text{K}$. The abscissa here refers to the x-direction as indicated in x-axis here refers to Figure 2-3.

The parabolic distribution of the temperature can affect the performance of the device. For example if the thermal gradient chip is set to generate a thermal gradient suitable for PCR, one heater would be set to 50 °C and the other at 120 °C; this generates a zone ideal for PCR (annealing and denaturing reactions occur at temperatures around 60 °C and 95 °C, respectively). If the region of the chip between these two temperatures is considered as "PCR window," the variation of convection coefficient not only shifts this window, but also affects the width of it. To demonstrate it, from the analytical solution the location of average $T=60\text{ °C}$ and $T=95\text{ °C}$ was shown in **Figure 2-9**, and the distance between these two regions was demonstrated by parameter L under no convection and parameter L' under the convection. The ratio L'/L demonstrates the impact of convection coefficient on the "PCR window."

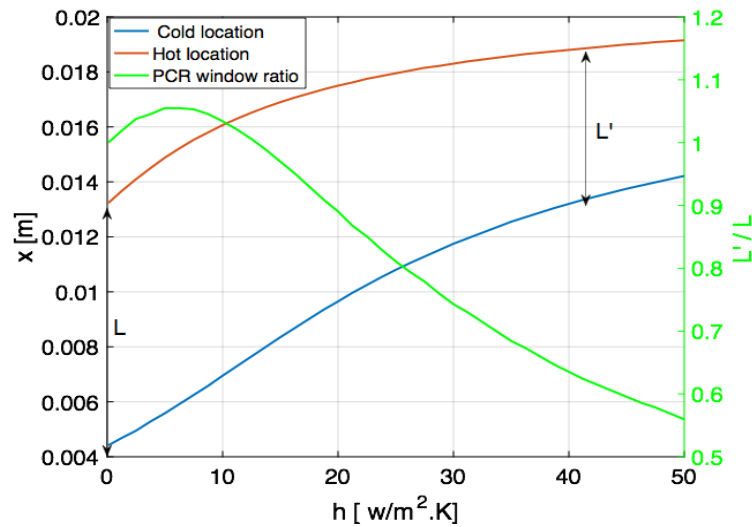


Figure 2-9: Impact of convection coefficient on the size of PCR window and its location. The red and blue color corresponds to the location of average $T=95^{\circ}\text{C}$ and $T=60^{\circ}\text{C}$ respectively. Distance between the location of these temperatures is defined by parameter L at no convection and parameter L' , under the convection. Right axis denotes the ratio L'/L demonstrating the impact of h on PCR window.

The size and location of the PCR window are of great importance when an optical system is integrated for capturing the fluorescence signal. Since ideally any variation should be avoided, we have focused on minimizing and stabilizing the convection coefficient. By encompassing the chip in an air tight enclosure, the disturbance due to the variation of convection coefficient can be minimized along with the reduction of convection coefficient. IR images of the chip inside and outside the box show a significant difference between the two cases.

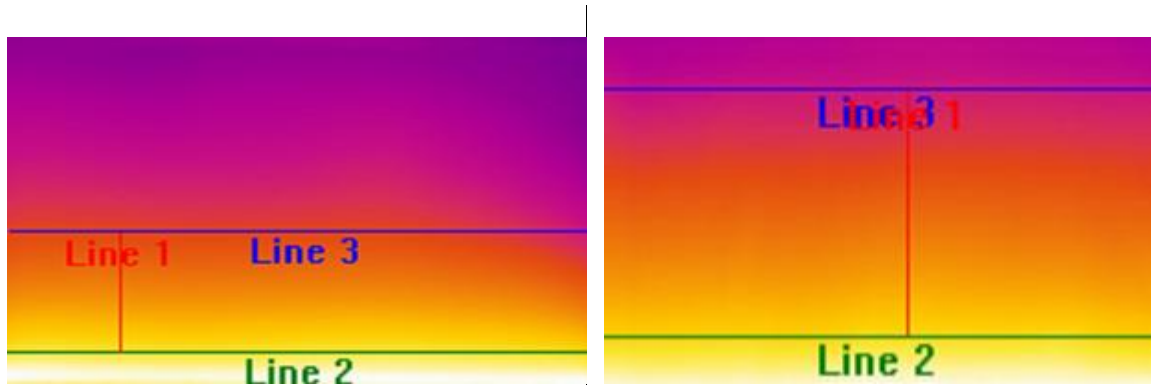


Figure 2-10: Actual IR images showing the PCR window for a chip inside and outside an enclosure

Although the share of forced convection will be minimized in this way, due to high temperature difference between the heaters and the ambient air, natural convection currents will be generated inside the box. In the next section, this phenomena and ways to minimize it will be discussed.

2.3 Natural convection

To characterize the natural convection and to explore the ways to control it, theoretical, experimental, and numerical methods were applied to analyze it and to investigate the efficient and practical parameters for minimizing it.

2.3.1 Theory

As discussed in the introduction, unlike the forced convection where an external source is the reason for fluid movement, in the natural convection, fluid moves due to change in its density in the presence of a body force. In general, density change can be due to variation of temperature, pressure, or concentration depending on the equation of state of the fluid, leading to a complicated problem. However, based on the assumption that $\Delta\rho/\rho \ll 1$, the change in the density can be expanded in terms of change in its properties:

$$\Delta\rho = \left(\frac{\partial\rho}{\partial T}\right)_{p,C} (T - T_0) + \left(\frac{\partial\rho}{\partial p}\right)_{T,C} (p - p_0) + \left(\frac{\partial\rho}{\partial C}\right)_{p,T} (C - C_0) \quad \text{Eq. 2-24}$$

Boussinesq approximation neglects the pressure term and assumes a linear relationship between the density change and variation in the temperature and concentration [17]. For a single fluid, the last term is zero, and **Eq. 2-24** simplifies to:

$$\rho \cong \rho_0 - \rho_0\beta(T - T_0) \quad \text{Eq. 2-25}$$

where β is the volumetric coefficient of thermal expansion which is $1/T$ (T is the absolute temperature) in the case of ideal gasses.

Here, only the gravity is acting as the body force giving rise to the buoyancy forces. Consequently, the momentum equation can be written as:

$$\frac{D\mathbf{u}}{Dt} = -\frac{1}{\rho}\nabla p + \nu\nabla^2\mathbf{u} - \beta\mathbf{g}\Delta T \quad \text{Eq. 2-26}$$

Performing a scale analysis introduces two important non-dimensional numbers playing a very important role for characterizing the natural convection flow [1, 14]:

$$Gr_y = \frac{g\beta(T_w - T_\infty)y^3}{\nu^2} \quad \text{and} \quad Ra_y = Gr_y Pr \quad \text{Eq. 2-27}$$

where Grashof number, Gr_y is the ratio of buoyancy force to friction force and Rayleigh number, Ra_y plays the role of Reynolds number in determining the transition from laminar to turbulent flow.

Also, further interesting conclusions can be deduced from scale analysis. Based on the condition that the buoyancy is balanced by inertia term or by friction term, Nusselt number, Nu_y can be proportional with $(Ra_y Pr)^{1/4}$ or $(Ra_y)^{1/4}$ respectively [14]. At any rate, it can be simply concluded that the lower the Ra_y is, the lower the Nu_y and the lower the convection coefficient are.

For the thermal gradient problem, the dimension of the chip is restricted by the optical system, and therefore, reducing the characteristic length is not a practical way for reducing the $(Ra_y)^{1/4}$. Temperature difference cannot be smaller than certain value as the thermal gradient should be fixed between two set temperatures (around 30 K for PCR). On the other hand, it can be concluded that $Ra_y \propto \rho^2$ or $Ra_y \propto p^2$ for the ideal gas. Therefore, reducing the pressure is the best option for decreasing the convection coefficient associated with natural convection.

2.3.2 Experiment

A simple experiment was conducted to observe and quantify the pressure effect on convection coefficient. The vertical cylinder geometry is a very appropriate choice as it is a common geometry in the natural convection studies and a semi-analytical solution based on Bussinesq approximation exists for it [14].

A cylindrical aluminum block (D=19 mm, H=22.5 mm) was heated to 100 °C on a hot plate. One thermocouple was attached to a hole inside the block, and another one was exposed to air to measure the ambient temperature. Both thermocouples were connected to a data logger (Omega HH147U, CT, US). The hot block was mounted on a plastic rod inside the cylindrical vacuum chamber. The vacuum chamber pumps the pressure down to a high vacuum level (lowest in this experiment was around 300 milliTorr). When the block was heated to few degrees over 80 °C, it was transferred to the vacuum chamber. Once the temperature would reach the 80 °C, the vacuum would be pulled and the data would be recorded. The experiment was done for vacuum pressures of 1000, 300 milliTorr, and the atmospheric pressure. **Figure 2-11** is the image of the set up.

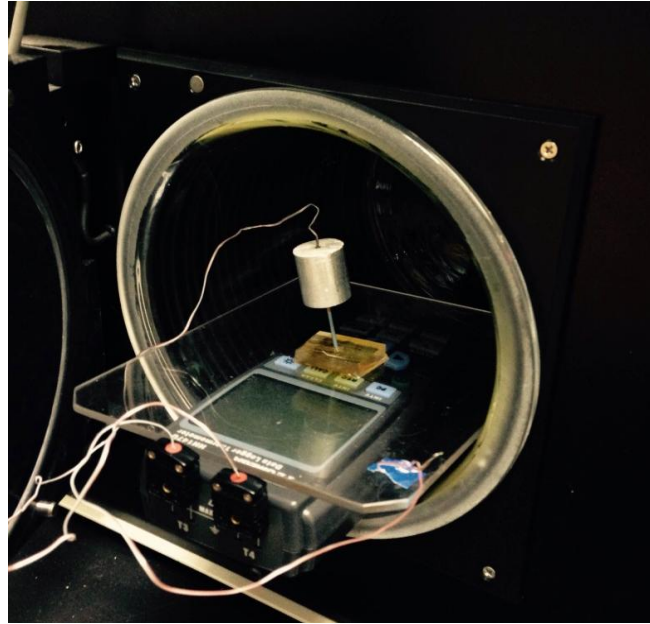


Figure 2-11: Picture of set up used for measuring the natural convection coefficient under vacuum. The cylindrical aluminum block is mounted on a solid PDMS pad by a thin plastic rod (in order to reduce conduction). Two thermocouples are attached to the data logger: one measures the ambient temperature, and the other one measures the temperature of the block.

As the $Bi \ll 1$, the lumped heat transfer assumption is valid, and the surface and inside temperatures of the block are almost the same. Recorded temperature can be used to estimate the convection coefficient using lumped capacity method [1]:

$$\theta = \frac{T - T_{\infty}}{T_0 - T_{\infty}} = \exp\left(-\frac{hA_s}{mCp} t\right) \quad \text{Eq. 2-28}$$

where T_0 is the initial temperature of the block, T_{∞} is the ambient temperature, A_s is the area of the device exposed to convection, and mCp is the heat capacity of the block.

Therefore, the convection coefficient can be simply calculated from this equation:

$$\log\theta = -\frac{hA_s}{mCp} t \quad \text{Eq. 2-29}$$

This experiment is very sensitive to the insulation of the sample. The best insulated sample showed about 25% reduction in the measured convection coefficient compared to

the primary experiments. An example of the non-dimensional temperature θ over time is shown in **Figure 2-12**:

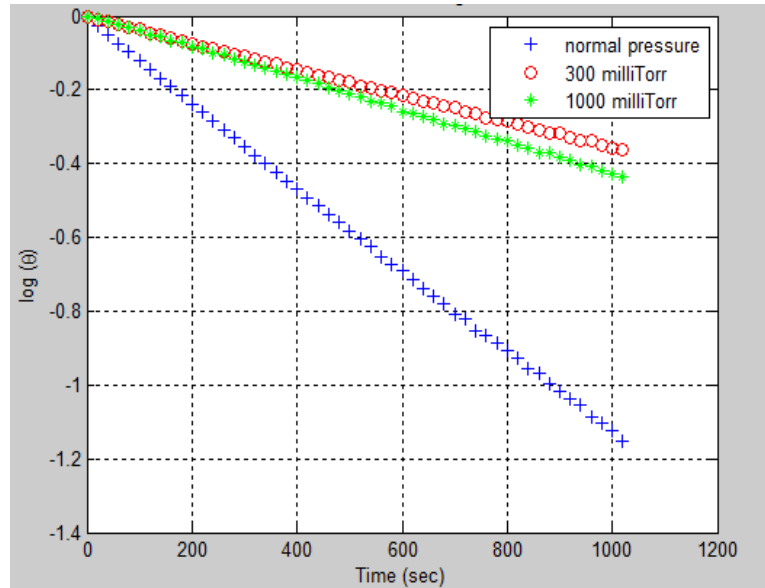


Figure 2-12: dimensionless temperature of the block over time for normal pressure, a moderate vacuum (1000 milliTorr) and a higher vacuum level (300 milliTorr)

Using equation **Eq. 2-24**, these values are calculated for the convection coefficients if the starting point of the temperature is 70 °C for about 1000 seconds.

$$h (300 \text{ milliTorr}) = 2.775 \left[\frac{\text{W}}{\text{m}^2 \cdot \text{K}} \right]$$

$$h (1000 \text{ milliTorr}) = 3.375 \left[\frac{\text{W}}{\text{m}^2 \cdot \text{K}} \right]$$

$$h (\text{normal pressure}) = 8.782 \left[\frac{\text{W}}{\text{m}^2 \cdot \text{K}} \right]$$

However, for the data recorded in the same experiment and for same duration, if the starting point is considered to be at 50 °C, it leads to smaller values:

$$h (300 \text{ milliTorr}) = 2.625 \left[\frac{\text{W}}{\text{m}^2 \cdot \text{K}} \right]$$

$$h (1000 \text{ milliTorr}) = 3.356 \left[\frac{\text{W}}{\text{m}^2 \cdot \text{K}} \right]$$

$$h \text{ (normal pressure)} = 7.491 \left[\frac{\text{W}}{\text{m}^2 \cdot \text{K}} \right]$$

The reason is that **Eq. 2-28** calculates the mean convection coefficient. However, convection coefficient is depending on the temperature difference in the case of natural convection. So, when the starting point is a lower temperature, it takes longer time to be cooled due to less temperature difference between the block and air. This will be elaborately studied in the next section.

2.3.3 Temperature dependency of natural convection coefficient

As observed in the previous section, the convection coefficient is a function of temperature. This is verifying an important aspect of natural convection: for natural convection, there is no fundamental convection coefficient defined according to Newton's law of cooling to correlate the heat transfer with temperature. As discussed in section 3.3.1, Nusselt number and consequently convection coefficient depend on $(Ra_y)^{1/4}$ which depends on temperature difference by itself unlike the forced convection case. As it is discussed by Tritton, [15] this is due to the "dual role of temperature difference"; Tritton argues "The larger it is, the greater the rate of heat transfer by a particular flow rate; but also the larger it is, the greater is the flow rate."

Thus, instead of a mean convection coefficient, instantaneous convection coefficient was evaluated:

$$mC_p \frac{dT}{dt} = -h(t)A_s(T - T_\infty) \quad \text{Eq. 2-30}$$

The data was noisy, so a Savitzky-Golay filter was used to smoothen it.

Along with the experimental data, the transient cooling of the cylinder at normal pressure was simulated in Fluent using the ideal gas model. The result shows a very good accordance as plotted in **Figure 2-13**.

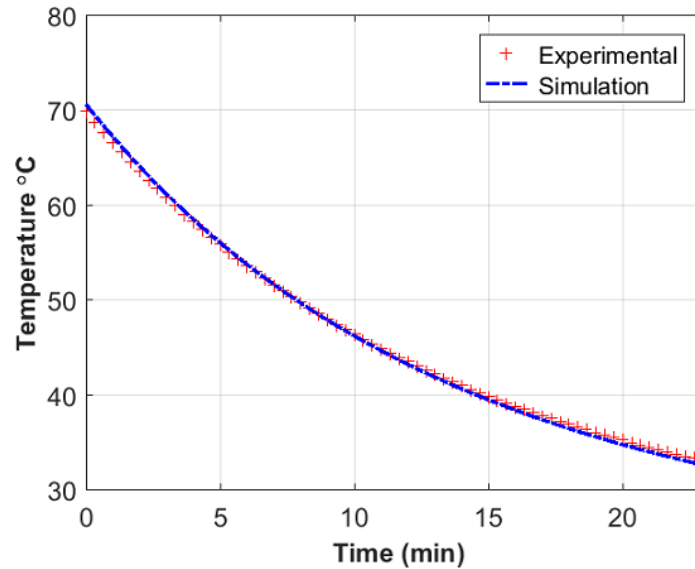


Figure 2-13: Experimental and numerical results for the gradual cooling of a cylindrical block oriented vertically due to natural convection.

There are two analytical solutions for a vertical cylinder, depending on how thermal boundary layer thickness, δ_T , is compared with the diameter of the cylinder, D . If $\delta_T < D$, then thick cylinder solution, which is the equivalent of external flow on a vertical wall solution, is valid, otherwise the curvature of the cylinder affects the boundary layer, and *thin cylinder* solution is valid. From scale analysis, thickness of thermal boundary layer is $\delta_T \sim L Ra_L^{-1/4}$, so the criterion for the validity of thick cylinder solution is [14]:

$$\frac{D}{L} > Ra_L^{-1/4} \quad \text{Eq. 2-31}$$

This inequality is valid for the geometry used in this experiment.

The results from both of the thin and thick cylinder analytical solutions, the experimental, and the simulation are plotted in **Figure 2-14**. The thin cylinder correlation (black color) is plotted here only for the comparison.

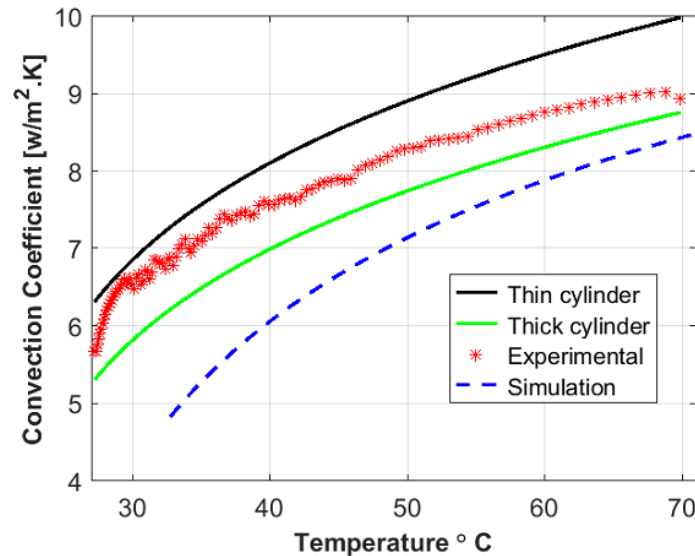


Figure 2-14: Analytical, experimental, and simulation results for temperature dependency of convection coefficient around a heated vertical cylindrical block.

As can be seen in **Figure 2-14**, the result of the thick cylinder solution is in a better agreement with both the experimental and numerical results. The higher convection coefficient calculated from the experiment is reasonable and is due to the heat loss through the conduction. Also, simulation predicts a smaller convection coefficient compared to the thick cylinder solution as the analytical thick cylinder solution calculates the convection coefficient indirectly based on the temperatures measured in the experiment.

2.3.4 Pressure dependency of natural convection coefficient

In the previous section, Fluent simulation using the ideal gas model was validated against experimental and analytical data for the gradual cooling of a cylindrical block at

normal pressure. Here, pressure dependency of natural convection around a vertical wall in an external flow was considered. The results from Fluent were compared with the vertical plate correlation [1]:

$$\bar{h} = \frac{k_{air}}{L} \left\{ 0.68 + \frac{0.67 Ra_L(P)^{1/4}}{[1 + (0.492/Pr)^{9/16}]^{4/9}} \right\} \quad Ra_L \leq 10^9 \quad \text{Eq. 2-32}$$

showing a very good agreement for most of the pressure ranges with only deviation at very low pressures:

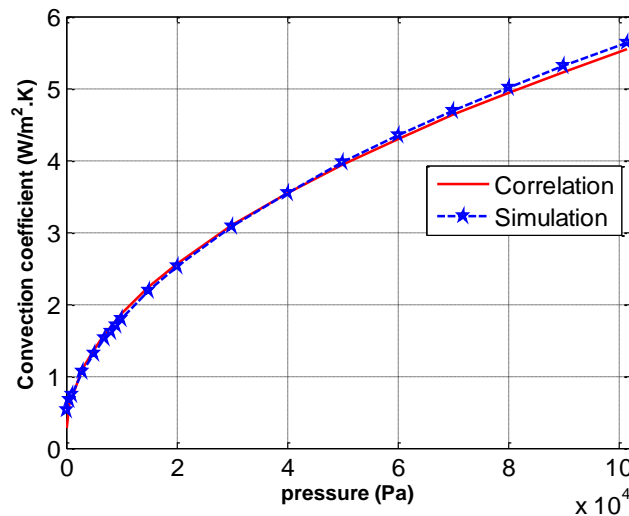


Figure 2-15: Convection coefficient on a vertical wall as a function of pressure evaluated by simulation and **Equation 2-32**

This solution is valid when there is no limit for the growth of boundary layer. As mentioned in previous sections, $\delta_T \sim L Ra_L^{-1/4}$ predicts a rapid growth of boundary layer with pressure decrease. This can be visually seen in the thermal contours around the vertical cylinder performed in Fluent at normal pressure and 300 milliTorr:

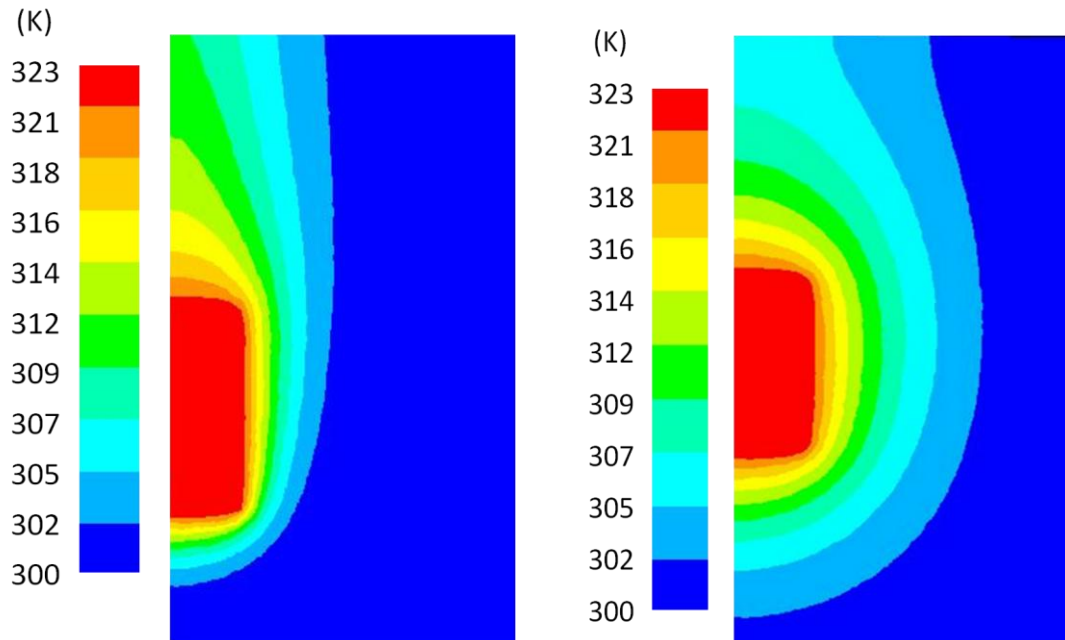


Figure 2-16: Thermal contours around the heated cylinder at normal pressure and 300 milliTorr

This requires an enormous vacuum chamber. In an enclosure where the heated wall has a distance of H from the cool wall, when the thermal boundary layer reaches the cool wall, Nusselt number converges to L/H [14]. This means that the heat transfer is governed by the conduction of the air rather than convection.

$$\text{Nu}_L = \frac{hL}{k_{\text{air}}} = \frac{L}{H} \Rightarrow h = \frac{k_{\text{air}}}{H} \quad \text{Eq. 2-33}$$

This suggests that the reduction of convection coefficient will reach a limit. The wider the vacuum chamber is, the smaller the convection coefficient will be. For a fixed distance H , further reduction of the convection coefficient is only possible by reducing the thermal conductivity of the air. Thermal conductivity of ideal gases is pressure invariant when the continuum condition is valid. So, there is no way to reduce the convection coefficient when it reaches to the conduction limit unless the continuum

collapses. This happens when mean free path of the gas is in the order of characteristic length H or smaller, or in other words, when the Knudsen number, Kn , is larger than 1.

So, the corresponding pressure can be estimated

$$P = \frac{k_b T}{\sqrt{2} \pi d^2 H} \quad \text{Eq. 2-34}$$

where k_b is the Boltzmann constant, T is the absolute temperature, and d is the kinetic diameter of the gas molecules. From **Eq. 2-34**, it can be concluded that the smaller the vacuum chamber is, the higher vacuum level is required for reducing the thermal conductivity of the air. However, reaching to this level requires a very powerful vacuum pump as well as very special vacuum chamber equipment.

2.4 Conclusion

The role of convection in a glass meso-scale chip involving conduction cannot be neglected. Enclosing the system protects it from the disturbance due to the ambient air convection and improves the performance of the thermal gradient. However, it gives rise to the natural convection currents in the enclosure which cannot be overlooked. The most efficient way to minimize the natural convection is to operate the conduction under the vacuum. A numerical study and corresponding experiments were performed to study the pressure dependency of the convection coefficient. The results show that the vacuum is efficient until a certain level. As soon as the boundary layer reaches the physical walls enclosing the heating device, the heat transfer is governed by the conduction in the air rather than the convection. Therefore, further improvement is not achievable until the thermal conductivity of the air decreases with pressure. This requires a vacuum level in which the mean free path of air molecules is equal or more than the distance between the

device and the enclosure wall. Reaching to such a level requires a special vacuum sealed design and a very powerful vacuum, which is out of the focus of this research.

CHAPTER 3

DETECTING THERMAL ASYMMETRY IN MICROFLUIDICS FOR SENSOR APPLICATIONS: CRITICAL DESIGN CONSIDERATIONS AND OPTIMIZATION

This article discusses the design and performance of continuous-flow microfluidic thermal sensors that operate on the principle of heat generation through lateral mixing. The platform under study is a Y-channel microfluidic device in which two laminar streams are brought into side-by-side contact under precise flow control. For this work, the two merging microchannels carry water and ethanol respectively; heat is generated as the liquids diffuse together. While much exists in the literature regarding the magnitude of this heat of mixing, this article examines the spatial distribution of this heat – in particular, the extent of lateral asymmetry in the resultant temperature map. This asymmetry is detected with milli-Kelvin sensitivity using a thin-film thermopile integrated on the exterior surface of the microdevice. Since this experimental configuration is implemented by numerous research groups in the design of biosensors and microfluidic calorimeters, a particular emphasis of this present study is on maximizing the detection sensitivity. The impact of the experimental parameters of volumetric flow rate and flow ratio on detection sensitivity was examined, and the optimum axial location for the thermopile sensor under a range of conditions was determined. Experimental and numerical methods were used in this study.

3.1 Introduction

Calorimetric biosensors have been used for detecting various bioprocesses such as enzyme-substrate activity [18, 19], protein binding activity [20, 21], DNA reactions [22, 23] and cell metabolism [24, 25]. Microfluidic calorimeters have been developed in recent years for their advantages in sample handling, speed of detection and sensitivity. Several types of temperature sensors have been incorporated in these systems, including thermistors [26, 27], thermopiles [28-30] and RTD's [31, 32]. In each instance, the sensor transduces the heat produced from a biochemical reaction into a measurable electrical output. Of these, thermopiles have the distinct feature of common-mode background rejection, which enables the measurement of subtle thermal events – even when they are orders of magnitude smaller than the ubiquitous variations in ambient temperature [13]. Owing to this feature, thermopiles are superior sensors for the detection of asymmetry within two-dimensional temperature distributions. Thermopiles have been used for biological reagent detection as well as chemical analysis. For example, Baier et al. demonstrated the development of a microcalorimeter with bismuth (Bi)-antimony (Sb) thin film thermopiles to detect the exothermic reaction of oxidation of ascorbic acid by ascorbate oxidase [33]. Lerchner and colleagues were able to apply the same method for the measurement of oxidation of glucose by glucose oxidase/catalase [34], metabolic dynamics of biofilms in real-time [35] and hybridization of single stranded DNA strands [36]. More recently, Guilbeau et al developed thermopile-based sensors for the detection of glucose [37], L-glutamate [38], and for DNA sequencing [39].

Two “species” of device designs have developed: one involves separate reaction chambers [40] or flow channels [29], with one serving as the “measuring” location, and

the other as the “reference”; the other design style relies on a non-homogeneity within a single flow channel [41, 42] or sample chamber [19]. This non-homogeneity is evaluated by comparing the temperature difference between a measuring *region* and a reference *region* within the same physical space. The designs having distinct and separate channels (sensing under flow) or chambers (sensing under a no-flow condition) for the reference and measuring zones are superior than single-channel/chamber devices at thermally isolating the two regimes from each other. However, such embodiments also sacrifice some of the common-mode rejection potential that is the marked advantage of thermopile sensors. Ambient temperature gradients will distort measuring and reference temperatures to the degree that they are spaced apart from each other. In addition, other unavoidable experimental inconsistencies - such as variations in pressure drop or flow control within the two regions - can create further artifacts in measured signals. These effects are minimized when the measuring and reference regions are within the same flow channel or sample chamber. In such systems there are two approaches that can be used to direct heat signal to the measuring junctions and isolate it from the reference junctions:

1. Controlled symmetry or asymmetry of heat generation by using localized surface preparation. For example, Nestorova and colleagues have used such a method for microfluidic ELISA [18].
2. Heat generation occurs at the interface of two fluid streams, in a way similar to that used by Conway [43], Sen [44] and colleagues with their powerful nanohole sensing technique. In such a configuration, the location of the fluidic interface is used to direct the heat flow.

In both instances, the asymmetry of the heat and the resultant sensitivity of the

thermopile measurements are heavily determined by such factors as flow rate and the geometric positioning of the heat generation regions within the microchannel. This article examines these critical performance characteristics. Specifically, this article treats this latter single-channel device design; however, the findings from this study are applicable to many different styles and categories of microfluidic thermal sensing devices.

In this article, the effect of design and operational parameters will be examined on a representative Y-junction microfluidic device. For both the experimental and numerical analysis, the interfacial mixing of water and ethanol streams will be used as the heat source. Water/alcohol mixing is often used as a standard for calibrating the calorimeters and other thermal measurement systems [45-48]. Fundamentally, the mixing of water and ethanol involves the breaking of hydrogen bonds between identical molecules and the formation of new hydrogen bond network between dissimilar molecules [49, 50] through the intermolecular interaction between water and ethanol as well as hydrophobic hydration interactions.

3.2 Experimental Methods

The experimental setup used for this study contains a microfluidic device with an embedded channel where two liquids streams join at a Y-junction. A thermopile is affixed to the exterior of the microdevice, one centimeter downstream from the Y-junction, and oriented symmetrically along the centerline of the microchannel. Precision syringe pumps and valves control the water and ethanol flows into the device; a nanovoltmeter records any electrical potential transduced in the thermopile caused by asymmetry in the temperature distribution caused by the water/ethanol mixing. The

microdevice itself is located within a thermally-insulated Faraday cage to reduce system noise.

3.2.1 Microfluidic Device Fabrication

The microfluidic device was fabricated using a rapid-prototyping method previously detailed [51]. The embedded microchannel has a rectangular cross-section (100 μm x 3.5 mm). As shown in **Figure 3-1a**, these devices are formed by sandwiching a patterned adhesive tape between a blank glass coverslip (75 mm x 25 mm x 0.13 mm) and a microscope slide (75 mm x 25 mm x 1.0 mm) pre-drilled with inlet and outlet holes. The channel pattern is cut from the double-sided polyimide tape (PPTDE-1, KaptonTape.com) using a cutting plotter (CE 5000-40-CRP, Graphtec America Inc., USA). Ports for the fluidic tubing interfaces are manually cut from a 6mm-thick sheet of PDMS and then cored with a 1.1mm diameter punch (33-31A, Miltex, PA, USA). These ports are permanently bonded over the drilled holes in the microscope slide by activating the mating surfaces with an air plasma (Harrick Plasma, NY, USA) and then gently pressing them together for 30 seconds.

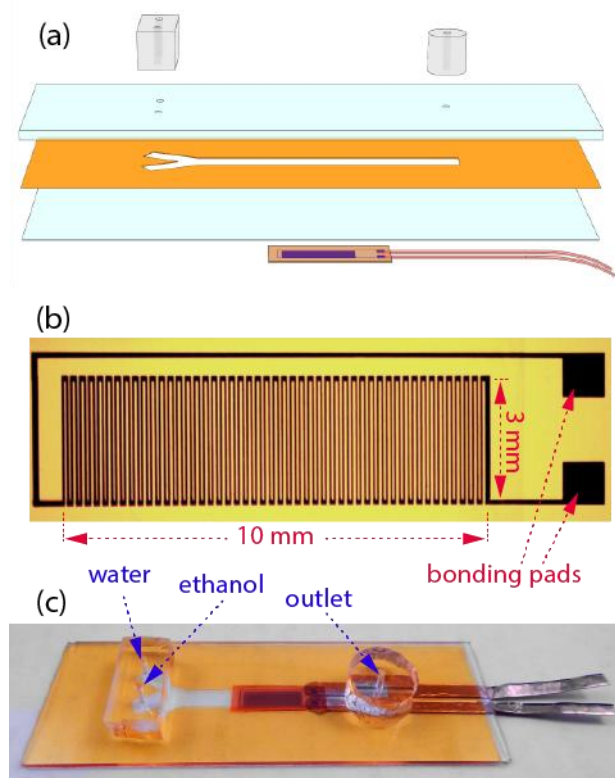


Figure 3-1: (a) Diagram of the microfluidic device fabrication. The microchannel is formed by sandwiching a patterned polymer tape between two glass blanks. PDMS ports are added where tubing will connect to the inlets/outlet of the microchannel. The thermopile is placed on the exterior of the device, opposite the flow channel (b) Photo of a Sb/Bi thermopile used for these experiments. (c) Photo of an assembled device.

3.2.2 Thermopile Sensor Fabrication

To detect any thermal asymmetry within the microchannel, a bismuth (Bi)/antimony (Sb) thin film thermopile is attached to the outer surface of the glass coverslip, directly opposite the microchannel, with the junctions symmetric about channel centerline. Although the thermopile design is unique to this present work, the fabrication process itself is elaborated in detail by Guilbeau et al [7]. Briefly, the thin film thermopile is fabricated on a 50 μm -thick polyimide film. Deposition of first the bismuth (0.8 μm thick) and then the antimony (1.2 μm thick) is performed by thermal evaporation through

two complementary shadow masks. **Figure 3-1b** shows a photograph of a fabricated thermopile having 50 junction pairs. The alternating vertical traces (“vertical” in reference to the orientation shown in the figure) of Bi and Sb occupy a 3 mm x 10 mm surface area. This configuration has a theoretical Seebeck coefficient of $5.95 \mu\text{V}(\text{mK})^{-1}$. The thin film thermopile fabricated onto the polyimide support was attached to the underside of the glass coverslip that forms the base of the microfluidic device using a low-viscosity cyanoacrylate adhesive (Super Glue, Ontario, CA). Thin copper sheet (VHB Tape, 3M, USA) and conductive paint (Silver Print, GC Electronics, USA) was used to make electrical contact with the thermopile bond pads. The completed device is shown in **Figure 3-1c**.

3.2.3 Experimental Setup

The 50 Bi/Sb junctions along the bottom of **Figure 3-1b** are denoted as the reference junctions and the 50 near the top of **Figure 3-1b** as the measuring junctions. Care was taken to mount the junction pairs symmetrically about the centerline of microchannel. In this way, a temperature distribution symmetric about that centerline would transduce no voltage in the sensor, regardless of its magnitude [13]. Asymmetry with higher temperatures toward the water inlet side of the device (labeled in Figure 1c, is the same as “up” in **Figure 3-1b**) would result in a positive voltage being transduced. For the experiments performed, this voltage was collected with a nanovoltmeter (34420A, Agilent, USA) and recorded onto a computer using LabView SignalExpress (National Instruments, USA). The microdevice and nanovoltmeter were placed in a thermally-insulated Faraday cage to reduce the thermal perturbations caused by the irregular air currents in the room and to reduce the electrical noise within the recording system. Two

syringe pumps (Pump11 Elite, Harvard Apparatus, USA) were used to flow deionized water and ethanol (Ethyl Alcohol Pure 200 Proof, EMD Chemicals Inc., USA) through the microfluidic device. For experiments where bolus volumes of ethanol were used, a precision injection valve (Rheodyne® 9725 Injector, Chrom Tech, Inc., USA) was placed inline with the syringe connected to the ethanol inlet of the microdevice.

3.2.4 Experimental Procedure

Two categories of experiments were performed: bolus mixing and continuous mixing of water and ethanol. Bolus mixing is particularly relevant to the many applications in which low volumes of individual samples are to be analyzed. For the bolus experiments, DI water was continuously pumped through both inlets of the microchannel, and a 5 μl volume of ethanol was injected into the ethanol line at a specific timepoint. The relative volumetric flow rates of the two streams were adjusted so that the lateral interface of the ethanol and the water stream would occur at different lateral locations within the microchannel. In this way, the mixing interface where heat is generated was shifted to one side or the other of the channel centerline. Several volumetric flow rates and ratios were used to study the response of the thermopile.

While the bolus tests were conducted to demonstrate the sensitivity of the experimental system, the continuous mixing of ethanol and water streams was tested to evaluate the parametric-dependent performance of the system, and to validate the numerical model. For these steady-state experiments, syringes were filled with water and ethanol, respectively, and the syringe pumps were programmed to periodically change the ratio of flow rates in the two Y-channel inlets. In this way, the location of the mixing interface would shift in relation to the microchannel centerline such that a detectable and

quantifiable thermal asymmetry would occur under a range of conditions. Volumetric flow rates up to 400 $\mu\text{l}/\text{min}$ were examined.

3.3 Numerical Simulation

A 3-D numerical model corresponding to the steady-state response of the sensor was created using the commercial CFD software Fluent (ANSYS, Canonsburg, PA). In this model, conservation equations of mass, momentum, species and energy are solved for the exothermic mixing of two incompressible laminar fluid streams brought together in a side-by-side configuration (see **Figure 3-2**). To minimize the false diffusion error, a power-law discretization scheme was applied for the convection-diffusion equation in the pressure-based solver [52]. The SIMPLEC algorithm defined in the software was used for the coupling of pressure and velocity. For the rest of the parameters, second-order upwind discretization schemes were used.

3.3.1 Model Geometry

A Y-shaped channel microfluidic chip similar to the experimental device was simulated in Fluent. The height of the channel is 100 μm and the width is 3.5 mm. In the computational domain, only the length of the chip containing the channel is modeled. The top surface of the channel is in contact with a glass coverslip of 130 μm thickness and the bottom surface is in contact with glass of 1 mm thickness. The sides of the channel are in contact with the polyimide.

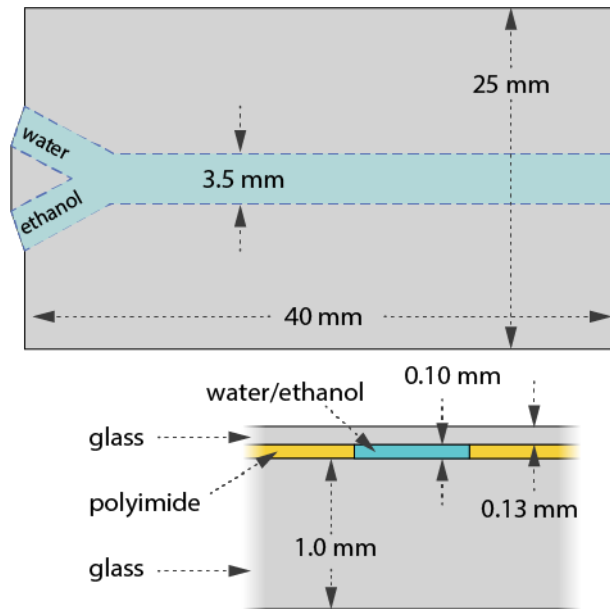


Figure 3-2: The dimensions and materials of the conjugate heat transfer model developed in Fluent. This orientation is inverted from the orientation shown in **Fig 3-1a** and **3-1c**.

3.3.2 Governing Equations

The species model is used for modeling the mixing of water and ethanol. The multi-component (or Fickian) diffusion model is used for incorporating the mass diffusion coefficients. A User-Defined-Function (UDF) is written for applying the energy released when water and ethanol are mixed. A separate UDF was also used to model the concentration-dependent density and viscosity of the mixture. This is important because the viscosity of water and ethanol as they mix is highly non-linear with respect to concentration. In fact, the viscosity of the mixture can be almost three-fold (2.9 Pa·s, at an ethanol mass fraction of 0.4) than that of the unmixed water (1 Pa·s) and ethanol (1.2 Pa·s) at room temperature [53]. In addition, the viscosities are also dependent on temperature. However, the temperature changes produced by this exothermic reaction are on the order of only a few degrees. Since the resulting viscosity change would be less

than 2%, this numerical model does not include this effect – as suggested by Orsi et al.[53]. Since the viscosity defines the local fluid velocities at the mixing interface, which in turn affects the heat generation rate, this unique behavior is significant.

Therefore, the Fluent UDFs proposed by Mauri were included here.

The maximum Knudsen number is 2.5×10^{-6} , which support the continuum model assumption. The maximum Reynolds number of 320 supports the laminar model for the flow rates used in the simulation.

$$\text{Continuity equation} \quad \nabla \cdot \vec{V} = 0 \quad \text{Eq. 3-1}$$

$$\text{Momentum equation} \quad \vec{V} \cdot \nabla \vec{V} = -\frac{1}{\rho} \nabla p + \nu \nabla^2 \vec{V} + \vec{g} \frac{\Delta \rho}{\rho} \quad \text{Eq. 3-2}$$

The influence of gravity can cause a slight bending of the interface of the two streams, thereby increasing the laminar diffusion surface when the densities of the two mixing streams are different. Therefore, this numerical model includes gravitational effects. The density differences that cause these are also affected by the temperature change induced within the reaction itself. However, these are insignificant. Consider that the total change in density ($\Delta \rho$) is a function of the change due to species/concentration ($\Delta \rho_s$) and the change due to temperature ($\Delta \rho_T$):

$$\Delta \rho = \Delta \rho_s + \Delta \rho_T \quad \text{Eq. 3-3}$$

These two terms are defined by Bejan [14] as:

$$\Delta \rho_s = \sum \beta_{s,i} (\rho_i - \rho_{i,ref}) \quad \text{Eq. 3-4}$$

$$\Delta \rho_T = -\beta_T \rho_{ref} \Delta T \quad \text{Eq. 3-5}$$

where $\beta_{s,i}$ is the solutal expansion coefficient, $(\rho_i - \rho_{i,ref})$ represents the density change of the dissolved component (ethanol), and β_T is the thermal expansion coefficient. To

compare the impact of each term in the buoyancy force using non-dimensional analysis, the ratio of the thermal Rayleigh number and solutal Rayleigh number are evaluated:

$$\frac{Ra_T}{Ra_s} = \frac{g\beta_T(\Delta T)L^3/\nu k}{g\beta_s(\rho_i - \rho_{i,ref})L^3/\nu D} \quad \text{Eq. 3-6}$$

where ν is the dynamic viscosity of mixture, k is thermal conductivity, L is a characteristic length, and D is the mutual diffusion coefficient.

This ratio reduces to:

$$\frac{Ra_T}{Ra_s} = \frac{\beta_T(\Delta T)D}{\beta_s(\rho_i - \rho_{i,ref})k} \quad \text{Eq. 3-7}$$

The values of β_T for ethanol and water are 0.0011 K^{-1} and 0.00021 K^{-1} , respectively, at room temperature. From the first thermodynamic law analysis, the maximum ΔT will be less than 2 K. The diffusion coefficient is approximately 1×10^{-9} . If we assume the concentration dependency of the solution to be linear (according to Boussinesq approximation), then, $\beta_s(\rho_i - \rho_{i,ref})$ will be approximately 0.22 at room temperature. Using the ethanol thermal conductivity of $0.17 \text{ W/m}\cdot\text{K}$, **Eq. 3-7** is evaluated to be approximately 5×10^{-11} . This confirms that temperature has a negligible effect on the gravitational effects in this system. Therefore, this model excludes the thermal component of the buoyancy term.

$$\text{Species equation} \quad \nabla \cdot (\rho \vec{V} Y_i) = -\nabla \cdot \vec{J}_i \quad \text{Eq. 3-8}$$

$$\text{Fick's law} \quad \vec{J}_i = -\rho D_{i,m} \nabla Y_i \quad \text{Eq. 3-9}$$

where $D_{i,m}$ and Y_i are mass diffusion coefficient and mass fraction of species i in the mixture, respectively.

$$\text{Energy equation in fluid} \quad \nabla \cdot (\vec{V}(\rho E + p)) = \nabla \cdot \left(k \nabla T - \sum_i h_i \vec{J}_i \right) + S_h \quad \text{Eq. 3-10}$$

where S_h is the volumetric heat source term. This source term was defined in order to apply the heat of mixing. The enthalpy of mixing of water and ethanol was experimentally measured by Boyne et al.[54]. As was suggested by Peeters [50], a sixth-order polynomial (Eq. 11) was fit to this data in order to predict the enthalpy of mixing for different alcohols:

$$\Delta H^e = C_{6/1} X_W^6 X_A + C_{1/1} X_W X_A + C_{1/2} X_W X_A^2 \quad \text{Eq. 3-11}$$

where X_W and X_A are mole fraction of water and alcohol respectively. For ethanol, $C_{6/1}$, $C_{1/1}$, and $C_{1/2}$ are -10.6, -1.2, and 0.1 (KJ/mol of alcohol), respectively.

In the binary system of water and alcohol, $X_W = 1 - X_A$. Furthermore, ΔH^e can be defined in terms of alcohol mole fraction. In this way the volumetric heat source term (W/m^3) is defined as:

$$S_h = \frac{dH_{mix}}{dt} = \frac{dH_{mix}}{dX_A} \frac{dX_A}{dx_i} \frac{dx_i}{\partial t} = \frac{dH_{mix}}{dX_A} (\nabla X_A \cdot \vec{V}) \quad \text{Eq. 3-12}$$

A UDF was written to apply this equation in the Fluent model used in this study.

$$\text{Energy equation in solid} \quad \nabla^2 T_s = 0 \quad \text{Eq. 3-13}$$

3.3.3 Boundary Conditions

Boundary conditions of the flow field applied to the inlets are:

$$\dot{m}_{in,1} = \dot{m}_A, \quad \dot{m}_{in,2} = \dot{m}_W \quad \text{Eq. 3-14}$$

where \dot{m}_A and \dot{m}_W are ethanol and water mass flow rates. Outflow boundary condition was applied at the outlet of the channel and no-slip boundary condition was applied on the microchannel walls.

Boundary conditions of the species applied to the inlets are:

$$Y_A|_{in,1} = 1 \quad , \quad Y_W|_{in,2} = 1 \quad \text{Eq. 3-15}$$

On the microchannel walls, zero-flux of both species was applied:

$$\left. \frac{\partial Y_i}{\partial n} \right|_{wall} = 0 \quad \text{Eq. 3-16}$$

For thermal field, all the exterior surfaces of the chip were exposed to convection boundary condition:

$$-k \frac{\partial T_s}{\partial n} = h(T_s - T_\infty) \quad \text{Eq. 3-17}$$

A convection coefficient of $20 \text{ W/m}^2 \cdot \text{K}$ was applied to the thin glass surface, and a convection coefficient of $10 \text{ W/m}^2 \cdot \text{K}$ was applied to all other surfaces. T_∞ for all convection surfaces was the room temperature set at 300K . Additionally, the inlet temperatures were set at room temperature.

3.3.4 Analysis of Numerical Results

This model was evaluated using a combination of tetrahedral and hexagonal meshing. Nodal temperature information was exported from Fluent to MATLAB (MathWorks, MA, USA) for visualization and further analysis. In addition to developing temperature maps of the device, predicted thermopile voltages for many scenarios were also calculated. This was achieved by extracting the simulated temperatures at the location of each of the 50 junction pairs and applying the following conventional thermopile voltage equation:

$$\begin{aligned} \Delta V &= \sum_{i=1}^n S_A (T_{2,i} - T_{1,i}) + S_B (T_{1,i} - T_{2,i}) \\ &= (S_A - S_B) \sum_{i=1}^n (T_{2,i} - T_{1,i}) \end{aligned} \quad \text{Eq. 3-18}$$

where $T_{2,i}$ is the temperature at the i 'th measuring junction and $T_{1,i}$ is the temperature at i 'th reference junction of the thermopile in the actual device, S_A and S_B are the Seebeck coefficients of Sb ($47 \mu\text{V/K}$) and Bi ($-72 \mu\text{V/K}$), respectively, and n is the number of junction pairs.

3.4 Results and Discussion

3.4.1 Shifting the Mixing Location by Adjusting the Flow Ratios

The purpose of adjusting the flow ratios between the two streams was to control the position of the water/ethanol mixing interface. This was demonstrated experimentally, as shown in **Figure 3-3**. As was expected, the profile of the interface was found to be a function of flow ratio only - essentially independent of the total volumetric flows of the two streams.

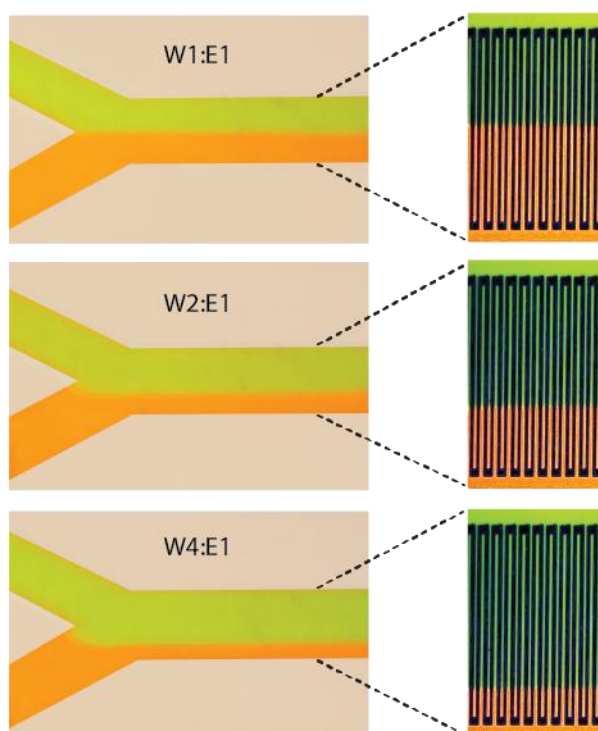


Figure 3-3: Photographs of three images of different flow configurations within the microchannel. Coloring dye and image enhancing was used to better visualize the flow streams. The images on the left are photos of a microfluidic device without the thermopile; those on the right are of a device with a thermopile positioned as in **Figure 3-1c**. These latter photos are high-zoom to show the thermopile detail with respect to the liquid flows.

3.4.2 Bolus Mixing

Thermopile output for injections of a 5 μl ethanol sample was collected at different volumetric flow rates through the microchannel. A representative data set is shown in **Figure 3-4** for total volumetric flow rates of 100, 200, and 400 $\mu\text{l}/\text{min}$ in the microfluidic device (which corresponds to fluid velocities on the order of 5, 10, and 20 mm/s). The peak height of each signal corresponds to the maximum change in the average temperature detected by the thermopile, and the area under the curve corresponds to the total thermal impact of the bolus injection.

For each, the constant volumetric flow rate for the Y-channel inlet that experienced the bolus injection was $\frac{1}{4}$ that of the inlet with the steady water stream (W4:E1). Thus, the water/ethanol mixing interface would be close to the reference junctions. This will also stretch each of the ethanol plugs to approximately 35mm in length (ignoring Taylor dispersion). At the three shown flow rates, the transit times between when the front of the ethanol plug enters the Y-junction and when the trailing end of the plug moves beyond the downstream end of the thermopile junctions are on the order of 12, 6, and 3 seconds, respectively. The corresponding thermopile signal¹ exhibits an expected lag, which is caused by the transit time for the heat to travel through the coverslip and polyimide film into the thermopile sensor.

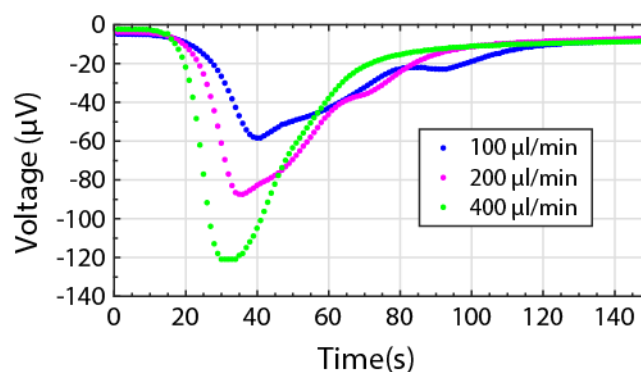


Figure 3-4: Thermopile output for a bolus injection of ethanol.

3.4.3 Continuous Mixing for a Steady State Response

To characterize the effect of the operating parameters, a series of continuous-flow experiments were performed as detailed above in the Experimental Procedures section.

As is shown in **Figure 3-5**, the thermopile voltage responded sharply to changes in the

¹ “The signal-to-noise ratio (SNR) for ethanol detection was approximately 50:1 for low ethanol concentration (10% V/V). The maximum noise in the signal was on the order of 50 nV. For the bolus ethanol measurements, the standard deviation was on the order of 5 µV.”

reaction zone location.

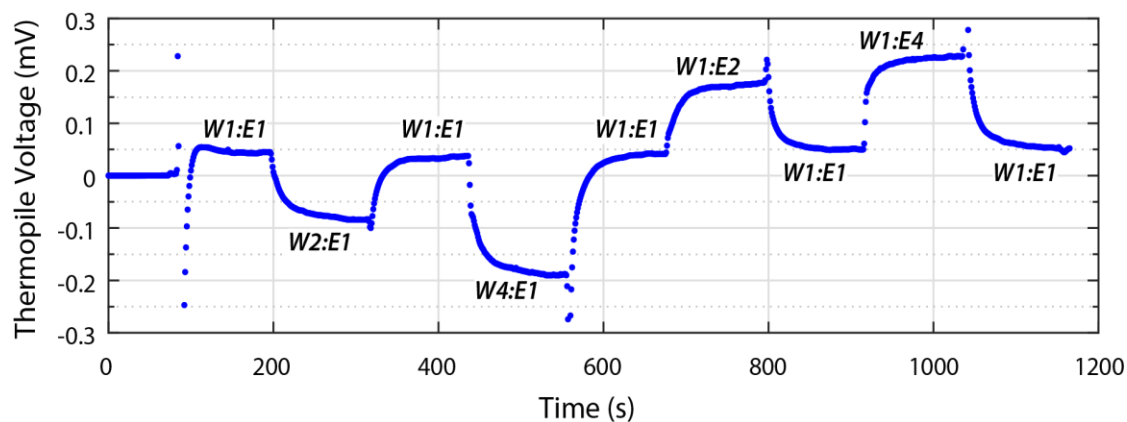


Figure 3-5: For the continuous-mixing experiments, the two inlet syringe pumps were programmed to change the flow ratios of the two liquid streams and regular intervals. For this thermopile output data shown here, the total volumetric flow rate for both streams combined was 200 $\mu\text{l}/\text{min}$.

3.4.4 Validation of the Numerical Model

In order to expand the parametric study beyond what mixing and thermal data could be obtained experimentally, a Fluent model was developed as detailed above in the Numerical Simulation section. Representative plots of the concentration and the temperature profiles are shown in **Figure 3-6**.

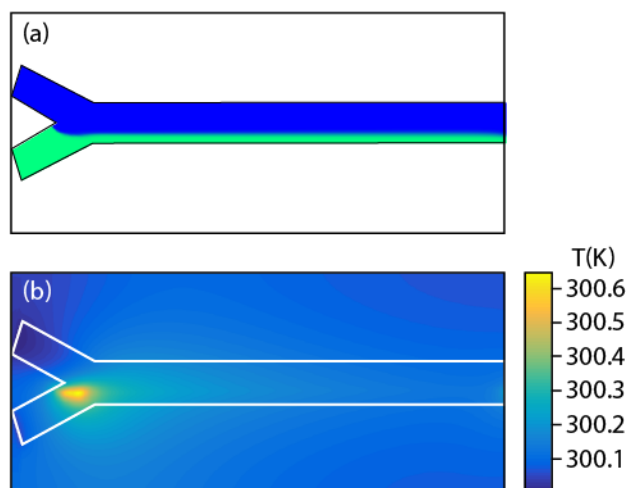


Figure 3-6: Representative results from the numerical simulations of the water/ethanol mixing. (a) shows the concentration distribution, and (b) shows the temperature distribution for the specific case of W4:E1 @ 400 $\mu\text{l}/\text{min}$ total volumetric flow.

The distinct similarities in the interface profiles observed in the experimental and the numerical results are shown qualitatively in **Figure 3-7**.

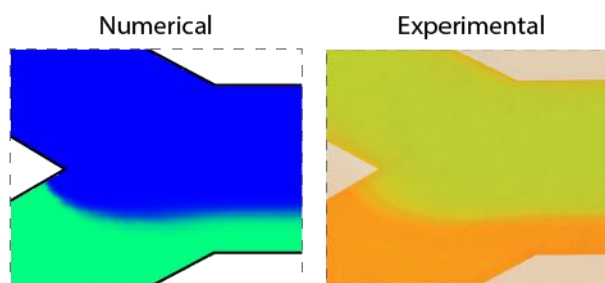


Figure 3-7: A comparison between the Y-junction flow interfaces for a W4:E1 flow ratio for the numerical (detail from **Figure 3-6a**) and the experimental (detail from **Figure 3-3**) results reveals strong qualitative correlation.

To validate the numerical model from a thermal performance perspective, the thermopile junction temperatures were extracted from multiple simulations and converted into a voltage using **Eq. 3-13** as described above. The actual (transient, but stabilized) and the simulated (steady-state) voltages are compared in **Figure 3-8**. This excellent

agreement across a range of flow conditions suggests that the numerical model can be trusted to precisely describe the real-world response of the physical system. With this model validated, it has been used to further explore the parametric dependencies of device performance.

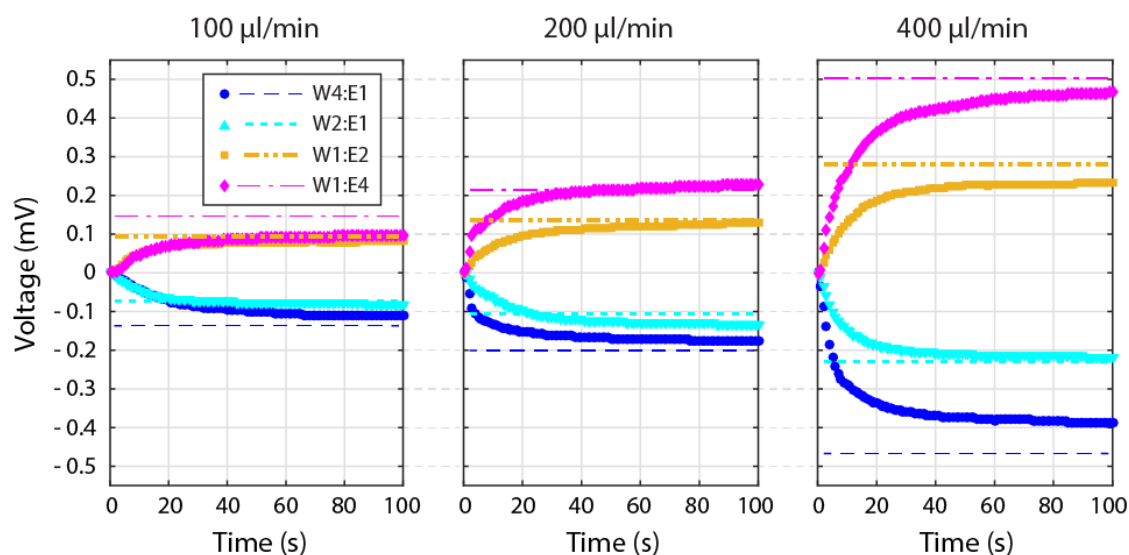


Figure 3-8: A comparison between the numerical and experimental results for four flow ratios at each of three flow rates (12 total combinations). Each graph corresponds to a specific total volumetric flow rate (W+E); each curve within each graph corresponds to a different flow ratio. The discrete points indicate the experimental data; the dotted/dashed lines indicate the corresponding numerical data. To filter out the effect of baseline drift in the experimental data (observable in **Figure 3-5**), the y-axes for these graphs define 0mV to be the W1:E1 condition (for both the experimental and numerical results). To compare the rise times for all conditions, the x-axes for these graphs define 0s as the last moment of stabilized W1:E1 voltage before changing to its new stabilized voltage at a different flow ratio (e.g. 196, 436, 675, and 915 seconds in **Figure 3-5**).

3.4.5 The Relationship between Flow Rate and Optimum Thermopile Location

Intuitively, the rate of water/ethanol mixing will be highest at the point where the two pure flow streams make first contact with each other; it is here that the diffusion distance between the two species is essentially zero. **Figure 3-6b** confirms that the greatest heat generation does occur at the beginning of the water/ethanol interface.

Because of the common-mode thermal rejection characteristic of the thermopile – which enables it to measure such miniscule temperature perturbations – only the asymmetry in the temperature profile will be detected. There are a number of factors, that determine the magnitude and location of that heat generation, as well as its advection and conduction through the liquid and the device materials before the heat arrives at the thermopile.

Rightly assuming that a highly-asymmetric flow will result in the largest thermopile voltages, the simulated thermopile voltage was examined as a function of its hypothetical location along the microchannel length for a range of flow rates. **Figure 3-9** shows a sampling of these numerical results.

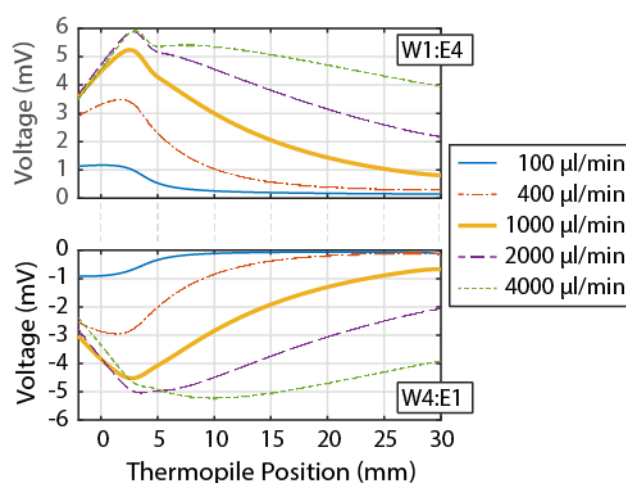


Figure 3-9: The predicted thermopile voltage for two highly asymmetric flows (W1:E4 and W4:E1) as a function of thermopile position along the microchannel. The x-axis denotes the distance between the center of the thermopile (which is 10 mm in length) and the base of the Y-junction channel where the two streams first meet.

Three trends are revealed through this examination:

1) Max/min voltage: As the flow rate increases, the maximum thermal asymmetry increases. At low flow rates, this increase in maximum voltage is rapid; the maximum voltage increase with increasing flow gradually diminishes until it reaches an

approximate maximum. The early increase is attributed to the increased heat generation caused by the growing rate at which ethanol and water molecules come in contact.

2) Peak location: As the flow rate increases, the thermopile location that would yield the maximum voltage shifts gradually downstream. This is attributed to thermal advection; the high flow carries more heat downstream.

3) Split peaks: The W4:E1 voltage curve remains a single peak; however, at high flow rates the W1:E4 curve splits into two peaks – one of which stays at a fixed location, and the other which moves downstream with ever increasing flow. This is attributed in part to the difference in the thermal properties of the water and ethanol. The thermal diffusivity of ethanol is about half that of water; thus, heat will travel laterally through the water faster than through the ethanol. This will amplify the asymmetry of the initial temperature distribution when it occurs nearer to the water inlet, and will counter-act the asymmetry when the heat generation is nearer the ethanol inlet.

These results suggest that A) there is an optimum thermopile position for each flow rate, and B) this optimum position is also influenced by the flow ratio – since the flow ratio controls the degree of asymmetry but not the magnitude or advection of the generated heat. These influences have been carefully examined. **Figure 3-10** gives an example of how both of these effects can be observed simultaneously. In this set of graphs, the maximum possible voltage for a given flow rate and flow ratio are shown – overlaid with the location along the channel where that maximum voltage would be measured.

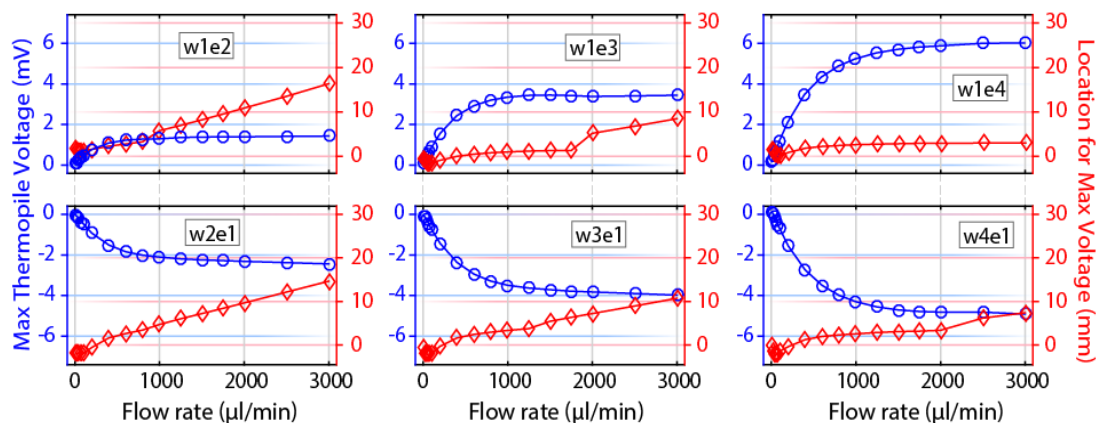


Figure 3-10: For each of these six representative flow ratios, the left-hand vertical axis indicates the maximum voltage as a function of flow rate; the right-hand vertical axis indicates where within the channel the thermopile must be to measure this maximum voltage.

These results reveal the following:

1) Optimum flow rate: For all ratios, increasing the flow rate to boost the thermopile voltage is helpful at low flow rates, but has quickly diminishing returns. Large flow rates are not practical if reagent or sample consumption has a significant cost.

2) Asymmetry: Greater thermal asymmetry results in a greater maximum voltage.

3) Location: For all ratios, the thermopile should be near the beginning of the microchannel for low flow rates. More importantly, the optimum location does not begin to change until some flow rate threshold is surpassed. This threshold – and the way in which the location changes with increasing flow rate – is specific to each flow ratio.

4) Thermal properties: Across the ratios, voltages are consistently higher when the water/ethanol interface is shifted to the water side of the microchannel. This is due to the difference in thermal properties.

These results suggest that lower flow rates are preferred over higher flow rates, since: A) the same thermopile location will yield the maximum sensitivity over a range of

flow rates, and B) increases in flow rate do increase the voltage signal, but by less and less.

Using data sets similar to those represented in **Figure 3-10**, a root mean square (RMS) algorithm was implemented in MATLAB to calculate the optimum thermopile location for several subsets flow rates. A significant result of that analysis is that the distinctly optimum location for all flow rates below 600 $\mu\text{l}/\text{min}$ is having the thermopile centered 1.5 mm downstream of the initial Y-junction interface. **Figure 3-11** compares thermopile performance at this location with performance when the thermopile is centered 15 mm from the Y-junction. Clearly, the thermopile essentially straddling the Y-junction will be much more sensitive at low flow rates. At high flow rates, though, the two locations are predicted to yield a comparable sensitivity.

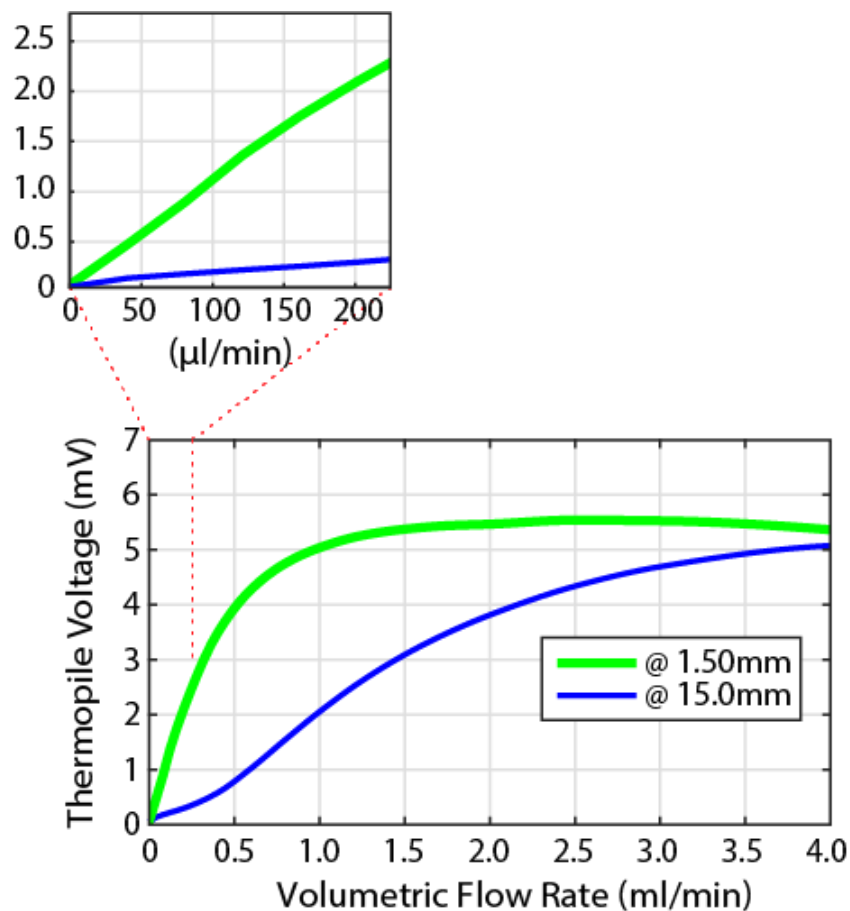


Figure 3-11: Comparison between the predicted thermopile voltage as a function of flow rate for two thermopile locations. The optimum configuration for low flow rates (<600 $\mu\text{l}/\text{min}$) has the center of the thermopile located only 1.5 mm downstream from the Y-junction. The inset reveals the linear relationship between the signal and flow rate at low flows. The flow ratio for this simulation is W1:E4.

A key result from this data is that – with the thermopile at this optimum low-flow location – the flow rate and the thermopile voltage are essentially proportional below about 500 $\mu\text{l}/\text{min}$. This suggests that the increased contact rate of the mixing species is the dominant factor in determining thermopile voltage at low flow rates.

3.4.6 Effect of Flow Ratio

Since the thermopile geometry used for these experiments is designed to measure asymmetry, certainly the more extreme flow ratios will provide a greater sensitivity to

temperature change. The effect of flow ratio, though, is not linear – nor is it reciprocal (e.g. $V_{W1:E2} = -V_{W2:E1}$). **Figure 3-12** shows this for a wide range of flow rates. The nonlinearity underscores the relationship between the flow ratio and the resulting thermal asymmetry within the device, as well as the effect of the different thermal properties of the water and the ethanol.

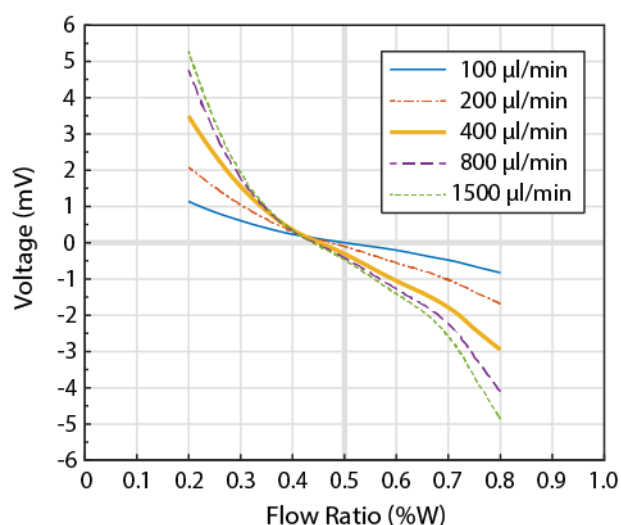


Figure 3-12: Thermopile voltage as a function of flow ratio, for several flow rates (W+E). When the mixing interface is shifted toward the water inlet, the voltage will be more positive; toward the ethanol inlet, more negative.

These results are of particular interest when considering which flow direction to move the mixing interface for best detection sensitivity. At moderate flow asymmetry up to about +/- 20% (i.e. 0.5 +/- 0.2), the thermopile will detect greater thermal asymmetry if the interface is shifted toward the ethanol inlet. With more extreme flow asymmetry (more than +/- 20%), shifting the mixing interface toward the water inlet will yield higher signals. As stated previously, this is due to the different thermal and flow properties of the two fluids. Since these particular constituents (water and ethanol) are representative of a great variety of liquid pairings of interest, further exploration of the impact of each

of the specific properties (viscosity, thermal conductivity, heat capacity, etc.) seems beyond the scope of this present study.

3.5 Conclusion

The scope of this work has been to explore the design and operational parameters that will maximize the sensitivity of microfluidic thermal sensors. This work has relied upon both experimental and numerical methods, using as a representative system the sensing of the water/ethanol heat of mixing in a Y-junction microchannel. The findings of this study can be summarized as follows:

1. There is an upper limit on the flow rate. Increasing the flow does increase the magnitude of the thermal signal, but primarily only at low flow rates. For the device specifically studied here, this upper limit is about 500 $\mu\text{l}/\text{min}$. If the sensor can detect an acceptable signal at 200 $\mu\text{l}/\text{min}$ or below – even better.
2. The thermopile should be placed in very close proximity to the source of heat; the lower the flow rate, the more important this is. Thermal advection does occur, but at flow rates below 500 $\mu\text{l}/\text{min}$ this is unimportant with respect to thermopile placement.
3. Asymmetry in the heat generation vs. concentration relationship can be leveraged to maximize the temperature difference between the two thermopile junction sets.
4. Greater sensitivity is obtained when the co-flow interface is shifted away from the fluid that is more resistant to heat transfer, such as with a higher viscosity and/or lower thermal diffusivity.

It is hoped that an understanding of the findings of this research and the process by which the conclusions were made will support others within the research community in the continuing advancement and development of many types of microfluidic thermal detection systems.

CHAPTER 4

3-D NUMERICAL SOLUTION OF EXOTHERMIC MIXING OF WATER/ETHANOL IN Y-SHAPED MICROCHANNELS

This chapter is the supplementary part of chapter 3 for the further explanation and justification of the model used in the previous chapter. Here, the focus is more on the flow and thermal field in the micromixer domain rather than the thermal field of exterior face of the device and the location of the sensor. Due to the complicated nature of the process, which involves the coupled transport of mass, momentum, heat, and species, it is worthy to dedicate a short chapter for some elaboration.

One interesting observation from the thermopile experiment was the non-zero signal for the equal volume flow rate of water and ethanol demonstrated in **Figure 3-5**. In this chapter, the reason for such an asymmetry and its root in the properties of water/ethanol mixture will be explained.

4.1 Introduction

Microfluidics has attracted researchers in the fields of chemistry, biology, and medical engineering due to low reagent consumption, small size, compatibility with micro total analysis systems (μ TAS), and excellent control over the process. High surface-to-volume ratio due to miniaturization in the microfluidics highlights the role of surface-dependent phenomena such as mass and energy diffusion flux, over the volume-dependent processes including volume flow rate and bulk reaction. Mixing of two or

more fluids is a generic process in microfluidics. Micromixers usually perform at laminar flow regime due to small characteristic length and operation at low volume flow rates. In the absence of "chaotic advection forces" at low Reynolds numbers, mixing happens mostly through diffusion and advection [55, 56]. Although considerable efforts have been dedicated to increase the mixing efficiency in micromixers by enhancing the mixing surface, (e.g. increasing the Reynolds number to reach vortex flow and engulfment flow [53, 55], modifying the geometry [57, 58]), in certain applications, slow diffusion facilitates the monitoring of the process in the micromixer and enables the supreme control over the process.

T- or Y-shaped micromixers consist of a simple microchannel design which guides two fluid streams into a side-by-side contact in a relatively high aspect ratio channel making it an ideal platform for investigating and monitoring the mixing behavior and concentration distribution. Kamholz et al. introduced this analytical device for investigating the molecular interactions, determining the molecular diffusion coefficients of the species, and quantifying the viscosity of the liquids. They used the collected fluorescence intensity data in conjunction with analytical models in order to extract the unknown properties of the fluids, such as diffusion coefficient and viscosity [59]. Micromixers with inlets located at different levels [18] of the channel or with more than two inlets create extra interfaces which can be used for additional simultaneous analysis in a single device.

These micromixers have been widely used as microreactor for performing reactions and chemical synthesis, extracting reaction rate constants [60], nanoparticle synthesis [61], detection [28, 62], calorimetry [44], and monitoring a process using a

variety of optical techniques [63, 64]. Recent advances in paper-based microfluidics have been integrated in Y-shaped micromixer to present a low-cost, pumpless microreactor operating by capillary force, and thus dismissing the large pumps often attached to the small microfluidic systems [65].

In T-micromixers, intense diffusion occurs at the interface of the streams where usually sharp variation of fluid properties such as species concentration, density and viscosity exist. As a result, a localized reaction zone makes it easier to target the reaction and mass distribution using optical techniques.

Majority of the studies are focused on the mass transfer and mixing performance including experimental, analytical [66], and numerical techniques [53, 55, 67]. Although the ultimate goal in microreactors is performing a process by controlled mass transfer, in many cases, heat transfer plays an unavoidable role. Temperature-dependent reaction constants and fluid properties involved in biological reactions, such as PCR and DNA melt, are just a few examples for the importance of heat transfer in microreactors. However, fewer studies have been focused on the heat transfer in these devices. As explained by Kowalski et al. [44], in a simple microreactor, there are much more flux surfaces and heating domains as compared to mass transfer domain. Xu et al. investigated the thermal mixing of two streams of water with different temperatures in a T-shaped micromixer [68]. They divided the domain into T-junction and mixing channel and developed a 2-D analytical model for the mixing channel. Pradre et al. conducted an experimental study of an exothermic acid-base reaction in a Y-shaped microreactor and extracted the thermal field of the chip from infrared thermography data [69]. Kowalski et al. simulated a 3-D model of a similar configuration with two streams containing diluted

solution of an acid and a base. They obtained the concentration and thermal field for determining the optimum location of Nanohole array (NHA) sensor used for calorimetry [44].

In addition to the examples of the heat generated by a reaction or mixing of two streams of different temperatures, the source of heat in the micromixers can be from an endothermic or exothermic mixing process. Unlike the chemical reactions, the absorbed or released heat comes from the rearrangement of intermolecular forces rather than the rearrangement of atoms. These mixtures are classified as non-ideal mixtures including the solution of a variety of organic and inorganic compounds in water. A well-known and ubiquitous class of non-ideal mixtures is water/alcohol mixture, which entails the breaking of hydrogen bonds between identical molecules and the formation of new hydrogen bond networks between dissimilar molecules. The binary mixture of ethanol/water shows abnormal behavior in terms of excess enthalpy, capacity, diffusivity, density, and viscosity [46, 49, 50, 70, 71]. Exothermic mixing of water and alcohol has been recently studied experimentally for calorimetric application in a thermopile-based nanocalorimeter by Padovani [47] and in a Y-channel micromixer by Kowalski et al. [48]. Also, simultaneous near-infrared imaging of a micromixer filled with diluted ethanol and water was recently conducted by Kakuta et al. [64]. Computational Fluid Dynamics (CFD) can be a powerful tool for expanding knowledge about the heat and mass transfer occurring in the micromixers for a complicated process such as exothermic or endothermic mixing of fluids.

In this study, we apply a new 3-D numerical model of heat generation for the exothermic mixing of water and ethanol. Commercial software, Fluent (ANSYS,

Canonsburg, PA) was used to solve the conservation equations of mass, heat, momentum, and species in a Y-shaped micromixer. To incorporate the non-ideal properties of the mixture, a User Defined Function (UDF) was written for applying the concentration-dependent heat of mixing based on experimental data and a fitted equation introduced by Peeters [50]. Another UDF was written to apply the abnormal viscosity and density of the mixture according to what was proposed by Mauri [53], who was one of the few researchers taking these non-ideal properties into account. The results of model will be compared against experimental data obtained from a similar geometry using thermopile sensors. Finally, an analytical solution will be suggested for describing the two-dimensional velocity in the fully-developed pressure-driven channel filled with two immiscible fluids emphasizing on the important role of the viscosity in determining the location of the interface and intensifying the asymmetrical thermal map when the flow rates are equal.

4.2 Methods

4.2.1 Heat of Mixing

In the water/ethanol mixing process, the interactions between solute-solute, solute-solvent, and solvent-solvent are involved [72]. The transition between the dominance of these interactions at different mole fractions causes irregular behavior in the mixture properties, including the enthalpy, density, and viscosity at different mole fractions of the solvent. Conventional calorimetric methods were used to obtain the heat of mixing in terms of mole fraction of solvents at room temperature [54] and investigating it at different temperatures [73]. Since then, numerous efforts have been dedicated to explaining these irregular behaviors using various experimental techniques

[49, 71, 72, 74]. However, there is no simple model for describing all the nuances of water/alcohol mixture, and it is yet an active area of research. Therefore, experimental data and the correlation introduced by Peeters were selected as the base for describing the heat of mixing.

In this dissertation, water/ethanol mixture was selected as a representative source to generate a local heat in a micromixer and to study the propagation of the heat. The modeling was performed using a continuum level numerical technique (Finite Volume Method), and any molecular level model is out of the scope of this study.

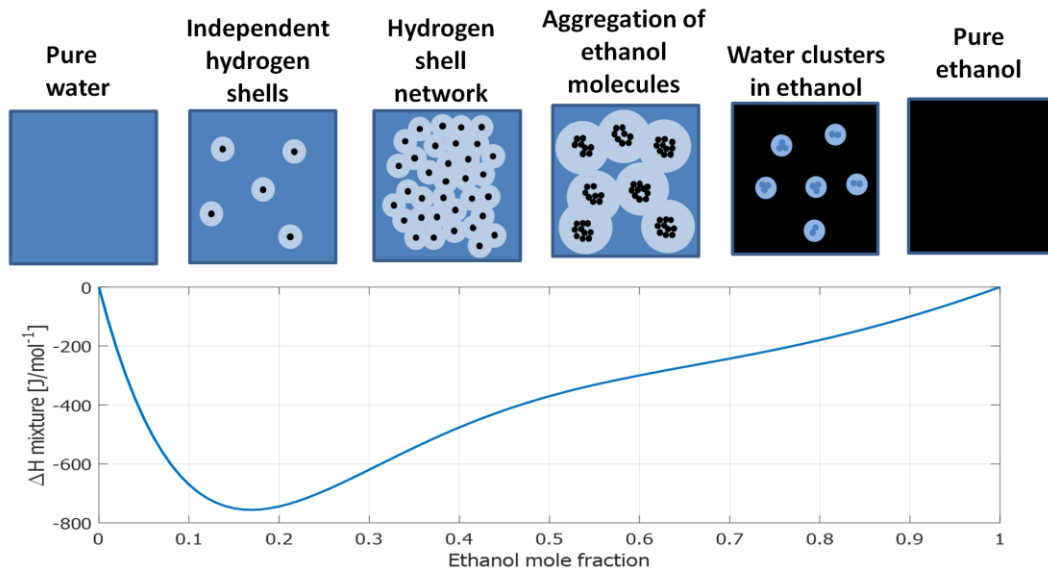


Figure 4-1: a) The schematic of the transition in the structure of water/ethanol mixture (schematics were reproduced from [49] b) enthalpy of mixing based on the sixth order fitted equation of Peeters.

Two approaches were taken in order to apply the mole fraction dependent heat of mixing:

- A) Modifying the enthalpy of each computational cell by adding the enthalpy term based on **Eq. 3-11**
- B) Adding the enthalpy as a heat source explained in **Eq. 3-12**

Fluent does not have any specific model for including the heat of mixing. Instead, it allows the user to customize the model by functions written in C language and dynamically executed in Fluent. In this way, the users are able to access the solver data using predefined macros and functions provided by Fluent and apply it for their special need [52]. Applying **Eq. 3-11** requires a simpler code compared to **Eq. 3-12**. The result of both methods for the flow rate of 100 $\mu\text{l}/\text{min}$ is plotted in **Figure 4-2** for different flow ratios along the length of the channel. The results are very close between all the flow ratios except for W1E1 as can be seen in the figure.

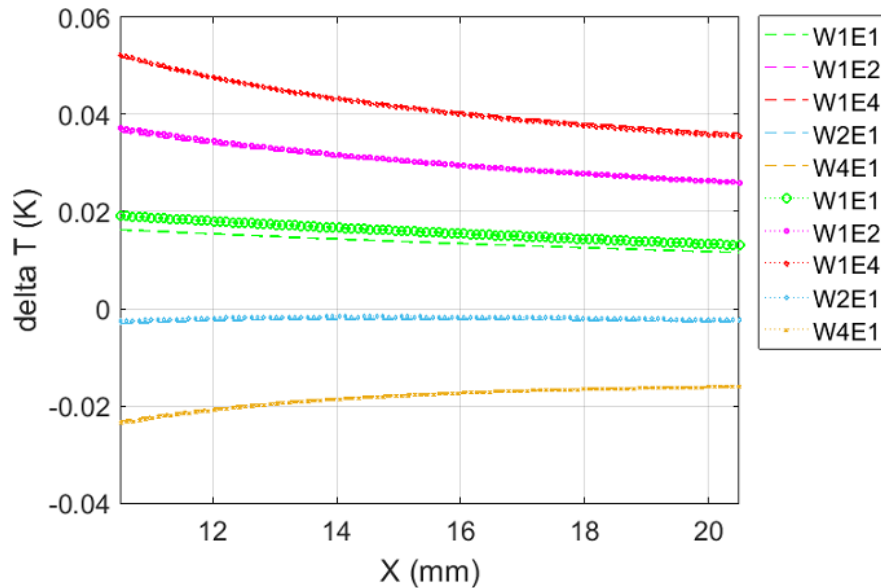


Figure 4-2: Temperature difference between two lines overlaying the thermopile location calculated using enthalpy modification (dashed lines) and source term (dotted lines with markers) for different ratios of water and ethanol. The temperature difference was plotted all along the channel (as indicated in Figure 3-2).

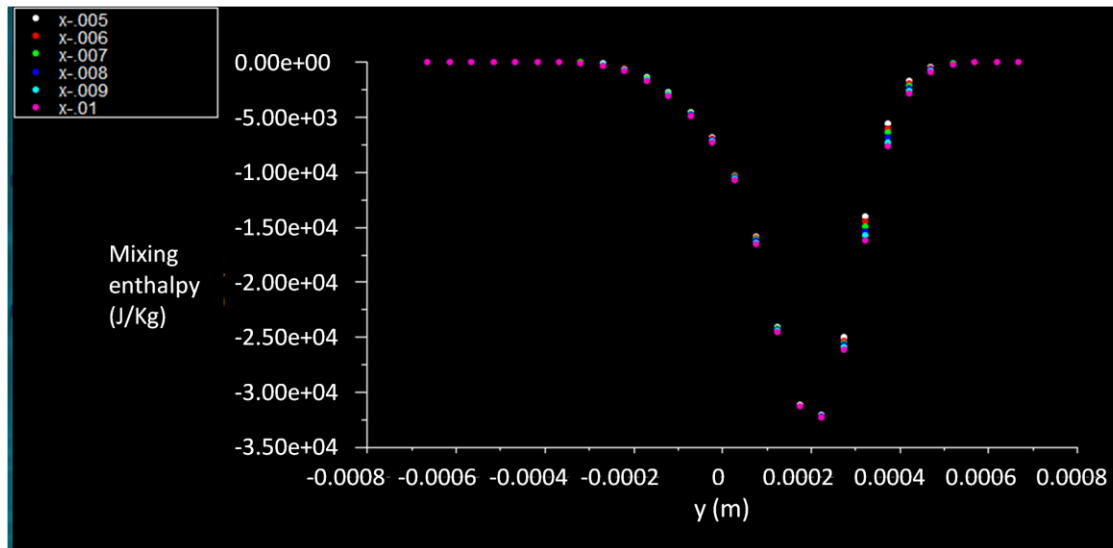


Figure 4-3: Enthalpy of mixing plotted at different sections of the channel.

Despite the similarity of the results, the source term method better describes the physics of the problem. Water and ethanol mix as long as they are in contact; however, when they are mixed and the energy is released in the first contact, it is expected that they release less energy. When the enthalpy of mixing and the source term were plotted at different cross sections of the channel, the decreasing trend was observed for the source term, while for the enthalpy of mixing, it was almost the same at different sections:

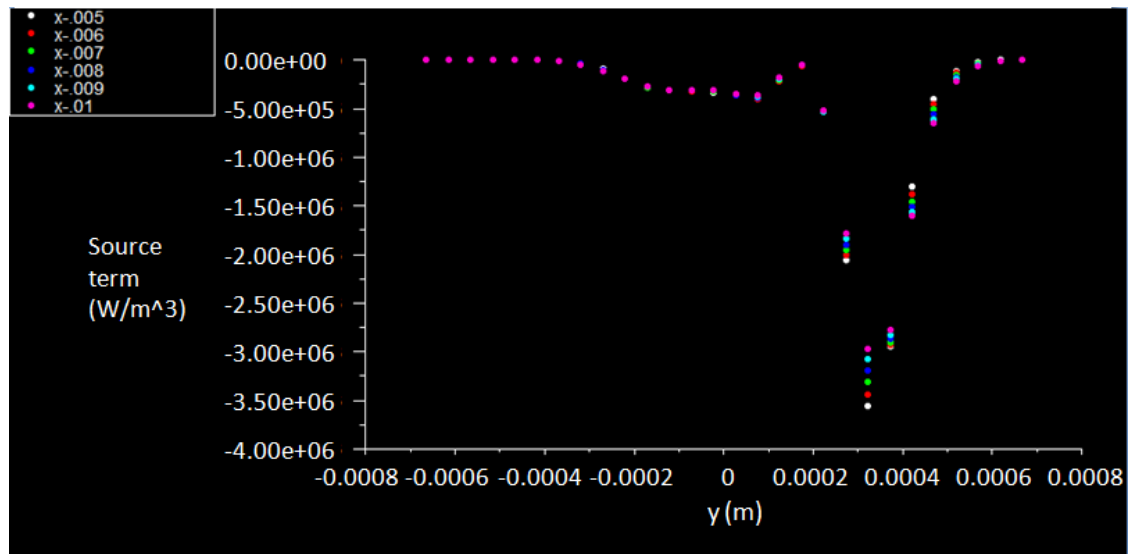


Figure 4-4: Source term corresponding to the heat of mixing, plotted at different sections of the channel.

Therefore, the source term method was chosen for the analysis.

4.2.2 Viscosity and Density

As explained in the previous chapter, abnormal viscosity of the water/ethanol mixture has a considerable influence on the result. The concentration-dependent viscosity based on the experimental data is shown in **Figure 4-5**. To emphasize the abnormality of the viscosity, conventional linear relationship, which is typical for ideal mixtures, is plotted as well. As it can be seen, the deviation from the regular mixture relationship is more evident in the viscosity, compared to the density. However, both relationships were applied as a customized UDF in the software.

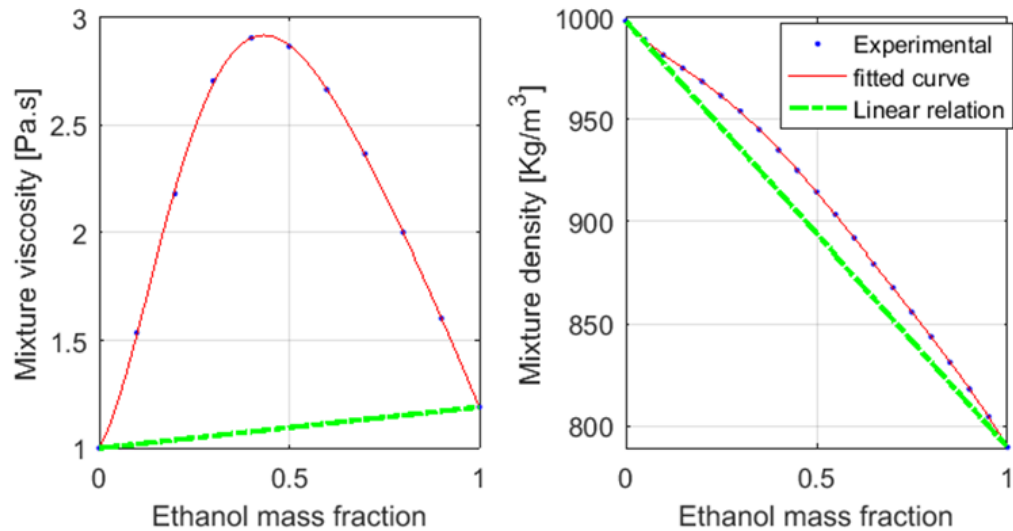


Figure 4-5: Viscosity and density of the mixture as a function of ethanol mass fraction (figure reproduced from Mauri).

4.3 Discussion

4.3.1 Sources of Asymmetry

In the experimental data, it was observed that for the equal ratio of water and ethanol (W1E1), a detectable signal was observed despite the fact that the sensor was placed symmetrically on the channel region, while the expectation was a very negligible signal. Simulations were performed to investigate the source of asymmetry. Despite the similarity, there are mismatches in the physical properties of water and ethanol. However, the share of each property in giving rise to the asymmetry is not the same. In order to understand the role of each parameter, the properties of the water and ethanol were reversed individually or jointly. Important properties of water and ethanol playing a role in the behavior of the system are provided in **Table 4-1**.

Table 4-1: Material properties of water and ethanol

Properties	Water	Ethanol
Density (kg/m ³)	998	790
Viscosity (Pa · s)	0.001003	0.0012
Thermal Conductivity (W/m · K)	0.6	0.182
Specific Heat (J/kg · K)	4182	2470

First of all, the heat of mixing curve as it was shown in **Figure 4-1** is not symmetric and has a peak at mole fraction of 15%. In this way, the highest enthalpy of mixing occurs at the water-rich region. Therefore, the mole fraction of water and ethanol was reversed in **Eq. 3-11**.

Another subtle factor is the difference between the viscosity of water and ethanol. The fluid with lower viscosity moves faster due to its lower friction. Subsequently, for a heat source containing a velocity term (**Eq. 4-12**) or an additional enthalpy multiplied by a velocity term (left side of **Eq. 4-10**), it results in higher released heat. This relationship between the mean velocity and viscosity was observed for W1E1:

$$\mu_1 |\bar{V}_1| = \mu_2 |\bar{V}_2| \quad \text{Eq. 4-1}$$

This relationship is a very good approximation of the behavior of side-by-side flows when the aspect ratio of the channel is high. Considering the continuity, **Eq. 4-1** results in an important relationship between the width, flow rate, and viscosity:

$$\mu_1 \frac{\dot{V}_1}{w_1 t} = \mu_2 \frac{\dot{V}_2}{w_2 t} \rightarrow \frac{\dot{V}_1 \mu_1}{\dot{V}_2 \mu_2} = \frac{w_1}{w_2} \quad \text{Eq. 4-2}$$

where \dot{V}_1 and \dot{V}_2 are the volumetric flow rates of each fluid, w_1 and w_2 are the width of each stream, and t is the depth of the channel. This implies that for the same flow rate \dot{V} , the interface of water and ethanol shifts to the lower viscosity stream which is the water side in this case:

$$w_W = \frac{w}{\frac{\mu_W}{\mu_W} + 1} \cong 0.455w \quad \text{Eq. 4-3}$$

So, width of the channel occupied by water will be $0.455w$ instead of $0.5w$. Therefore, for a sensor located symmetrically over the width of the channel, the heat source is closer to the water side. The combination of the enthalpy curve and viscosity mismatch is responsible for most of the asymmetry behavior.

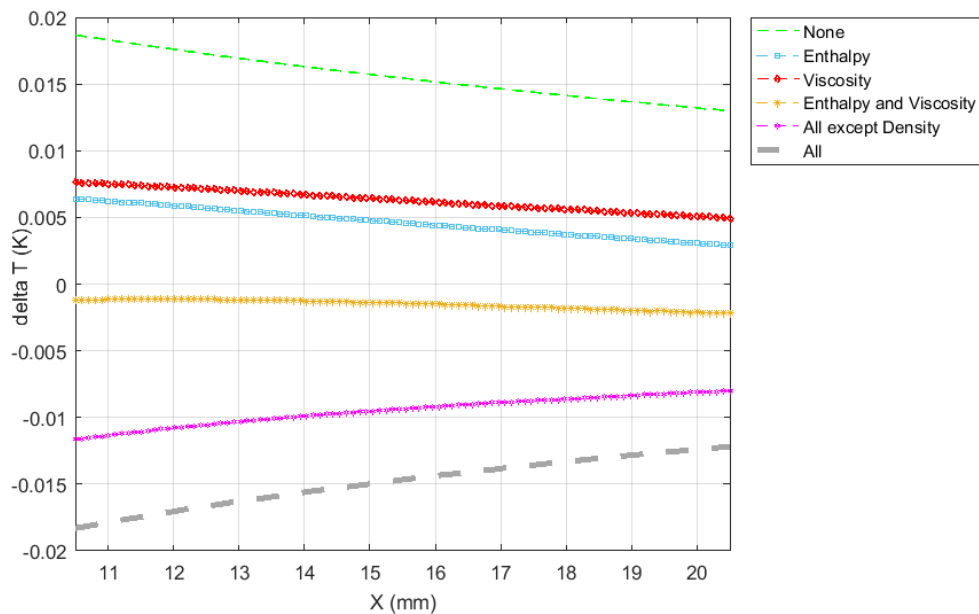


Figure 4-6: Impact of reversing the factors accounting for the asymmetry in the temperature of the co-flow. Again, temperature difference between two lines overlaying the thermopile location was plotted over the length of the channel

As can be seen in the **Figure 4-6**, the temperature difference coming from the combination effect of viscosity and enthalpy equation is less than the difference caused by adding each of them separately. In other words, the superposition principle is not valid. This is logical given that the change in the viscosity influences the velocity, which directly affects the rate of enthalpy.

The phenomena can be better explained using the non-dimensional group parameters defining the dynamical similarity of the two streams. In order to expect that the two flows behave the same under the forced convection, dynamical similarity should exist between them. The complete dynamical similarity implies that both Reynolds number, $Re = UD_h/\nu$, and Péclet number, $Pe = UD_h/\alpha$, are equal for them. An equivalent of this condition is the equality of Re and Prandtl number, $Pr = \nu/\alpha$. Prandtl number is the ratio of diffusivity of momentum to diffusivity of heat and is a property of the fluid [15]. The Pr is 7 and 16 for water and ethanol, respectively. Therefore, even for the same Reynolds number and under the same thermal condition, the thermal behavior of the two fluids is never identical. However, the non-dimensional numbers are good measures for predicting which stream gets hotter.

Hydraulic diameter of the two streams is almost the same:

$$\frac{D_{h,W}}{D_{h,E}} = \frac{\frac{2w_w t}{(w_w + t)}}{\frac{2w_E t}{(w_E + t)}} \approx 1.01 \quad \text{Eq. 4-4}$$

The ratio of Reynolds numbers can be approximated using **Eq. 4-1**:

$$\frac{Re_W}{Re_E} = \frac{\rho_W |\bar{V}_W| D_{h,W} \mu_E}{\rho_E |\bar{V}_E| D_{h,E} \mu_W} = \frac{\rho_W |\bar{V}_W| \mu_W \mu_E}{\rho_E |\bar{V}_E| \mu_E \mu_W} = \frac{\rho_W}{\rho_E} \left(\frac{\mu_E}{\mu_W} \right)^2 \quad \text{Eq. 4-5}$$

According to **Eq. 4-5**, the two fluids in a co-flow occupy the same width of the channel and obtain the equal Re when their density ratio equals the square of their viscosity ratio. Inserting the densities and viscosities, $Re_W \cong 1.8Re_E$. Subsequently, considering the Pr of each fluid, $Pe_W \cong 0.76Pe_E$ is valid. This explains why even with source term with a pick occurring at the ethanol side, the water side is still slightly hotter (**Figure 4-7**). In the flow with smaller Pe , conduction (molecular transport process) is more important than convection. Therefore, heat conducts more from a source term located at the interface of the two streams to the stream with smaller Pe .

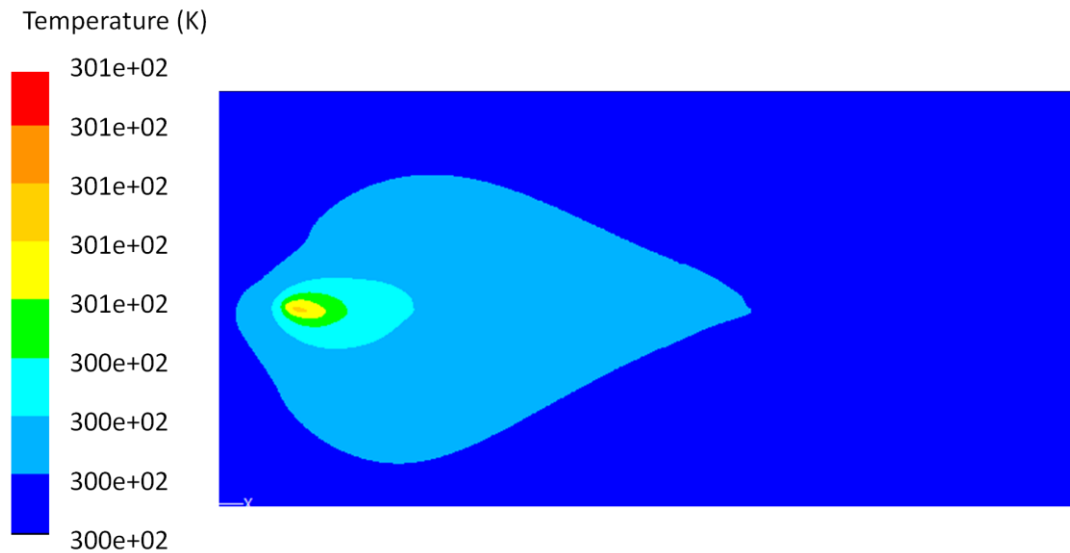


Figure 4-7: Thermal contour of the microchannel chip when the source term is defined in a way that its pick is toward the ethanol side (water and ethanol sides are as demonstrated in **Figure 3-2**).

4.4 Conclusion

The discussion made for the justification of the non-zero thermopile signal at the ratio W1E1 is very important, especially for the design of a thermoelectric sensor.

Establishing the same flow and heat convection between the two streams in the co-flow is somehow crucial for benefiting the common mode rejection in the thermopile sensor.

CHAPTER 5

COUNTER-FLOW THERMAL GRADIENT MICROFLUIDIC DEVICE FOR THERMAL STABILIZATION

5.1 Introduction

Counter-flow microfluidic chips and their application in stabilizing the thermal microsystems are the subject of this chapter. Microfabrication and rapid prototyping methods will be used to fabricate counter-flow microfluidic chips. The fabrication process of a high precision counter-flow chip will be explained in elaborate detail. Infrared thermography will be used to investigate the thermal behavior of the fabricated devices under thermal gradient at a wide range of volumetric flow rates. Influence of the interlayer material in the performance of the counter-flow will be investigated by fabricating the composite counter-flow chips with interface materials of different thermal conductivity levels. The performance of the devices will be compared with non counter-flow, or as it is termed here, the *direct-flow* chips.

5.1.1 Flow-induced Effects

In chapter 3, the unwanted impact of convection in thermal behavior of a thermal gradient microfluidic chip was discussed. In this chapter, the adverse impact of the flow in distorting the thermal distribution will be discussed, and counter-flow configuration as a way of dealing with this problem will be investigated.

In a thermal microfluidic device, rapid alteration of the sample fluid is possible through passing it from different thermal zones. This idea has been the principle of a wide variety of biological processes, among which continuous-flow PCR (CF-PCR) and spatial DNA melt are two well-known examples. CF-PCR systems can be classified into two categories. The first category is multiple zones CF-PCR, including three separate isothermal zones primarily introduced by Kopp et al. [6]. In such devices, thermal "cross talk" between the iso-thermal zones affects the performance of the device and limits the miniaturization [2, 75]. Contrary to the first category, Crews et al. used a single-zone temperature gradient design where fluid experiences the temperature change by passing across the isothermal lines. The sophisticated design of the channel geometry with respect to thermal gradient enforces the precise control over the residence time at distinct temperatures [9, 76]. The thermal gradient provides the ability of mapping the temperature of the fluid, which was successfully integrated into spatial DNA melt analysis [4, 77]. For such a system, the ideal temperature map is the one dictated under no flow condition, which is a linear thermal gradient. However, the flow passing isothermal zones causes variation in the temperature of the chip causing error in the analysis. The flow-induced effect can reach a level that limits the efficiency [3] and even the process time of both categories of devices.

Flow-induced effects in the thermal gradient microfluidic was extensively studied by Crews et al. [2] using both experimental and numerical methods. They demonstrated how the flow can affect the temperature by designing a serpentine channel with right angle bends along or vertical to isothermal lines (under no flow condition). Schematics of the pattern they used can be seen in **Figure 5-1**.

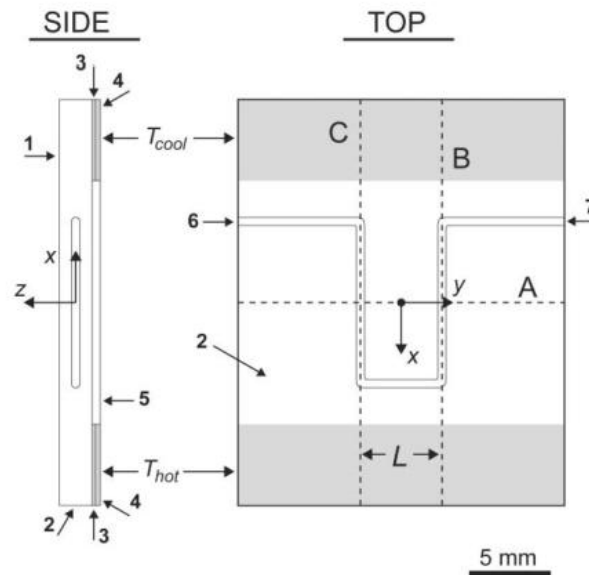


Figure 5-1: Geometry of the microchannel from the model depicting the pattern and its location with respect to the two heaters. a) side view b) front view [2]

They tested the thermal performance of the actual micorfabricated glass microfluidic chip under the flow and with no flow conditions by analyzing the temperature difference between line B and line C, ΔT_{BC} , as a measure of distortion caused by the flow. CFD models were validated with IR themography of the chip surface. In this study, impact of important parameters such as volumetric flow rate, distance between the parallel channels, and the material properties of the substrate were investigated. According to **Figure 5-1**, the flow along lines B and C has opposite direction making a counter-flow. They demonstrated that the heat transfer between the two opposite streams can reduce the flow-induced distortion of the temperature distribution. The magnitude of this heat transfer depends on the resistance between the two channels, which is defined by the distance and material thermal conductivity of the substrate. This important outcome is the basis for designing the counter-flow microfluidic chip in order to deal with the adverse flow-induced effects. It suggests that a sophisticated design for

minimizing the resistance between the opposite streams is a promising approach for addressing the distortion due to flow.

Thomas et al. [75] expanded the parametric study of channel spacing to a series of bends creating a serpentine microchannel designed for 25 thermocycles similar to the microchannel fabricated by Crews et al [78]. They demonstrated the important role of channel spacing in the design of such devices. In another study by the same researchers, impact of operational parameters such as environment temperature, convection coefficient, and flow rate of the channel was investigated [3]. Their results show that flow rate is the most limiting parameter for efficiency or even possibility of PCR in these designs. The limit for the flow rate in their design was 1 ml/hr.

Distance between the centerline of the serpentine counter flow channels is restricted by width of the channels, which is limited by resolution of the fabrication process. In fact, in most of the 2.5-D microchannels, miniaturization is mostly done in the depth (simply by reducing the etch time or by laminating a very thin interlayer material in xurography). Additionally, the resolution of optical and IR systems limits the ability of characterization of very minute channels located very close to each other. However, if the two opposite streams of the channels are separated in the normal plane, the two counter-flows can be separated by a very thin layer, dismissing the need for very small channels. This design also allows for the design of a hybrid microfluidic in which the high thermal conductive material is used wherever it is required, while the lower conductive material (typical in transparent microfluidic chips) is used in the regions where thermal isolation is favorable.

5.2 Analytical Approach

It is very innate to regard a counter-flow microfluidic performing under the thermal gradient as a miniaturized heat exchanger. The concept of the heat exchanger has been discussed very thoroughly in heat transfer textbooks [1, 14]. Although treating the problem as a 1-D heat exchanger model has undeniable benefits in terms of explaining the phenomena and clarifying the key parameters in the design of a counter-flow microfluidic chip, it cannot describe the nuances of the complicated heat transfer mechanism occurring in all dimensions. The 1-D model of the textbooks usually neglects the conduction heat transfer through the interlayer and solid walls and simplifies the multidimensional convection heat transfer in the fluid to a 1-D term. This approach can be more general when the heat conduction in the interlayer is considered. Applying this approach, Aminuddin et al. [79] developed an analytical solution for a counter-flow heat exchanger subject to a uniform external heat flux and considering a 1-D axial conduction in the interlayer. Similar approach is utilized here to deal with the problem when the 1-D conduction heat transfer is considered in the two solid walls surrounding the two counter-flow channels in addition to the interlayer wall.

5.2.1 1-D Analytical Model

Consider two parallel channels of dimensions R and t , representing the length and depth of the channels, respectively. The top and bottom walls have identical thickness of t_w and thickness of the interlayer material is denoted by t_{int} .

The axial conduction in the two walls and the interface is considered while it is neglected in the flow. Suppose that the external walls are subject to uniform air convection with the coefficient h_∞ . Additionally, the flow has reached a fully developed

condition in both directions. A linear thermal gradient along the length of the chip generates a constant heat flux boundary condition to the channel wall. For this condition and depending on the aspect ratio of the channel, Nu can be estimated. Therefore, heat transfer coefficient between the fluid and wall is:

$$h_f = \frac{Nu \cdot k_f}{D_h} \quad \text{Eq. 5-1}$$

where k_f is the fluid thermal conductivity and D_h is the hydraulic diameter of the channel:

$$D_h = \frac{4A}{P} = \frac{2wt_c}{w + t_c} \quad \text{Eq. 5-2}$$

Also, in accordance with the microfluidic chip designed and fabricated in this study, in the counter-flow it is assumed that instead of two independent inlets and outlets, the outlet of one stream is the inlet of the next stream, as it is shown in **Figure 5-2**. As a result, it is fair to assume that the temperature of the first flow at its end equals the inlet temperature of the second one.

Schematic of the configuration for the 1-D model is drawn in **Figure 5-2**:

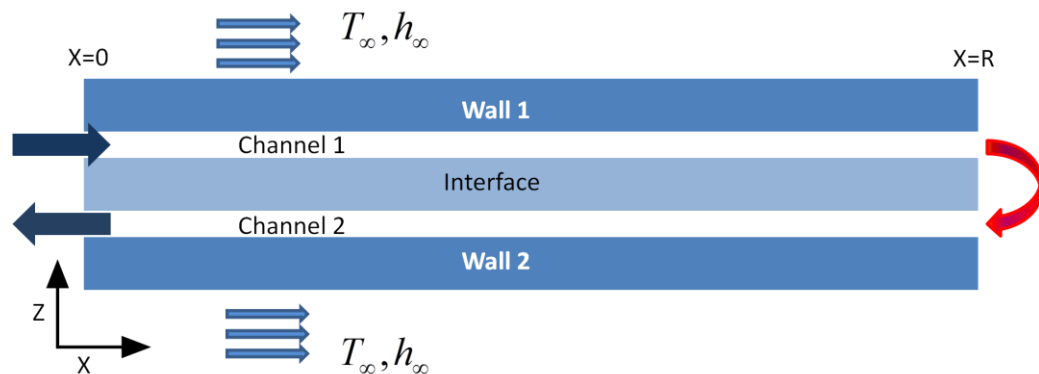


Figure 5-2: Schematic of the 1-D model

The governing equations and the corresponding boundary conditions are:

$$\frac{d^2 T_{w1}}{dx^2} = \frac{h_{ch1}}{k_{w1} t_{w1}} (T_{w1} - T_{ch1}) + \frac{h_{\infty}}{k_{w1} t_{w1}} (T_{w1} - T_{\infty}) \quad \text{Eq. 5-3}$$

$$\frac{dT_{ch1}}{dx} = \frac{h_{ch1}}{\rho \bar{V}_1 t_{ch1} C_p} (T_{w1} + T_{int} - 2T_{ch1}) \quad \text{Eq. 5-4}$$

$$\frac{d^2 T_{int}}{dx^2} = \frac{h_{ch1}}{k_{int} t_{int}} (T_{int} - T_{ch1}) + \frac{h_{ch2}}{k_{int} t_{int}} (T_{int} - T_{ch2}) \quad \text{Eq. 5-5}$$

$$\frac{dT_{ch2}}{dx} = \frac{h_{ch2}}{\rho \bar{V}_2 t_{ch2} C_p} (2T_{ch2} - T_{w2} - T_{int}) \quad \text{Eq. 5-6}$$

$$\frac{d^2 T_{w2}}{dx^2} = \frac{h_{ch2}}{k_{w2} t_{w2}} (T_{w2} - T_{ch2}) + \frac{h_{\infty}}{k_{w2} t_{w2}} (T_{w2} - T_{\infty}) \quad \text{Eq. 5-7}$$

where T_{w1} , T_{ch1} , T_{int} , T_{ch2} , and T_{w2} are temperature of the first wall, fluid in the first channel, interlayer, fluid in the second channel, and second wall, respectively. Parameter k represents the thermal conductivity of layers and channels, \bar{V}_1 and \bar{V}_2 are the mean velocities in the first and second channels, C_p and ρ are the specific heat capacity of the working fluid and its density, respectively. Convection coefficients of the fluid in the first and second channel, h_{ch1} and h_{ch2} , are calculated using **Eq. 6-1**. The ambient air temperature and convection coefficient are denoted by T_{∞} and h_{∞} , respectively. For the purpose of clarifying the effect of counter-flow, it is useful to consider the direct-flow case as well. The governing system of ODE's for the direct-flow is:

$$\frac{d^2 T_{w1}}{dx^2} = \frac{h_{ch}}{k_{w1} t_{w1}} (T_{w1} - T_{ch}) + \frac{h_{\infty}}{k_{w1} t_{w1}} (T_{w1} - T_{\infty}) \quad \text{Eq. 5-8}$$

$$\frac{dT_{ch}}{dx} = \frac{h_{ch}}{\rho \bar{V} t_{ch} C_p} (T_{w1} + T_{w2} - 2T_{ch1}) \quad \text{Eq. 5-9}$$

$$\frac{d^2 T_{w2}}{dx^2} = \frac{h_{ch}}{k_{w2} t_{eq}} (T_{w2} - T_{ch}) + \frac{h_{\infty}}{k_{w2} t_{eq}} (T_{w2} - T_{\infty}) \quad \text{Eq. 5-10}$$

The material properties used in the direct-flow case are the same as the counter-flow.

Since the second channel is removed from the calculations, the interface and second wall can be merged into one wall with the thermal properties of the second wall used in the counter-flow case and an equivalent thickness which is calculated in this way:

$$t_{eq} = k_{w2} \left(\frac{t_{int}}{k_{int}} + \frac{t_{w2}}{k_{w2}} \right) \quad \text{Eq. 5-11}$$

5.2.1.1 Boundary conditions

Thermal gradient along the chip can be applied by either constant T or constant Q to the top and bottom of the chip.

For the constant T boundary condition, based on how the heaters are attached to the chip, different conditions can be considered. If the heaters generate a uniform temperature at the two ends:

$$T_{w1}, T_{w2}, T_{int} = T_{cold} \quad \text{at} \quad x = 0 \quad \text{Eq. 5-12}$$

$$T_{w1}, T_{w2}, T_{int} = T_{hot} \quad \text{at} \quad x = R \quad \text{Eq. 5-13}$$

$$T_{ch1} = T_{in} \quad \text{at} \quad x = 0 \quad \text{Eq. 5-14}$$

$$T_{ch2} = T_{ch1} \quad \text{at} \quad x = R \quad \text{Eq. 5-15}$$

In case the heaters are attached to one side of the chip (which was the main configuration used in this research), it can be assumed that conduction through the depth of the chip defines the temperature of the layers at each end of the chip:

$$T_{w1} = T_{cold,w1}, T_{w2} = T_{cold,w2}, T_{int} = T_{cold,int} \quad \text{at} \quad x = 0 \quad \text{Eq. 5-16}$$

$$T_{w1} = T_{hot,w1}, T_{w2} = T_{hot,w2}, T_{int} = T_{hot,int} \quad \text{at} \quad x = R \quad \text{Eq. 5-17}$$

By knowing the heater temperatures at one side and using a 1-D heat conduction model in the depth of the chip, the remaining temperatures can be calculated. Schematic of the boundary condition applied by conduction is shown in **Figure 5-3**:

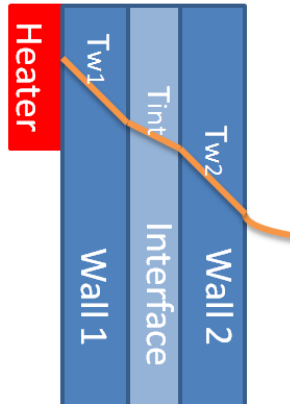


Figure 5-3: Temperature of each layer is dictated by the 1-D conduction when the heater is attached to one end

For the constant Q case, the boundary condition applied to the heating end will be:

$$\frac{dT_w}{dx} = -\frac{Q''}{k_w} \quad \text{at} \quad x = R \quad \text{Eq. 5-18}$$

where Q'' is the surface heat flux from the heater attached to the chip. Similar to the constant T boundary condition, different conditions can be applied based on where the heaters are attached.

This system of boundary value ODE can be solved analytically; however, reaching a closed form solution for it is tedious. Instead, the system of ODE was solved numerically using MATLAB boundary value ODE solver, BVP4ODE. The code is included in

Appendix A.

5.2.1.2 Results and discussions

It was noticed that the analytical solution is very sensitive to Nu . Therefore, for a better comparison, $Nu \approx 5$ was calculated from the 2-D simulation of an almost identical geometry.

$$T_{w1} = 303 \quad T_{int} = 304, \quad T_{w2} = 305 \text{ K} \quad \text{at} \quad x = 0 \quad \text{Eq. 5-19}$$

$$k_{w1} \frac{dT_{w1}}{dx} = k_{w2} \frac{dT_{w2}}{dx} = k_{int} \frac{dT_{int}}{dx} = -Q'' \quad \text{at } x = 40 \text{ mm} \quad \text{Eq. 5-20}$$

where Q'' is 6.5, 12, and 55 kW/m² for glass/glass, glass/quartz, and glass/silicon chips, respectively. Ambient air convection coefficient was considered to be 20 W/m²·K. Thermal conductivity of 1.38, 10, and 150 W/m·K was considered for the interface material representing the glass, quartz, and silicon.

The results from analytical method and CFD model are in very good agreement when the thermal conductivity of the interface material is high (quartz and silicon), while they are different when the interface material is glass. The difference increases noticeably for the glass/glass chip at high flow rates. As an example, the results of the analytical solution and the CFD model were plotted in **Figure 5-4**. Since the linear thermal distribution between the two ends of the chip is a very intuitive outcome, for the inlet of the channel, temperature was selected to be different from the temperature of the solids at $x=0$. As a result, a sharp change in the temperature of the fluid is observed in the results of the models (**Figures 5-4, 5-5, and 5-6**)

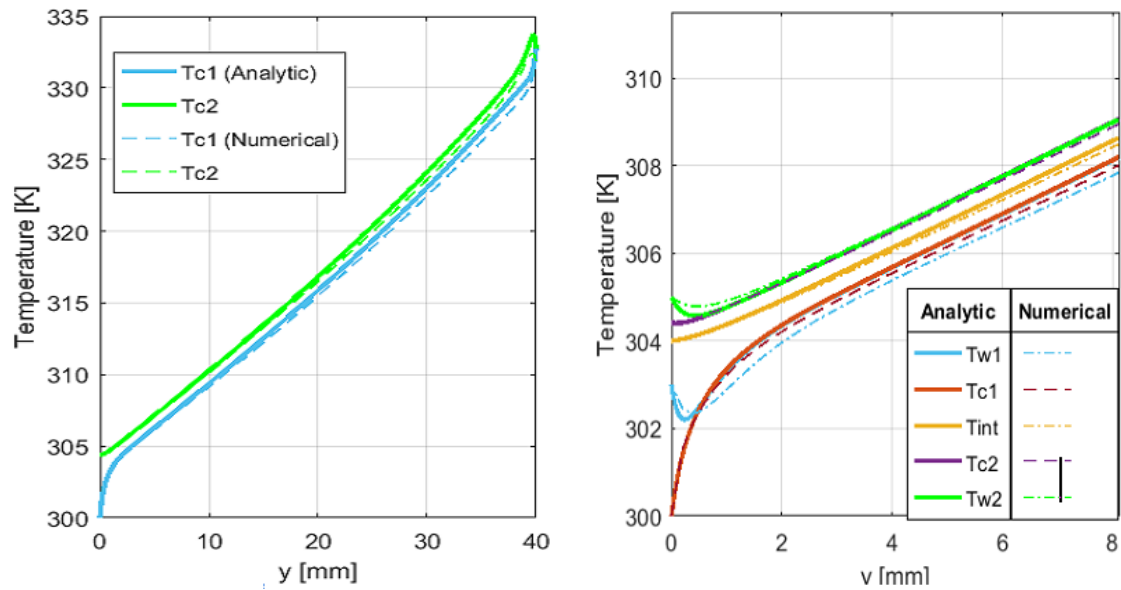


Figure 5-4: Thermal distribution in the glass/silicon counter-flow model at 10ml/hr from analytical and simulation plotted for different layers (wall 1, channel 1, interface, channel 2, wall 2). The right picture is magnified.

The reason can be explained by the assumptions on which the analytical solution was based. In the governing equations, axial conduction was considered while the conduction in y -direction was neglected due to the 1-D nature of the solution. This can be a reasonable simplification for high thermal conductivity materials as the thermal resistance in the thin width of the material is very small and therefore, uniform temperature in y -direction can be expected. For glass though, the uniform distribution in y -direction is not acceptable due to its poor thermal conductivity. The same justification is valid for the difference between the results of the two models at high flow rates. When the mean velocity is high, the parabolic temperature (solution of Poiseuille flow) in the channel width deviates from the uniform temperature assumed in the analytical solution.

Despite the comparative simplicity of the analytical solution, it explains a lot about how the counter-flow configuration assists in neutralizing the adverse convection effect of the ambient and consequently linearizing the gradient.

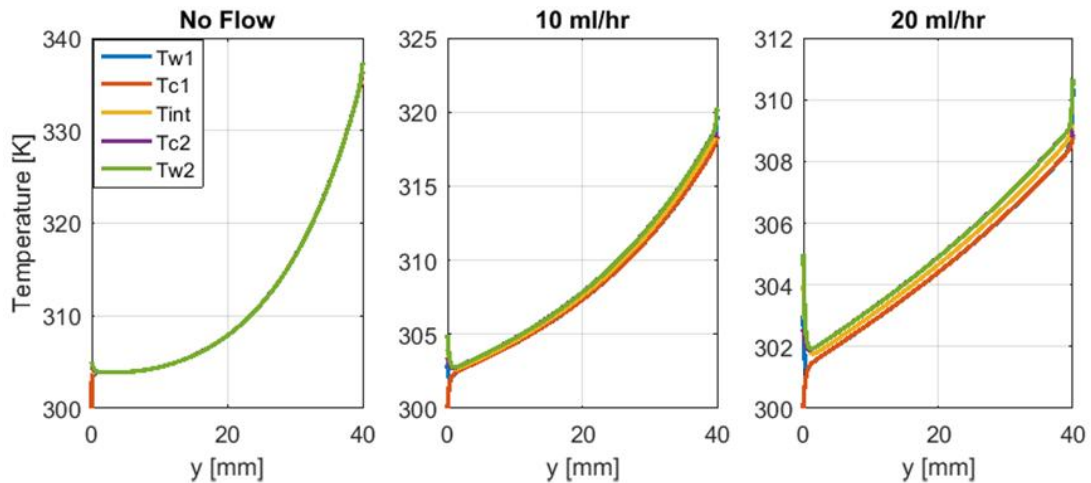


Figure 5-5: Thermal distribution of the layers along a glass/quartz counter-flow under no flow, flow of 10 ml/hr, and 20 ml/hr

As can be seen, the hyperbolic thermal distribution of the chip gets more linear as the flow increases. This is visible especially in the glass/quartz chip since the moderate thermal conductivity of the materials dictates the parabolic thermal distribution caused by the ambient convection. For the glass/silicon chip, due to the very high thermal conductivity, even at no flow condition, the thermal distribution is almost linear, as can be seen in **Figure 5-6**.

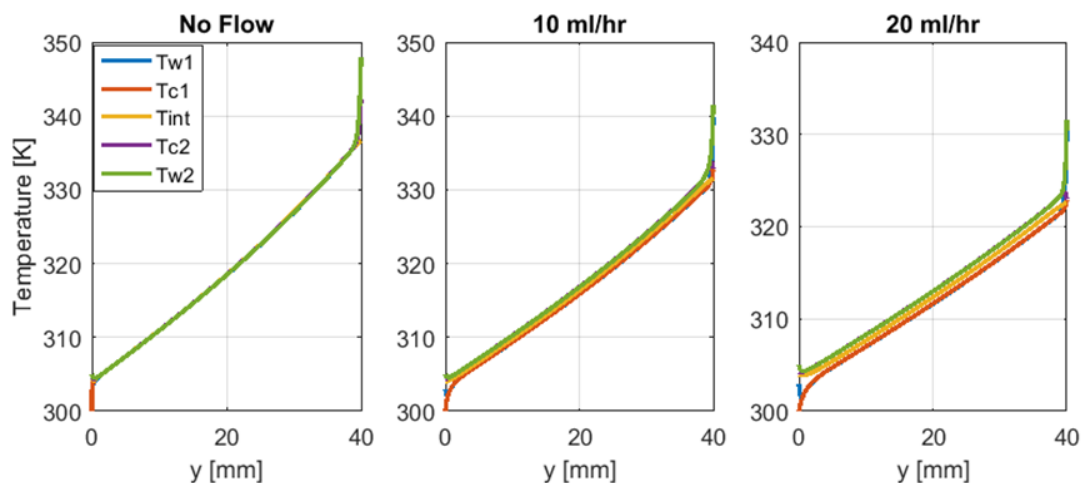


Figure 5-6: Thermal distribution of the layers along a glass/silicon counter-flow under no flow, flow at 10ml/hr and, 20ml/hr

The temperature change due to flow for the glass/silicon chip is less than the glass/quartz chip. This observation can be explained in this way: due to the constant Q boundary condition, fixed amount of heat is responsible for establishing a thermal gradient of interest at the end of the chip when there is no flow. The flow introduces a thermal mass which drags energy, and therefore, the temperature of the chip decreases under the flow. However, the heat flux Q required for establishing the same thermal gradient in the glass/silicon case is much more than that of glass/quartz chip (about 4.5 times more), and therefore, for the same flow rate, it is more resistant to the flow condition.

5.3 Design and Fabrication of a Counter-flow Chip

The concept of a counter-flow chip for thermal stabilizing was covered in the previous chapters. In this chapter, microfabrication procedure of a hybrid silicon/glass counter-flow microfluidic chip including the design of the chip, design of the photomask, formation of the hard mask using photolithography, wet etching, device

packaging, and assembling the set up will be described. Fabrication using xurography for hybrid glass/glass and glass/quartz chips will be discussed briefly because details of this fabrication technique can be found in the reference [77].

5.3.1 Design

5.3.1.1 Chip Design

Analytical solution of chapter 3 for a chip under the thermal gradient was used for minimizing the impact of the parabolic temperature distribution, which can be a source of temperature difference when the two sensing and reference junctions of the thermoelectric are not placed symmetrically. To analyze it, for a fixed height and thickness of a glass chip, temperature difference at 1 mm and 2 mm off the centerline was calculated for different widths. Convection coefficient of the air is assumed to be the typical value of $20 \text{ W/m}^2\text{K}$. When there is no convection, this value is ideally zero for all the widths, so for chips fabricated with a higher conductive material in which the conduction dominates the convection, this error is much smaller.

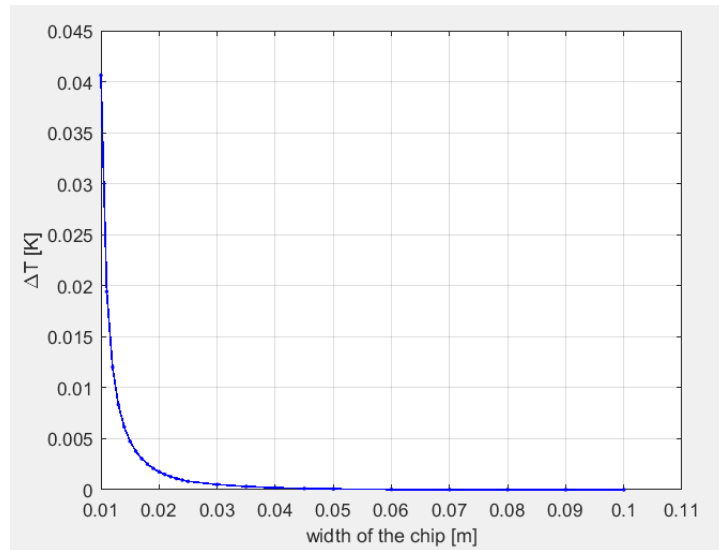


Figure 5-7: Impact of the width on the temperature difference between two fixed points

5.3.1.2 Microchannel Design

The microchannel design is based on the thermopile application in a way that one set of junctions aligns with one stream without any internal heat event (e.g. a buffer solution) called reference junction and the other set of junctions aligns with the stream containing the heat event of interest (e.g. melt of DNA) called the measuring junctions.

The counter-flow chip is designed for the minimum number of inlets and outlets for the simplicity of the set up. At the same time, the aim of the device dictates the minimum of two inlets. The schematic of two preliminary designs for this application is plotted in **Figure 5-8**:

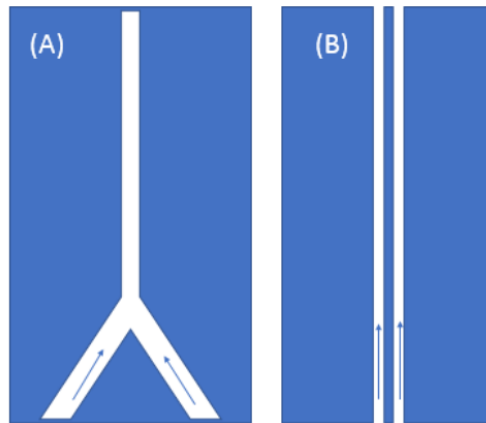


Figure 5-8: Schematic of two microfluidic designs for the thermoelectric sensing a) merging b) parallel

The merging pattern or the Y-channel is the design used in the thermoelectric microfluidic sensor explained in chapter 3. Such a configuration has been widely used in the microfluidics, taking advantage of the side-by-side laminar flow. Fully developed flow can be achieved in both sides if the interface thickness is negligible. This condition occurs when the mass Péclet number is large. For a certain thermopile sensor (e.g. thermopile introduced in chapter 3), minimum width of the channel needs to be equal or larger than the distance between the junctions. The parallel channel pattern in contrast, avoids the mixing of the two streams and allows much smaller channel widths as long as their width is larger than the thermopile junctions. The distance between the channels is limited by the width of the thermopile. In both designs, a minimum of two inlets and outlets are required. Also, in both designs the common mode rejection characteristic of the thermoelectric sensor helps reduce the artifacts. In comparison, the parallel pattern avoids any potential unwanted artifacts due to the mixing of the two streams especially at low mass Péclet numbers when the interface width expands to the channel walls. Furthermore, the discussion made in the chapter 4 showed how establishing a full

similarity between the two side-by-side flows can be cumbersome or even impossible when there is a mismatch between the Prandtl number of the two fluids. Although most of the biological samples (e.g. DNA solution) are water based and probably have similar thermal properties, their viscosity can be significantly different.

To take advantage of both designs, the final design is the combination:



Figure 5-9: a) Front side of the chip b) Back side of the chip

Front and back will be connected through a hole drilled at the end of the channel. For demonstrating the performance of the counter-flow chip, a direct-flow chip will be fabricated without drilling the hole between the front and back channel.

Beside the distance of the two parallel channels and the location of the inlets and outlets which are constrained and customized for the existing thermal sensor and the chip holder, there is still room for alteration and modification for the remaining dimensions. For example, the 1 mm channel width was selected to make the microfabricated device comparable with the xurography fabricated devices. Since xurography required more manual labor and involved the scoring of adhesive films, thinner channels increase the uncertainty, especially for the alignment of the features cut in tape on the back and front side of the chip while for the microfabrication technique, it is not the case. The obvious advantage of the thinner channel design is the higher thermal ramp rate. Also, the low

aspect ratio of the channel enhances the mixing of the two streams at the junctions. The noticeably long distance between the merging point of the two channels and the end of the channel located on top of the chip may give rise to the asymmetry of the design, which is not favorable. However, this design increases the mixing length of the two streams.

5.3.1.3 Photomask

According to **Figure 5-9**, the chip has two different patterns on back and front sides making a two-layer device. In photolithography, usually each layer with a different pattern requires a separate photomask. Fabrication of a precise and high quality photomask requires time, and it is often costly. As a result, reducing the number of the masks helps reduce the complexity, the expenses, and the time of the process. Here, instead of two photomasks, a single photomask containing both patterns was designed. Accordingly, alignment mark sets were designed in a complementary way. In the succeeding fabrication steps, when the pattern is transferred from the photomask to the photoresist-coated front side of the chip using the standard photolithography steps, photomask was rotated 180° to transfer the complementary pattern to the photoresist-coated back side of the wafer.

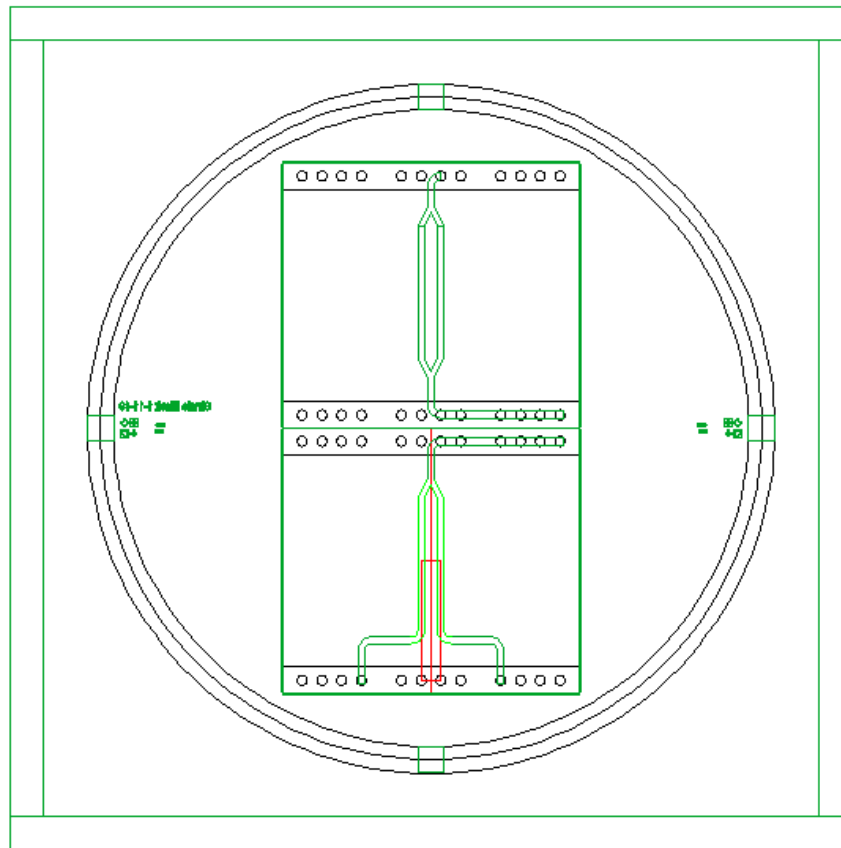


Figure 5-10: Photomask layout including the final pattern (plotted in green color) and the guidelines

The photomask was designed for a 4" wafer containing two devices. Guidelines used for locating the inlets, outlets, and the potential location of a 3 by 1 mm thermopile are drawn in the **Figure 5-10**. The array of inlets shows the location of holes in an aluminum chip holder (Dolomite Microfluidics, Royston, UK) which will be used in the device assembly.

Two sets of alignment marks were designed on the left and right edge of the wafer in order to minimize the error in x , y , and θ .

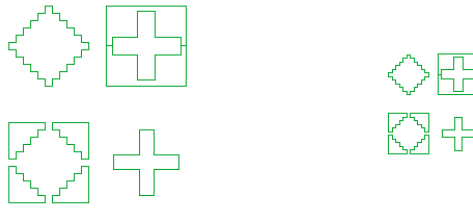


Figure 5-11: Alignment marks designed in a large and a small set

The photomask was designed in AutoCad and the DXF file format was converted to GDSII format suitable for the laser mask writer using the LinkCad software. The high resolution chrome/quartz mask was fabricated in the laser mask writer.

5.3.2 Hard Mask Fabrication

The standard photolithography process was used to create the hard mask suitable for the following wet etching step. Prime <100> p-type silicon wafers (Resistivity 1-20 Ohm.cm) of 100 mm diameter and thickness of 500 μm were used as the substrate for the chip. Since potassium hydroxide (KOH) was selected as the etchant solution in the wet etching process, an appropriate hard mask was required to protect the remainder of the wafer from being etched. Common hard masks used in the KOH etching of silicon are silicon dioxide (SiO_2), silicon nitride (Si_3N_4), and alkali resistant metals such as chromium. Most of other metal masks are not suitable in KOH wet etching since the poor adhesion to the wafer allows the etchant to creep between the metal film and the wafer, causing it to peel off. On the other hand, most of the photoresists cannot withstand the KOH. The ratio between the etch rate of silicon to the hard mask, or the "selectivity" of oxide, is around 100. This value is around 1000 for the nitride. Considering the depth of the channel (less than 100 μm) and the availability of the equipment, silicon dioxide was chosen as the hard mask. Silicon dioxide can be formed using dry or wet oxidation or it

can be deposited using chemical vapor deposition (CVD). Growing silicon dioxide using wet oxidation is significantly faster compared to dry oxidation as the water vapor diffuses much faster into the formed silicon dioxide. However, the slow dry oxidation process leads to a denser oxide layer of higher quality [80]. About 800 nm of oxide were thermally grown on both sides of the wafers in a quartz tubular furnace at 1200 °C.

5.3.3 Photolithography

Unlike the dry etching (the etch process is directional), the wet etch process enables the simultaneous etching on both sides of the wafer. As a result, the standard photolithography steps are done on both sides of the wafer before creating any etched feature in the silicon or silicon dioxide. The steps for transferring the pattern to both sides are:

1. Wafer cleaning using IPA and acetone
2. Drying the wafer on the hot plate, 2 minutes at 110° C
3. Applying the positive S1813 photoresist and spin coating
4. Soft baking for 1-1.5 minutes at 95° C on hot plate
5. Mounting the wafer in MA/BA6 Mask Aligner (Suss MicroTec, Germany), aligning the wafer edges with the four square windows of the photomask
6. Exposure (14 to 25 seconds)
7. Developing in MF 319 and rinsing in DI water, (no need to agitate it since it enlarges the etched feature, also no need to rinse it with a strong water flow)
8. Hard baking at 125° C for 5 minutes on hot plate
9. Gently centering the wafer on the spin coater and spin coating on the back of the wafer

10. Soft baking in an oven or on a hot plate, five minutes at 110° C (or on the hotplate at 95° C for 1-1.5 minutes)
11. Putting the wafer in MA/BA6
12. Rotating the mask by 180° to flip the top and down and putting it in the MA/BA6 mask holder
13. Aligning with respect to the alignment marks, and UV exposure
14. Developing in the MF 319, rinsing in DI water
15. Hard baking for 5 minutes on hot plate at 95°

Longer hard baking at the end is especially important when the photoresist is used in harsh chemicals such as hydrofluoric acid (HF) or buffered oxide etch (BOE) for a comparatively long time, which is required for removing the thick silicon dioxide layer. The through hole connecting the front and back side channels can be drilled after defining the features by photolithography, after generating the features in the hard mask, or after the wet etching. If the precise dimension of the hole is important, it should be noted that the hole expands during the wet etching. Here, drilling the hole was done successfully either before or after the wet etching. However, drilling the hole after the wet etching makes the process much simpler and maintains the original dimension of the hole. For thin wafers or for very deep etched channels, chances are that making the holes using mechanical techniques such as drilling with diamond beads causes extra stress and breaks the wafer. In such conditions, it is better to drill the hole before or to use other techniques such as laser drilling [81], or etch-through-hole techniques such as DRIE [82, 83]. Hard mask fabrication step is usually finalized by wet etching of the unprotected SiO₂ in BOE or in HF. BOE 7:1 was used to etch the oxide at room temperature. Observing the change

in the color of the wafer from bluish to gray is a visual way for stopping the etch. Considering the typical etch rate of $700 \text{ \AA}/\text{min}$, the 800 nm oxides were etched in about 12 minutes. A better way for assuring the removal of all oxide is to rinse it in DI water. If a layer of oxide still remains on the surface, the water wets it, while if it is removed completely, only water droplets remain on the surface due to the silicon hydrophobic property. Native oxide always forms on the wafer, therefore performing the wet etch right after this process is very beneficial for achieving a uniform surface. Once the oxide was removed, the photoresist was also rinsed off with acetone. An image of the wafer and hard mask is shown in **Figure 5-12**:

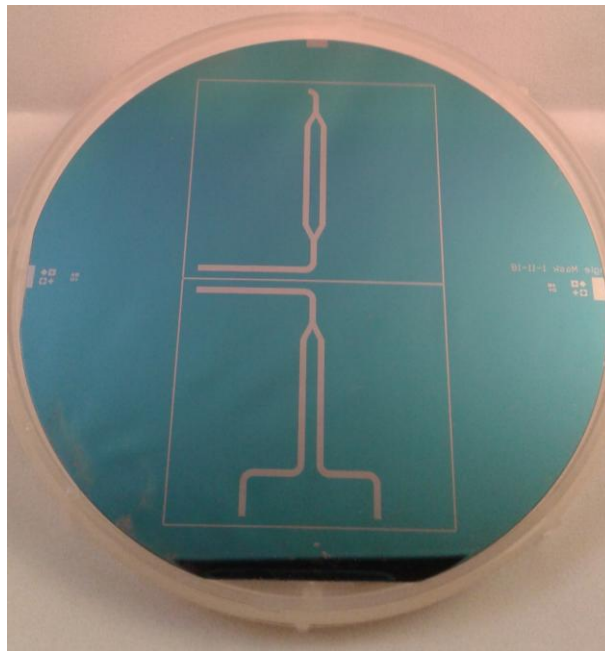


Figure 5-12: Wafer with the patterned oxide as the hard mask. The bluish color shows the oxide and the gray color represents the silicon

5.3.4 KOH Wet Etching

Carving a microchannel in a silicon wafer performed through the selective removing of a significant amount of a silicon wafer is an example of bulk

micromachining. Wet etching and dry etching are two main techniques in the bulk micromachining. Wet etching usually tends to be isotropic whereas highly anisotropic features can be etched through dry plasma etching [84]. However, based on the chemistry of the etchant, isotropic features from dry etching as well as highly anisotropic features by wet etching are feasible. In any etch method, the key parameters are the selectivity and the etch rate. In crystalline materials, such as silicon and quartz, certain crystal lattice orientations are etched much slower. For silicon, the etch rate of $\langle 100 \rangle$ and $\langle 110 \rangle$ planes are remarkably more than $\langle 111 \rangle$ crystal planes in the alkaline solutions such as KOH, TMAH, and EDP. This characteristic has been used for the manufacturing of V-grooves formed by the intersection of $\langle 111 \rangle$ planes in the $\langle 100 \rangle$ silicon wafers and for creating the vertical walls in the $\langle 110 \rangle$ silicon [80, 82]. Although $\langle 110 \rangle$ silicon is an ideal choice for creating the microchannels, $\langle 100 \rangle$ silicon has been widely used for microchannels due to its availability and lower price. Very smooth 57° sidewalls can be achieved simply by anisotropic wet etching. Despite the CMOS incompatibility and the relatively poor selectivity to SiO_2 hard mask, KOH has the best etch rate and the highest crystalline plane selectivity, making it an ideal etchant for MEMS applications, such as microchannel fabrication [82]. Etch rate and surface roughness of silicon is a strong function of KOH concentration, temperature, and agitation [85]. Adding IPA or special surfactants can be an effective way to reduce the roughness of the etched surfaces [86]. Adding IPA also helps keep the composition of the solution as IPA stays on top due to its lower specific gravity. In better words, IPA acts as a sacrificial liquid layer for water/KOH solution.

5.3.4.1 Wet etching set-up

The set up used for wet etching consists of a 5 liter Pyrex beaker, a condensation lid, hot plate with magnetic stirrer, stirrer bar, and HDPa wafer cassette. About 3.5 liters of 32 to 35% KOH solution was prepared by diluting the aqueous 45% (w/w) KOH (700000776-VWR –PA-USA) with DI water. 0.3 to 0.5 liters of IPA was added to the solution after heating the beaker to the approximate temperature of 75 °C. <100> silicon wafers (100 mm diameter, Boron doped, 10-20 Ohm.cm, 500 µm thick) were selected for the microchannel substrate.

Due to the large thermal mass of the solution, it takes a really long time to reach the set temperature of 70 °C. Therefore, a 500 watt immersion heater was used along with the insulator foams covering the outside surface of the beaker when the mixture was heating up on the hot plate. Once the temperature reached the set temperature, the immersion heater was taken off, the wafer cassette containing the wafers was transferred to the beaker, and the condensation lid was put on the beaker. Wafers were placed vertically to facilitate the discharge of the byproducts such as hydrogen bubbles, which are known to cause pseudo-masking [85]. **Figure 5-13** shows the picture of the set up.



Figure 5-13: KOH wet etching set up

Two sets of wafers were etched under different conditions. In the first set, a half liter of IPA was added to the 35% KOH solution without agitation. In the second set, 0.3 liters of IPA was added to the 32% KOH, and a magnetic stirrer bar was used for agitation at 250 to 300 rpm.

5.3.4.2 Outcome

Surface roughness and depth of the channels were analyzed in the 3-D microscope (Keyence VK-X150) and Dektak 150 Surface Profiler. In the first set of

wafers, the etched surface had non-uniformities in terms of depth and roughness. Etch depth of 55 to 70 μm was observed in a single wafer. The overall smoothness was good, but regions with high roughness existed.

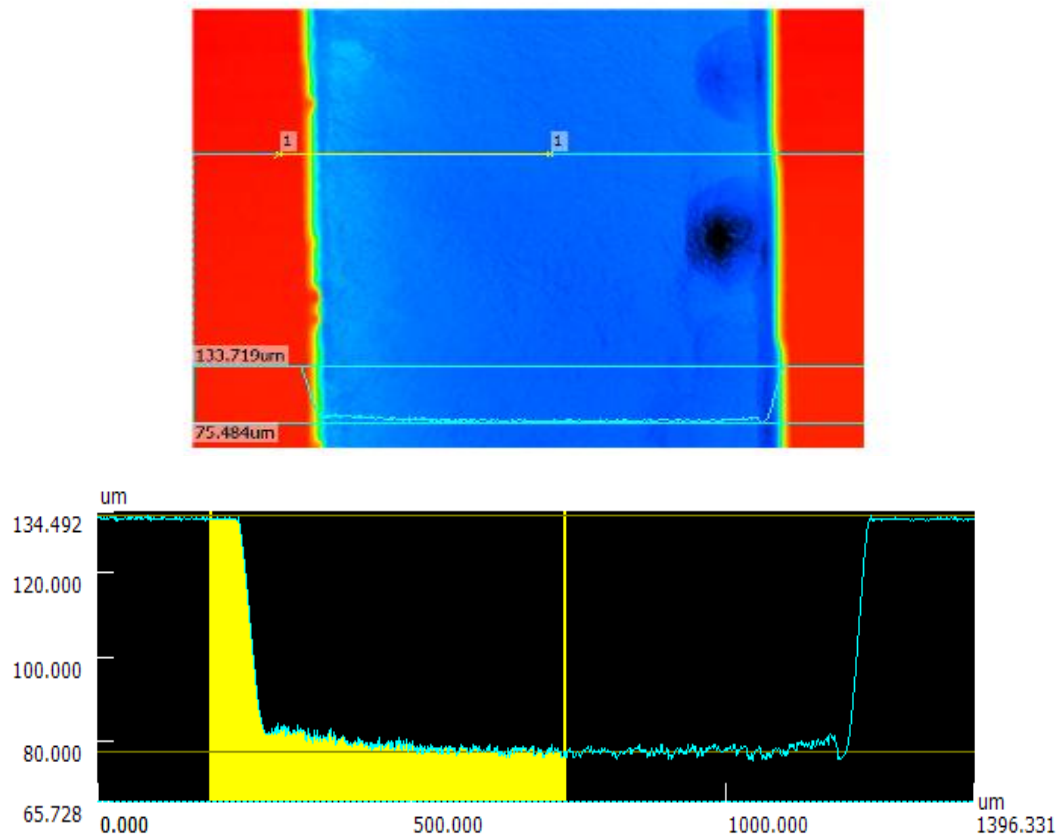


Figure 5-14: A 3-D microscope image of the etched channel on front the side of the wafer. Top picture shows the top view of the etched channel (maximum height demonstrated by red color, minimum by dark blue). The bottom picture shows the profile of the etched channel probed along line 1 shown in the top picture. The difference between the highest and the lowest depth is about 68 μm .

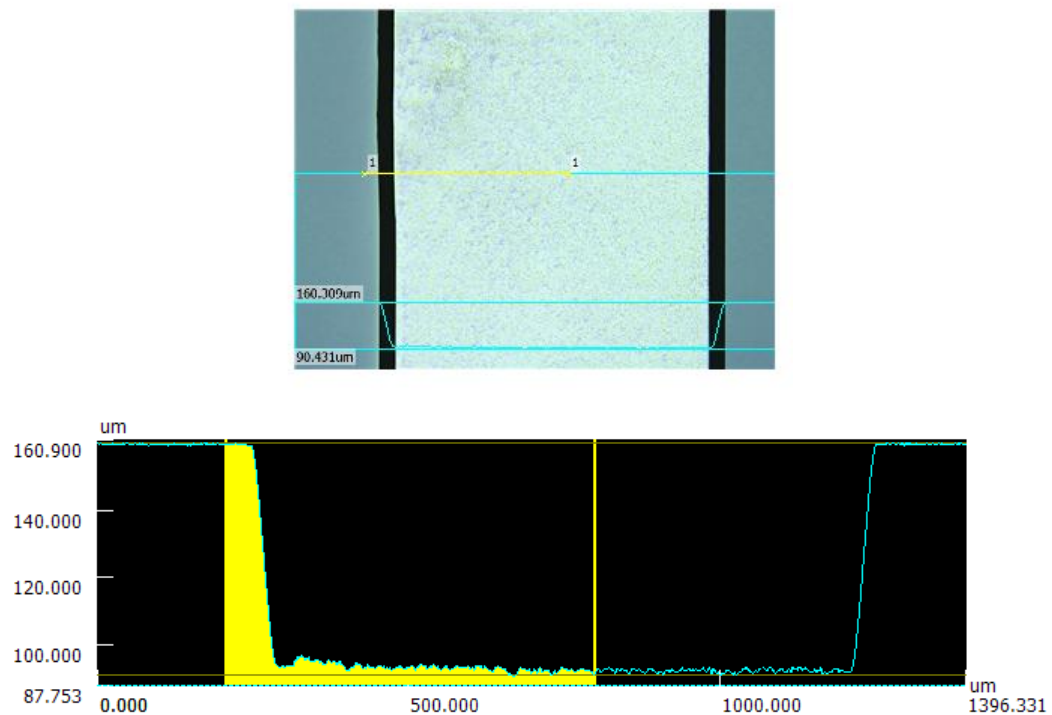


Figure 5-15: 3-D microscope image of the etched channel on the back side of the wafer. The two parallel thick black lines in the top picture show the anisotropic walls of the etched channel. The roughness of the etched surface of the channel can be seen in the top view. The profile of the probed line 1 is shown in the bottom picture. The etch depth is about 55 μm .

The etched surface of the second set was rougher, but the uniformity of the etch depth was significantly better possibly due to agitation. For the counter-flow application, the uniformity in the depth of the channel, especially on both sides of the wafer, is a critical characteristic for the performance of the device since it influences the local velocity of the fluid. As a result, wet etching with the second set of parameters is recommended despite the higher roughness of the outcome. Of course, reducing the surface roughness is a very important practice in microchannel fabrication especially in the heat sink application for the purpose of reducing pressure loss [87]. For the biomedical application of this device, the high surface roughness may have a detrimental

effect, such as trapping large biomolecules like DNA; however, optimizing the surface quality of the microchannel is a time consuming process and is beyond the focus of this study.

5.3.4.3 Residual hard mask removal

The original thermally grown SiO₂ layer in the dry oxidation furnace was not uniform. As a result, when the etch process was stopped, there were regions with oxide residue (hydrophobic/hydrophilic surface was checked by DI water to check the remaining oxide). The remaining oxide measured in Filmetrics was between 80 to 200 nm. For the following device bonding step, it is important to have a clean and uniform surface. Therefore, the wafers were underwent an additional BOE etch to remove the residual oxide.

5.3.5 Chip Assembly

Chip assembly or chip packaging is the process of closing the open microchannel and attaching the inlet and outlet ports. Once the features are generated in the wafer, the device should be capped. For a biomedical application, capping the channels using a transparent material is extremely useful as it allows the optical monitoring techniques such as Fluorescence spectroscopy or direct optical monitoring of the process when a dye is used. Glass, quartz, PDMS, polycarbonate, SU-8, and PMMA are the popular candidates. In the choice of capping material, in addition to the optical transparency, mechanical and thermal properties as well as the biocompatibility characteristics are of great importance. The low thermal conductivity of the capping material allows producing a large thermal gradient at a lower power. In this sense, polymers are a better choice. On the other hand, using a hard material with similar mechanical properties is advantageous

over the soft and elastic polymers. In addition to the cost and availability, the feasibility of bonding techniques is probably the most important parameter in selecting the capping material. As far as the simplicity of the bonding, the direct plasma bonding of the PDMS to the native oxide on the silicon makes it an interesting option. However, its low stiffness is not favorable for integration with silicon. Moreover, in the thermal characterization using IR thermography, the big gap between the thermal conductivity of PDMS and silicon makes a significant difference between the actual temperature of the channel and the IR camera read outs from the PDMS surface. The huge difference between the coefficient of thermal expansion (CTE) of silicon and PDMS (several orders of magnitude [88]) can apply a significant thermal stress to the silicon chip when it is used under a large thermal gradient. Therefore, the sandwiching material should have low thermal conductivity compared to silicon but be compatible in other thermal and mechanical properties. This suggests the selection of glass or quartz for this application.

Material properties of some common materials for fabrication of microfluidics are summarized in **Table 5-1**:

Table 5-1: Material properties of common candidates for microfluidic fabrication

Material name	Thermal conductivity (W/m²K)	CTE (10⁻⁶/K)	Young modulus (GPa)	Refractive index
Silicon	148	2.5	140-180	Opaque
Glass (Pyrex)	1.1	4	67	1.473
ST-cut quartz	7-10	7.1-13.2	76.5-97.2	1.54
PDMS	.15	960	less than .001	1.43
SU-8	.2	52	2	1.59
Polyimide(Kapton®)	.46	20	2.5	1.7

5.3.5.1 Bonding techniques

Wafer bonding techniques are usually classified into "direct" and "indirect" methods. In the direct method, two materials are bonded without any intermediate material. Fusion bonding and anodic bonding are probably the most well-known direct bonding techniques. Direct bonding requires a very clean wafer with special attention to the particulates. Fusion bonding of the glass to glass at 650° C and plasma activated bonding of glass to glass are two examples of direct bonding of glass [83].

Anodic bonding is probably the best bonding method for fabricating hybrid glass/silicon devices. Only glasses containing the alkaline impurities and with a CTE close to the CTE of silicon such as Corning 7740 (Pyrex), Borofloat glass, Schott 8329, and Corning 7070 are anodic bondable [83, 89]. Glass and silicon heated to 300-450° C bond together in an electrochemical process when the mobile alkali ions of glass under an electrical potential move towards the cathode and leave an oxygen rich "depleted region", causing the oxidation of the silicon at the interface of the two wafers [89].

Anodic bonding of triple stack of glass/silicon/glass structures, which is applicable for the fabrication of counter-flow device, is also possible. In comparison to glass/silicon bonding, it is less straightforward and requires creative steps which have been developed by different researchers [90, 91]. Both fusion and anodic bonding are usually performed under the vacuum condition and require specific equipment.

In indirect bonding, the two wafers bond together using an "intermediate" layer in between [92]. Unlike the direct bonding technique, indirect bonding is usually less expensive, requires lower applied temperature, does not require an extensive cleaning procedure, is less sensitive to the surface defects and scratches, and can be performed without expensive or special equipment. A wide variety of intermediate layer materials such as metals, solder, glass frit, and polymers were reviewed and compared in the reference [92]. Uniform spreading of the adhesive on the bonding surfaces is the crucial part of the indirect wafer bonding. Photoresist polymers exist in a variety of viscosities and can be dispensed uniformly using spin coaters and be patterned using cleanroom equipment.

SU-8, the negative epoxy-based photoresist is one of the most ubiquitous polymers used in microfluidics. Its excellent mechanical strength, along with its good thermal and chemical stability, have expanded the usage of this polymer from a regular photoresist to a material for direct fabrication of high aspect ratio structures in microfluidics, and as a mold in soft lithography. Since SU-8 bonds easily to itself, it can be used for creating microstructures that can be simply packaged by the same material [93]. Moreover, its optical transparency makes it a material of choice when it is used for bonding glass to glass.

5.3.5.2 Wafer dicing

When direct bonding techniques such as fusion and anodic bonding are used, depending on the equipment, it is often necessary to bond the wafer before the dicing step. In contrast, for the indirect bonding using adhesives, dicing the wafer into chips before the bonding process has advantages, such as less consumption of adhesives, which are often expensive (e.g. SU-8), and easier handling. Therefore, the wafer dicing is performed before the bonding.

Silicon wafers were diced with a wafer dicing saw (MicroAutomation, CA, USA) using a nickel blade. The guidelines showing the border of each chip in the photomask (**Figure 5-10**) were very helpful for simplifying a precise dicing. Subsequently, Pyrex glass wafers of 760 mm thickness and 10 mm diameter (University wafers, MA, USA) were diced to obtain two 40×45 mm rectangles in the same dicing saw using a diamond- and- epoxy resin blade. Needless to say, compared to silicon wafer, glass wafer dicing demands a significantly longer time because it is done by score cutting. For the xurography chips, ST-cut quarts were diced.

5.3.5.3 Chip bonding using SU-8

Despite the numerous examples of using SU-8 for bonding, the procedure is still very tricky and mostly depends on skill and experience. The worst problem associated with the SU-8 chip bonding for the microchannel is the channel clogging. SU-8 bonding should be done around the glass transition temperature of the SU-8 when it is less viscous. Consequently, any non-uniformity in the temperature and applied force may guide the low viscous resist to the etched channel. The sloped 57° sidewall of the microchannel caused by wet etching also aggravates this problem.

For wafer bonding, it is recommended to use a low viscous SU-8, such as SU8-5 [94, 95]. SU8-5 is suitable for thicknesses of 5 to 15 μm , depending on the spin speed. For avoiding a significant introduction of the SU-8 into the channel as well as maintaining the designated microchannel depth, a lower thickness is preferable. Moreover, SU-8 has a comparatively high CTE compared to silicon [93], so, having a thinner layer applies less thermal stress to the device.

In the first attempts, the protocol suggested by Yu et al. [95] was followed to imprint the SU8-5 (Microchem corp, MA, USA) only on the non-channel surface of the etched silicon. For the features with a high ratio of etched surface such as a pressure sensor cavity, direct imprinting of the SU-8 from a dummy wafer to the etched surface is a promising procedure. When the ratio of etched surfaces to the chip surface is low (as it is in the pattern used in this dissertation) the separation of the two wafers using a razor blade may break the brittle wafers. On the other hand, separating the wafers by sliding introduces SU-8 to the etched area. For such a condition, Lu et al used a Teflon roller for transferring the SU-8 from the dummy wafer to the etched wafer surface.

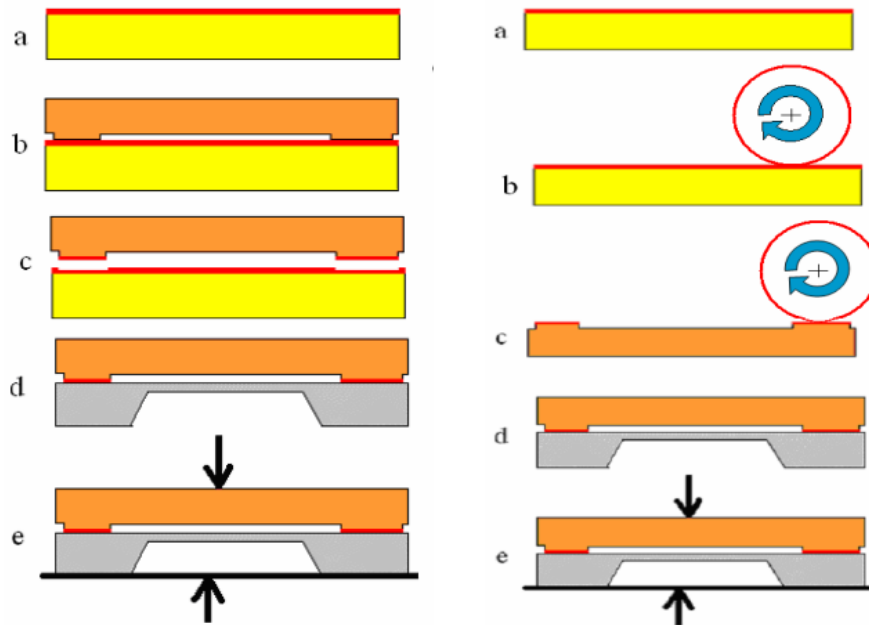


Figure 5-16: Schematic of the two contact imprinting methods for transferring SU-8 to an etched surface [95]

Unfortunately, transferring the SU-8 using the Teflon roller was not successful because the thin SU-8 layer wouldn't stick to the roller while the thick layer would lead to an uneven distribution of the resist on the surface of the roller. Consequently, SU-8 was spin-coated on the diced glass slides and brought in contact to the diced silicon chip. The recipe used here for the pre-treatment and bonding is based on what Lima et al [94] suggested. The steps are given below:

1. Wafer cleaning using NanoStrip® at 65 °C for 10 minutes followed by rinsing and drying
2. Dehydration on the hot plate at 120 °C for 30 minutes. Following these steps, not only are the contamination and particles minimized, but also the surface energy of the glass and silicon wafer will be reduced, which in turn improves the adhesion of SU-8.

3. Spin coating the SU-8 on a 45×40 cm glass slide: 5 seconds ramp of 500 rpm/sec, 30 seconds at 3000 rpm to form about 5 μm layer. Care should be done to center the slide as much as possible. For glass slides with holes, due to high viscosity of the SU-8, the holes stay intact.
4. Leaving the coated slide to "age" at room temperature for 10 minutes [93] while setting one hot plate to 65 °C and another one to 95 °C.
5. Soft baking at 65 °C for a minute. This step decreases the thermal stress, evaporates some solvent, and promotes the adhesion. The silicon wafer is also heated to the same temperature.
6. Very gently approaching the two parts together and aligning the holes in the glass to the inlet of channels in the silicon. No force should be applied in this step as it introduces a large quantity of photoresist into the channel.
7. Transferring the two slides over the 95 °C hot plate. The hot plate should be perfectly leveled. Any tilting may introduce SU-8 into the channel. SU-8 at 95 °C has much less viscosity, helping the bond spread. However, it is very probable that some parts will not be bonded completely. Applying a uniform or local weight (less than 200 g) helps the bond spread. The whole soft baking at 95 °C takes 5 to 10 minutes.
8. Once the two slides are taken off the hot plate and cooled down to the room temperature (it makes the SU-8 very viscous and minimizes any sliding) the assembled chip should be exposed from the glass side. A dose of 600 mJ cm⁻² recommended by Lima was used. The exposure was done in the MA/BA6 mask aligner. The exposure time can be calculated by dividing this dose by the mask

aligner power. By experience, at least two minutes of exposure is necessary to cure the SU-8. After the exposure, the crosslinked SU-8 turns gray.

9. Post exposure bake at 95 °C for a minute. The duration can be extended to up to five minutes to ensure a complete crosslinking.

The other side of the chip should be bonded similarly. However, the glass/silicon bonded slides cannot be immersed in the NanoStrip as it penetrates into the channel, reacts with the SU-8, and clogs the channel. Thus, surface cleaning was done using acetone and IPA.

It is possible to use a negative mask to selectively keep the SU-8 coated parts of the glass slides unexposed. Then, by flowing the SU-8 developer, one can remove the uncrosslinked photoresist on the channel wall. However, chances are the developer removes some of the uncrosslinked resist of the sidewalls. To avoid this, an interesting lift off process is suggested by Lima et al. for creating a negative aluminum mask that covers the sidewalls of the channel [94]. However, this step needs to be done at the end of the wet etching process and before removing the hard mask residue removal. Bonded chips were all tested later by flowing up to 30 ml/hr flow. The overall thermal resistance applied by the very thin photoresist layer is small despite the low thermal conductivity of the SU-8 due to its thickness.

5.3.5.4 Attachment of inlets and outlets

The location of the inlets and outlets was designed based on the CAD of an aluminum chip holder (Dolomite Microfluidics, Royston, UK). As long as the inlet holes in the chip are aligned and in contact with the holes in the chip holder holes, the device is leak free due to the gasket of the chip holder. However, as the holder was originally

designed for 4 mm thick microfluidic chips, there is a gap, which should be filled to make the device leak free. In the first set of experiments, this configuration was tested successfully. However, for thinner hybrid chips fabricated by xerography, tightening the gap caused cracks at the inlets. Therefore, PDMS ports replaced the inlet part of the chip holder in all of the proceeding experiments.

PDMS ports were bonded to the glass inlet and outlets using the oxygen plasma cleaner (Harrick Plasma, NY, USA). Tubings were inserted in the holes punched by 1.5 mm punch and plumber. Inlet tubings were connected to 10 ml plastic syringes fitted into the injection syringe pumps.

5.4 Thermal Gradient Experiment

Six sets of microfluidic chips were fabricated and used to analyze the impact of counter-flow and the interface material on the behavior of the thermal gradient chip. Hybrid glass/quartz and glass/glass counter-flow and direct-flow chips were fabricated using the xurography technique by cutting 100 μm polyimide tapes (PPTDE 1 112, Kaptontape.com, CA, USA). Pyrex glass wafers 500 μm thick and ST-cut quartz wafers (University Wafers, MA, USA) of 375 μm were diced in the wafer dicing saw to make two 40 \times 45 mm slides. The alignment of the back and front channels cut by a vinyl cutter (CE 5000-40-CRP, Graphtec, Yokohama, Japan) was done by hand. **Table 5-2** outlines the microfluidic chips used in this study in terms of interlayer material and thickness, channel depth, and fabrication technique:

Table 5-2: Summary of the three type of microfluidic chip fabricated and used in this study

Abbreviation*	Interlayer material	Interlayer thickness (μm)	Channel depth (μm)	Fabrication technique
GS	<100> Silicon	**	65	Microfabrication
GQ	Crystal Quartz	350	100	Xurography
GG	Pyrex Glass	500	100	Xurography

* Each chip is fabricated in direct-flow and counter-flow version generating a total of six chips abbreviated as GSCF, GSDF, GQCF, GQDF, GGCF, and GGDF.

** The thickness of the interlayer silicon is not uniform: 500 μm where it was not etched and 370 μm between the counter-flow channels

5.4.1 Experimental Set Up and Procedure

Thermal gradient was generated by attaching resistive heaters (HK5571, Minco, MN, USA) directly to the top of the chip. The heater was connected to a DC power source supplying a constant heat flux for generating a thermal gradient of about 40° C per chip height under no flow condition. The bottom of the chip was in contact with the aluminum chip holder, which was mounted on an aluminum heat sink. The set up exposed to the room temperature. During the experiments, temperature of the front surface of the chip was monitored and recorded by an IR camera (A320, FLIR, OR, USA) which was connected to a PC. The emissivity of 0.95 was considered by default for all the experiment sets. The sensitivity of the IR camera is about 0.1 °C at 25 °C. In predicting the temperature based on the IR signal, the FLIR software assumes that only the surface is emitting IR, and none is transmitting from the interior of the material. This assumption is correct, since the bolometer used in this model only collects IR in the wavelengths between 7.5 and 15 μm , while the optical transmission of glass is essentially

zero for wavelengths above 5 μm . For the constant temperature mode, it is required to use a controller and a thermopile.

Two syringe pumps (KDS100, KD Scientific, MA, USA), (7801001, Fisher Scientific, NH, USA) were used to inject the 10 ml plastic syringes at constant flow rates. All the experimental set up components were mounted on an optical table (Newport, CA, USA) to avoid the possible alteration in the relative location of the chip with respect to the camera. A picture of the setup is shown in **Figure 5-17**:

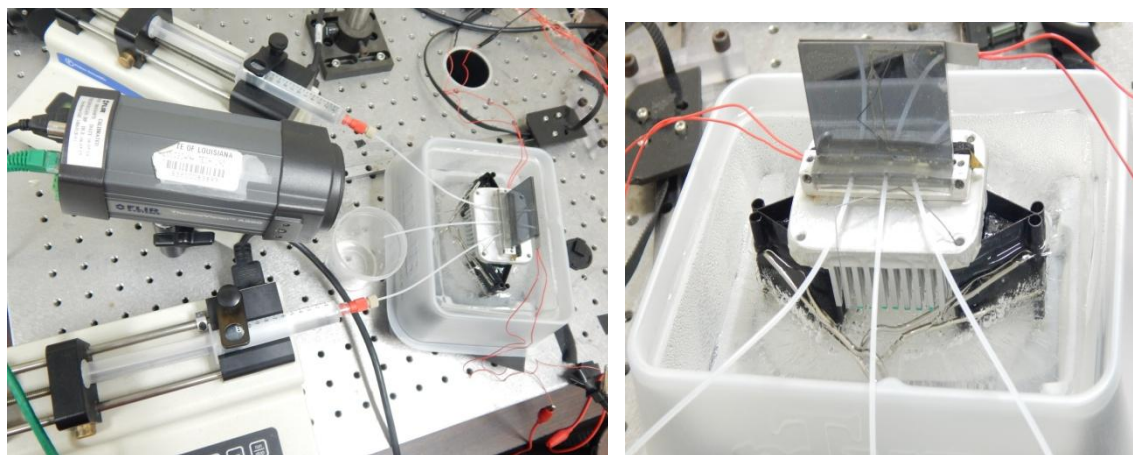


Figure 5-17: Picture of the setup used for GS experiment. The heat sink in ice/water was used to sink the heat and generate a gradient of 40 $^{\circ}\text{C}/\text{chip}$.

Generating a wide thermal gradient for a glass/silicon chip demands high power consumption as for a fixed gradient, ∇T , the volumetric heat is proportional to the thermal conductivity ($Q = k\nabla T$). Moreover, a more efficient heat dissipation technique is necessary. Therefore, in the case of glass/silicon chips, the heat sink was immersed in an ice/water container to maintain a constant temperature.

The mean power applied by the DC power to generate the gradient for the glass/glass chip was about 1.87 W, for glass/quartz about 2.09 W, and for silicon was between 7 and 8.1 W.

The IR images were being recorded as a movie during the whole experiment using the ExaminIR™, the camera's thermographic software platform for monitoring the process. The temporal plots on several regions of interest (ROIs) in the software were the criteria for deciding about the steady state condition of the system. Volumetric flow rates from 2 to 26 ml/hr (even values) were injected during each experiment set. **Figure 5-18** shows an example of the temporal plot of a representing ROI that connects the top and bottom of a glass/quartz direct-flow chip for flow rates of up to 20 ml/hr. After each flow, a non-flow condition was performed and recorded to minimize the errors associated with the change in the power of the heater, air convection alteration, and any relative displacement of the image frame with respect to the camera.

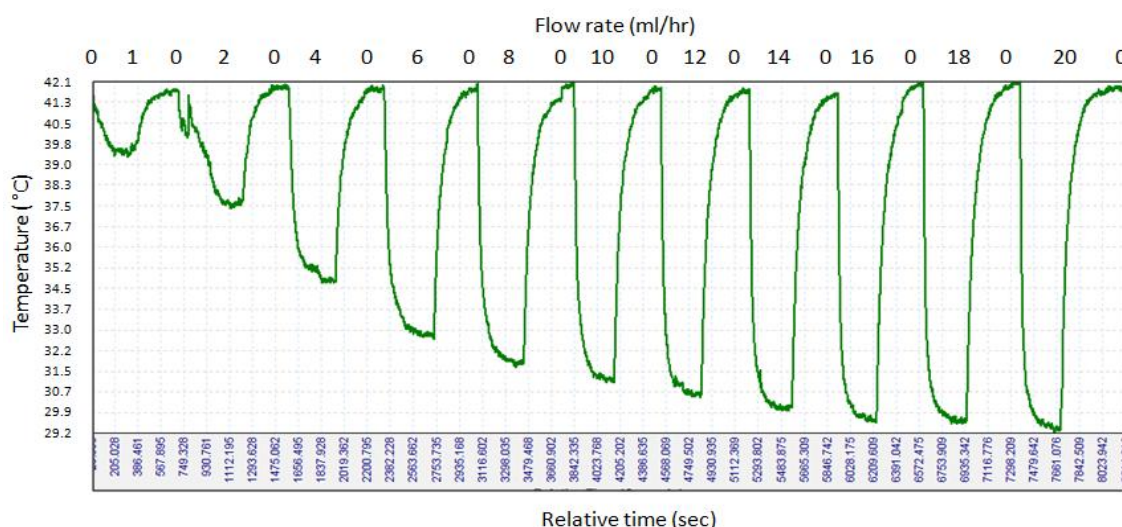


Figure 5-18: Temporal plot of an ROI in the GQDF experiment. Flow rates of 1, 2, 4... 20 ml/hr were used in each syringe pumps. The system is approximately in steady-state when the curve plateaus.

Three images were selected from the supposedly steady state part of any thermal event in order to reducing the role of artifacts and exported as .mat files for further analysis in MATLAB. To select the images, temporal plots of multiple horizontal and

vertical ROI lines located at different regions were used simultaneously so that the images did not represent any local abnormal thermal event. Since each injection time was at least 4 minutes, using large syringes is highly recommended to avoid the syringe refilling process, which in turn causes the inevitable frame change.

Another source of artifact in the behavior of the device and consequently the recorded thermal image is from the air bubbles that stick to the microchannel walls. At low flow rates, the inertia force of the fluid cannot overcome the adhesion force between the air bubble and microchannel wall. As a result, a big chunk of air bubble piles up and probably expands under the applied heat. The bubble narrows the channel locally, cause an enormous change in the temperature that shows itself as a discernible asymmetry in the iso-thermal lines at the channel location. There are many possibilities for the source of air bubbles: PDMS ports, trapped air bubbles between the tape and substrate layers, the connections between the syringe and tubing, and of course the air dissolved in the water. Although degassing the working fluid reduces the dissolved air bubbles in the water (a significant amount of air is dissolved in the tap water), the problem was still unsolved. The amount of air bubbles was significantly higher in the xerography chips when heated. This could be due to the expansion of the air bubbles between the layers or creeping of the air into the channel region close to the heater.

Interestingly, it was observed that the air bubbles in the direct flow chips were less stationary even at low flow rates. A similar observation can easily be made by comparing the temporal plot of the counter-flow with the smooth temporal plot of direct-flow xerography chips. When the flow rate is higher bubbles start to move. The movement of the air bubbles makes the temporal plot of counter-flow chips noisier,

especially at ROI's close to the channel area. It was observed that air bubbles start to move at lower flow rates when the working fluid is IPA or ethanol. Hence, about 10% IPA was added to syringes used in the GGCF and GQCF experiments. To observe the noisy behavior of the CF chips, the temporal plot of **Figure 5-18** can be compared to the temporal plot of the GQCF chip tested over flow rates ranging between 2 to 20 ml/hr shown in **Figure 5-19**. A similar observation was made by comparing the GG chips and GS chips. It was observed that the noise amplitude at flow rates below 4 ml/hr is in the order of temperature variation that resulted from the flow-induced effect. This means that in the presence of major noise sources such as DC power variation and bubbles, it is very difficult to detect the flow-induced effects from the flow rates below the 4 ml/hr.

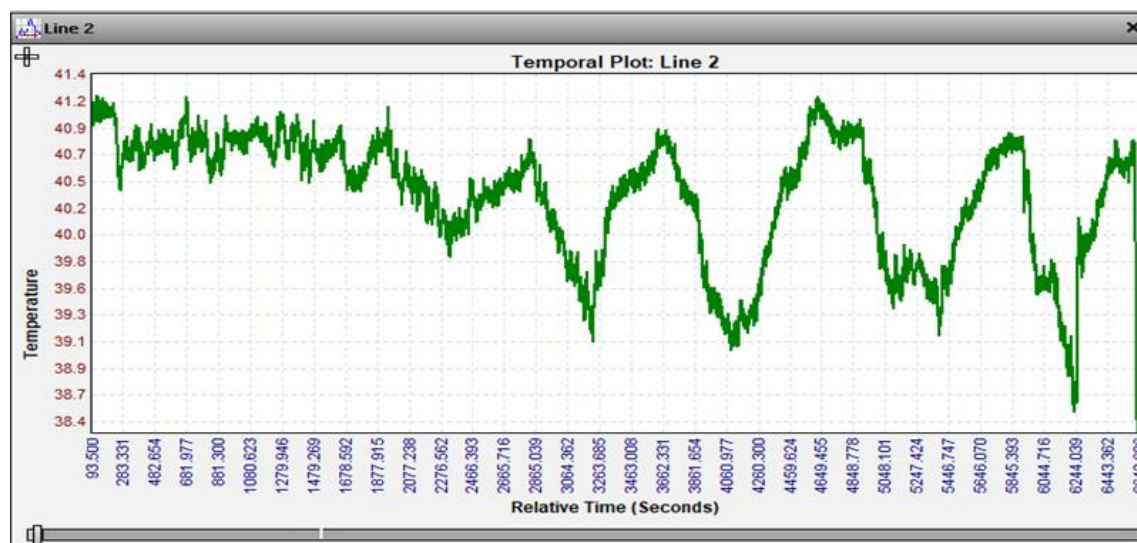


Figure 5-19: Temporal plot of an ROI in the GQCF experiment. Flow rates of 2, 4, 6 ... , 20 ml/hr were used in each syringe pumps.

5.5 Experimental Results

5.5.1 Ramp Rate

Ramp rate is one of the most important characteristics of a microfluidic heating component. A rough estimation of the ramp rate G [°C/sec] assuming a uniform gradient and neglecting the temperature difference between the fluid and solid wall is:

$$G = \frac{Q \Delta T}{A L} \quad \text{Eq. 5-21}$$

where L is the length of the channel, Q is the volumetric flow rate, A is the channel cross section, and ΔT is the temperature change from inlet to the outlet. For a GS chip, G is estimated to be $4.28Q$ [°C/sec] while for xurography chips the average ramp rate is $2.88Q$ [°C/sec] because of a larger cross section, where Q is expressed in [ml/hr]. The highest G was achieved for a GSCF with the flow rate of 30 ml/hr, but a smaller thermal gradient of 0.8 °C/mm made a ramp rate of about 103 °C/sec.

For a thermal distribution which is not linear or when the direction of the flow and gradient are not the same, local $G(x,y)$ can be defined as:

$$G(x, y) = \vec{V} \cdot \nabla T \quad \text{Eq. 5-22}$$

which can be integrated over the flow path:

$$G = \int_c G dl \quad \text{Eq. 5-23}$$

5.5.2 IR Thermal Data Analysis

The IR data captured from the ExaminIR™ software was saved as .mat files for further analysis in MATLAB. Despite the struggle to capture the IR images in a similar frame by fixing the distance and angle of the camera with respect to the chip, there was an undeniable inconsistency due to syringe refilling, chip replacement, and arbitrary

movements of the chip (especially for GS experiments conducted in the ice/water container). Therefore, a MATLAB code was written to tackle this issue by trimming the thermal map of the chip from the surrounding.

In order to reduce the errors due to artifacts such as unwanted movements, uncontrolled changes in the temperature of the heaters due to fluctuations in the power source, and variation of the room temperature, three frames were selected from the quasi-steady-state section of the IR data and were averaged. Moreover, the experiments were repeated multiple times especially for the counter flow chips. All the analyses performed are based on the averaged data. Additionally, the temperature change due to each flow rate was compared individually and independently with the no flow condition right before the corresponding flow condition (Figure 5-18). This minimizes both the artifacts due to inconsistent heating and temperature hysteresis.

5.5.3 Linearity of the Distributions

Linearity of the thermal distribution was specifically investigated at the two parallel channel areas of the chip designed for the placement of the sensor.

The measure defined here for quantification of the linearity degree in the distributions compares the area between the actual thermal curve (blue area) and the area of the triangle made by the linear distribution (blue added by red) as demonstrated in

Figure 5-20:

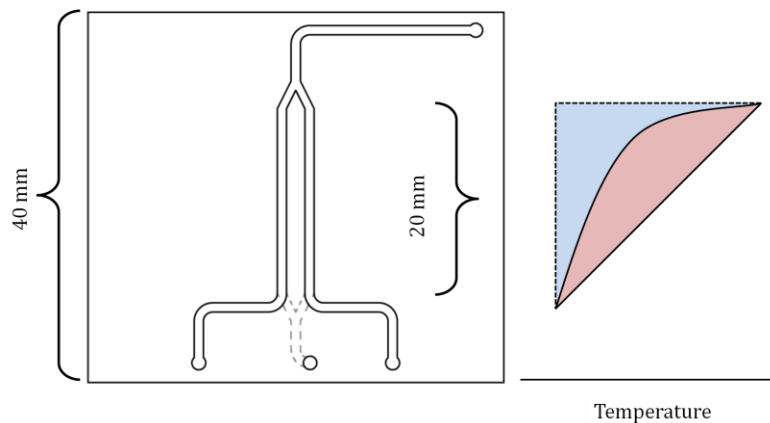


Figure 5-20: Schematic of the areas defined for the linearity measure. The 20 mm "parallel flow region" is where the results are evaluated in this chapter.

Using this measure, the impact of flow on linearization of each case is demonstrated in Figures 5-21, 5-22, and 5-23.

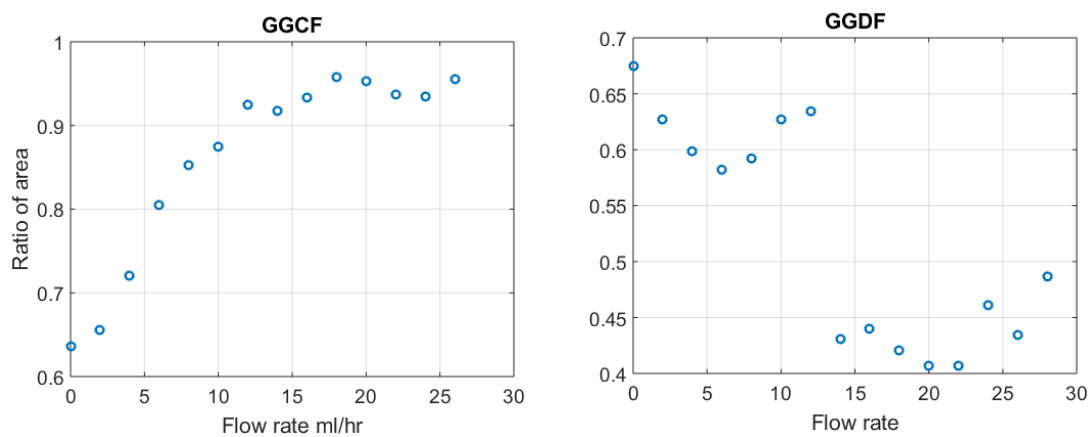


Figure 5-21: Linearity measure for GGCF and GGDF at different flow rates evaluated at the centerline of the parallel region (**Figure 5-20**)

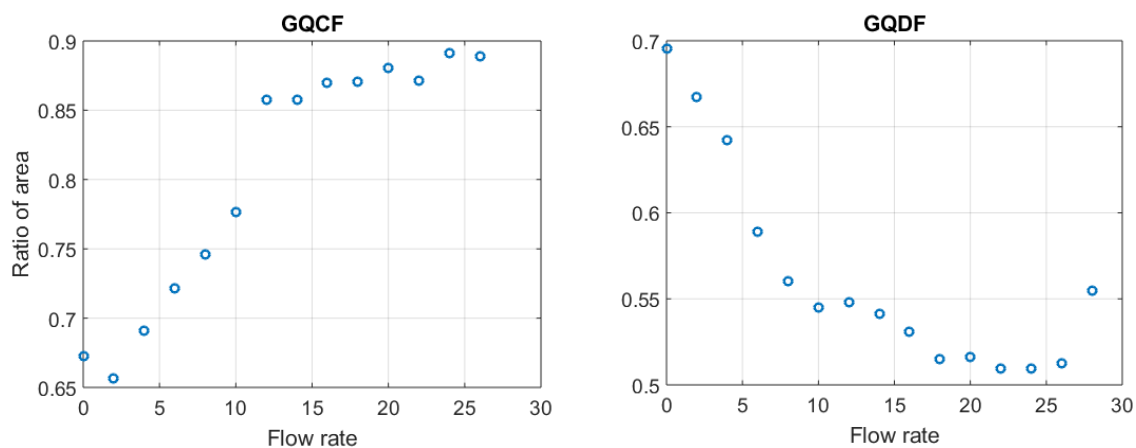


Figure 5-22: Linearity measure for GQCF and GQDF at different flow rates

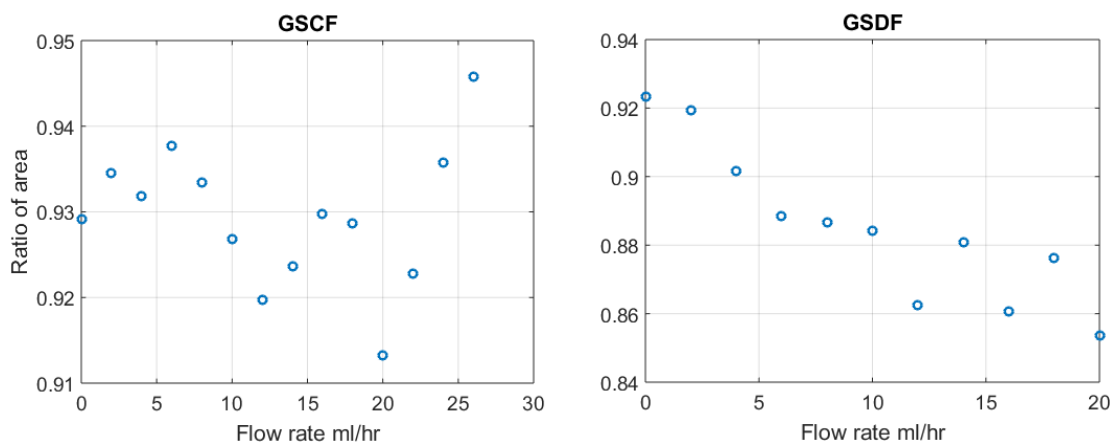


Figure 5-23: Linearity measure for GGCF and GGDF at different flow rates

The reason that cases were plotted separately is that they were not exactly at the same thermal condition (set temperature, heater attachment). However, CF and DF cases were at very close thermal conditions.

As can be seen, the flow helps the linearization in the CF cases while it deteriorates the linear distribution in DF cases. Also, the variation in the linearity caused by flow in the GS chips is small. The GSCF case has a very stable linearity performance

due to flow and there is not a very clear trend except for the high flow rates while in the GSDF, the flow causes a visible reduction in the linearity measure.

5.5.4 Regional Temperature Variation due to Flow

In order to demonstrate the flow induced effect at different regions, the IR data of the flow was subtracted by the corresponding no-flow data captured right before the flow condition. Introducing such a parameter reduces the abnormalities caused by the heater non-uniformity and the convection given that these factors were the same at flow and no flow conditions. The temperature difference between flow and no flow conditions, $\Delta T_{f,NF}$ was plotted for GGCF and GGDF at the flow rate of 10 ml/hr as shown in **Figure 5-24**.

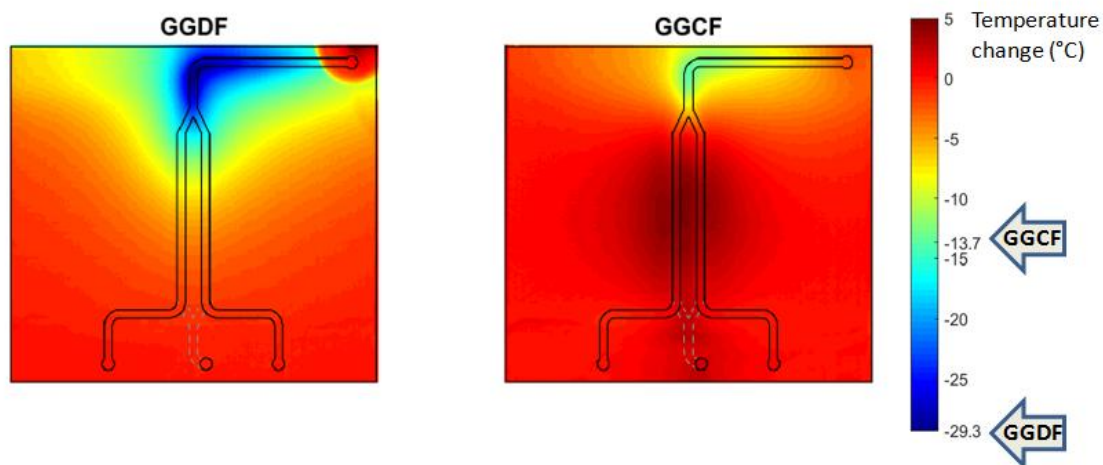


Figure 5-24: Temperature difference map between the 10 ml/hr flow rate and no plotted for GGDF and GGCF chips from the IR data. The maximum decrease of each chip is shown by arrows pointing to the color bar.

The highest temperature reduction due to the flow occurs at the channel bends where the two parallel channels merge. For the DF, the reduction of temperature at that region is almost twice that of the CF case. In both cases, the outlet is hotter under the

flow condition as the flow drags the heat when it passes through the heater region. For comparison, $\Delta T_{f,NF}$ was plotted for all the six chips in **Figure 5-25**.

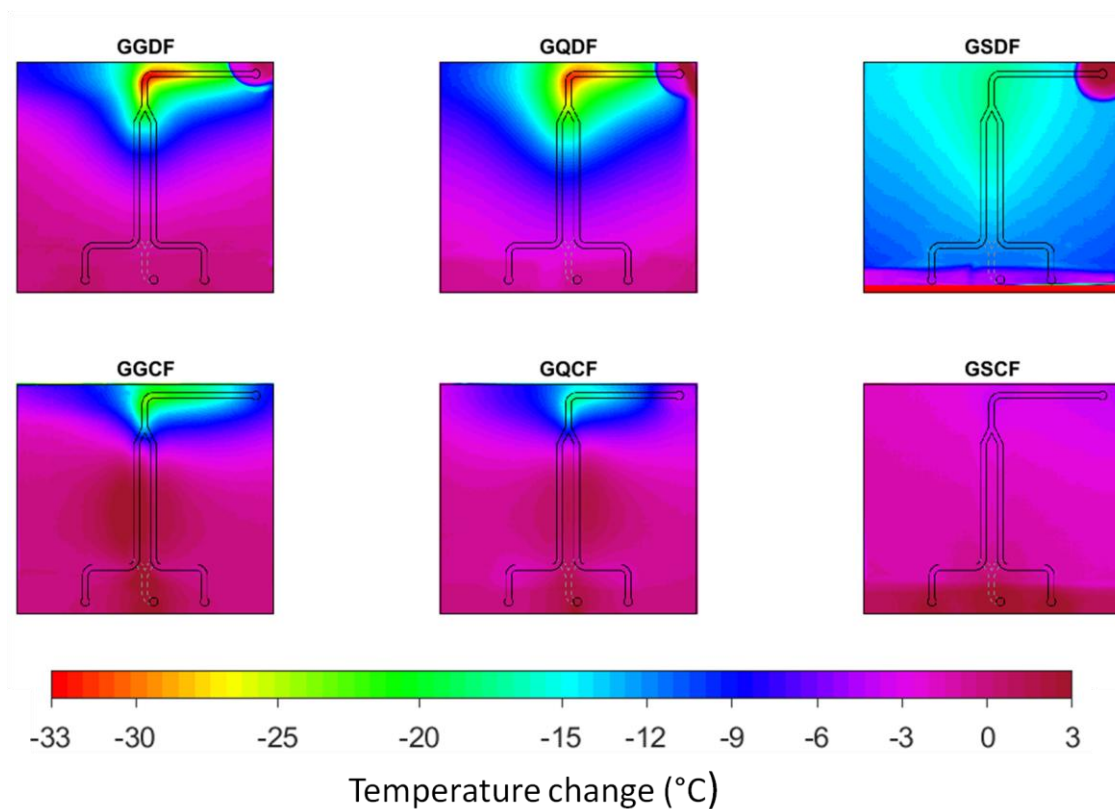


Figure 5-25: Temperature difference between the flow condition of 20 ml/hr and the no flow condition plotted from the IR data of the six configurations. The same colormap was used for all the chips for better comparison.

The DF chips are all colder than the CF chips. If a temperature change of ± 3 K is considered acceptable, then the purple range shows the region of the chips not experiencing a significant thermal change between the flow and no flow conditions.

Figure 5-25 shows that the temperature of the GSCF is almost invariant (an average of -1 K at the parallel channel region). Both GQCF and GGCF experience an increase in the temperature in the middle of the parallel channel region and a sharp decrease right before the junction.

Between the DF chips, the GSDF shows a comparatively uniform temperature change of -15 K. This value clarifies that it has no acceptable area under the 20 ml/hr flow condition. The acceptable area for GGCF is larger than the GGDF. In fact, the higher thermal conductivity chips show a more uniform $\Delta T_{f,NF}$; however, they obtain a smaller acceptable area (purple range) at high flow rates. In other words, a low thermal conductivity chip such as GGDF experiences a more intense reduction in the temperature (33 K at 20 ml/hr) compared to GSDF (about 17.3 K); however, due to its low thermal conductivity, the reduction is somehow isolated while in the GSDF it spreads to all regions.

To quantify the flow induced effects, the average $\Delta T_{f,NF}$ variation of a rectangular area (representing the thermal sensor) located at the bottom, middle, and top of the parallel channel region was calculated over flow rates.

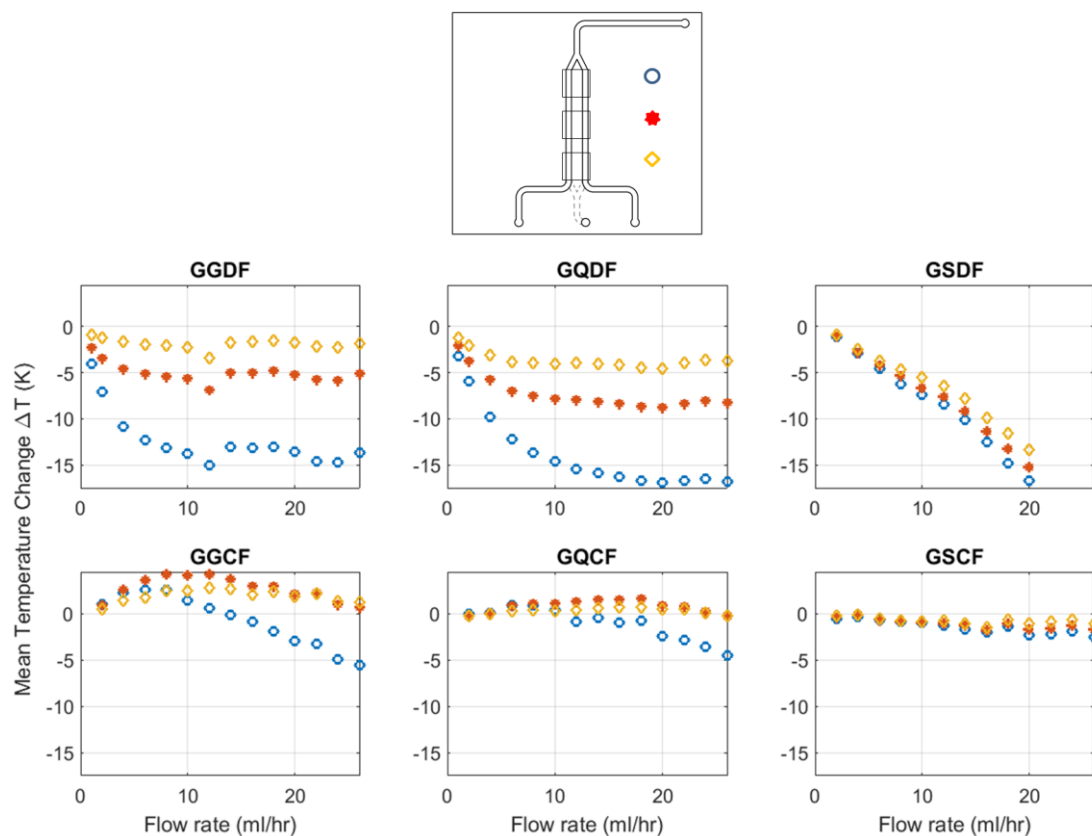


Figure 5-26: Temperature change due to flow evaluated at different regions. ΔT was evaluated at a 4 mm square located on bottom, middle, and top marked by \diamond bottom, * middle, and \circ top respectively as demonstrated on top figure

Results show that the smallest variation in all parts of the parallel flow region was achieved in GSCF. In both GGCF and GQCF chips, the temperature rises until a certain flow rate and then starts to cool down. The increase in the temperature in the middle of these two chips helps the linearization as the no-flow temperature distribution is saggy intrinsically. Despite the outstanding stabilization in the middle, both of these chips show a visible cooling at the top region, which is a drawback as the thermal stability at high temperature is both challenging and desirable.

5.6 Conclusion

The concept of counter-flow for thermal stability of the continuous flow thermal gradient chip was explained. A hybrid glass/silicon counter-flow chip consisting of two parallel channels designed for thermoelectric sensing was introduced, and the microfabrication procedure was explained. Hybrid glass/glass and glass/quartz counter flow chips were fabricated by low cost technique termed as xurography for comparison with the glass/silicon. For each chip, a similar direct flow chip was fabricated. All the six chips were tested over a wide range of flow rates and under a thermal gradient of about 40 °C along the chip length. The GS chips benefit from an excellent linearity of temperature due to high thermal conductivity. It was observed that the counter flow improves the linearity of the gradient while the direct flow makes it hyperbolic. The significant linearity improvement occurs for GGCF chips. As far as thermal stabilization goes, the GGCF chip shows an excellent performance at high flow rates.

CHAPTER 6

COUNTER-FLOW 3-D SIMULATION

6.1 Introduction

The IR thermography used for the measurement and characterization of the thermal-gradient microfluidic chips in the previous chapter only reveals the thermal map of the exterior surfaces facing the camera. The flow is where all important events take place. Mathematical modeling is a useful and powerful tool for obtaining additional information about the interior thermal field where applying the experimental methods have limitations or require complex configurations whose establishment is expensive and time consuming.

In the previous chapter, an analytical method was developed for explaining the mechanism of thermal stabilization using the counter-flow configuration.

Although the discussed 1-D analytical model considers the role of advection in changing the temperature of all solid layers, this model regards an equivalent dimension for the flow and solid domains because it neglects the third dimension normal to the page. This description is a reasonable simplification in the proximity of the channels, but in general, it exaggerates the role of advection in comparison with the conduction in the solid chip. This simplification is valid especially in the analysis of heat exchangers where the fluid and solid domains are comparable. However, in the thermal gradient

configuration proposed in this dissertation, the aim is to apply a known temperature to the fluid (for example, to start a temperature dependent reaction in a biological reactor) using the conduction in the solid rather than using the fluid to imply a specific thermal distribution. Of course, there are examples in which the thermal gradient is applied by either the fluid streams [96] or controlled by the flow [97], but those configurations are not the subject of this study. In other words, we are talking about a microfluidic chip in which the channel volume is much smaller than the solid of the chip. On the other hand, if it is assumed that the solid temperature is completely unaffected by the flow, then the problem can be expressed as standard internal forced convection configuration with walls subject to either constant heat flux, Q , wherever the flow is normal to the isothermal lines or subject to constant temperature, T , wherever the flow is horizontal to them. The solution to these problems quantifies the difference between the mean flow temperature and the channel wall temperature. Such an analysis was performed by Crews et al. explaining the impactful parameters on the difference between the bulk and wall temperature of the channel in a thermal gradient.

However, as discussed and demonstrated in the same article the flow is in fact *able to* distort the thermal distribution of the solid. The importance of such a distortion was demonstrated in a practical case such as PCR where the practical thermal gradient vanishes after a certain flow rate [3].

In summary, the goal of the design is to apply a known temperature to the fluid through the conduction mechanism. Thus, the space dedicated to the fluid domain is much smaller than the solid. However, the assumption that the temperature of the solid is

unaffected by the fluid is not precise, and gets violated rapidly by increasing the flow rate.

As a matter of a fact, *coupled* heat transfer occurring between the flow and the chip governs the overall thermal behavior of these microfluidic devices. A better term for this mechanism is "conjugate heat transfer" used for describing the "mutual thermal effect of the solid body and fluid flow on the heat exchanging between them" [98]. This is a common case in microchannel heat sinks in which heat is conducted from a hot surface to the channels and transferred by advection caused by flow of the working fluid. The coupled mechanism of heat transfer makes it a complicated problem and consequently, presenting a closed form analytical solution for these types of problems has been yet the subject of the interest for many researchers.

Various modeling approaches for the heat transfer in the microchannel heat sinks depending on their complexity are summarized by Liu [99]. Despite the accuracy of these models for design phase of such devices, they are all 2-D models and based on a simplified geometry.

For the problem in hand, obtaining a more comprehensive analytical solution demands the consideration of heat transfer in all directions. Solving the complete form of the equations in all three dimensions converts the ODE's into PDE's and the multi materials used increases the number of coupled PDE's resulting in a very complex problem. Therefore, developing an analytical solution will be significantly more tedious. As a result, 3-D simulation can be a practical way to tackle this problem.

6.2 Governing Equations

The conjugate nature of the heat transfer in this problem implies the simultaneous solution of the energy equation in the solid and fluid. The governing equations based on the conservation of mass, linear momentum, and energy are:

$$\text{Continuity equation} \quad \nabla \cdot \vec{V} = 0 \quad \text{Eq. 6-1}$$

$$\text{Momentum equation} \quad \vec{V} \cdot \nabla \vec{V} = -\frac{1}{\rho} \nabla p + \nu \nabla^2 \vec{V} \quad \text{Eq. 6-2}$$

$$\text{Fluid energy equation} \quad \nabla \cdot (\vec{V}(\rho E + p)) = k_f \nabla^2 T_f \quad \text{Eq. 6-3}$$

$$\text{Solid energy equation} \quad \nabla^2 T_s = 0 \quad \text{Eq. 6-4}$$

The assumptions leading to this format of governing equations are: Steady state, incompressible flow (low Mach number), negligible buoyancy force ($0.0003 < \beta_w < 0.0006$), laminar flow (maximum $Re \approx 127$), and no-slip condition on the solid walls (mean free path of water is in the order of few Angstroms while the smallest dimension of the channel is 65 microns resulting in $Kn \approx 10^{-6}$).

In the microfluidic mixers, the increased mixing occurs when the engulfment regime is present. In this case, vorticities occur at the cross section of the channel and significantly increase the mixing. Due to the addition of these vorticities, complete modeling requires very fine grids [53]. However, according to the findings of different research works including those conducted by Bothe's, Mauri's, and Salvetti's groups, this regime usually occurs when the aspect ratio of the channel is small while in the devices fabricated or modeled in this work, the aspect ratio of the channel is high (larger than 10), which delays the critical Reynolds number corresponding to the engulfment regime.

Therefore, the regular laminar flow model without grid resolution and significantly fine computational cells can be used.

Since the two inlets were injected by DI water, buoyancy term due to density mismatch of the two streams is neglected in **Eq. 6-2**, unlike the water/ethanol mixing case of Chapter 3.

6.3 Model Geometry

The AutoCad file of the photomask was used as the base geometry for generating the CAD of the model. Location and shape of inlets and outlets, and the hole connecting the front and back channels were modified in order to make the mesh generation process easier. Location of the inlets and outlet was transferred to the edge of the chip and instead of the hole connecting the front and back, a bypass channel was designed at the side edge of the chip. Additionally, the trapezoidal cross section resulted from the anisotropic etch of the silicon was replaced by a rectangular cross section resembling an anisotropic dry etch process. The thin bonding SU-8 layer and the PDMS ports attached to the inlets/outlet were neglected in the CAD. However, for xurography chips, the polyimide tape layers were considered in the model. Therefore, the CAD models of the microfabricated devices consist of three solid layers, while the CAD models of xurography devices include five solid layers.

In the primary models, the top edge of the chip was assigned as the heating surface. However, it was observed that the dimension of the heater and its connection from one side of the chip were influential in the thermal distribution of the chip; therefore, in the final models a block with the similar dimensions of the actual heater was

designed at the back side of the chip. CAD picture of the chip with a strip representing the heater is shown in **Figure 6-1**:

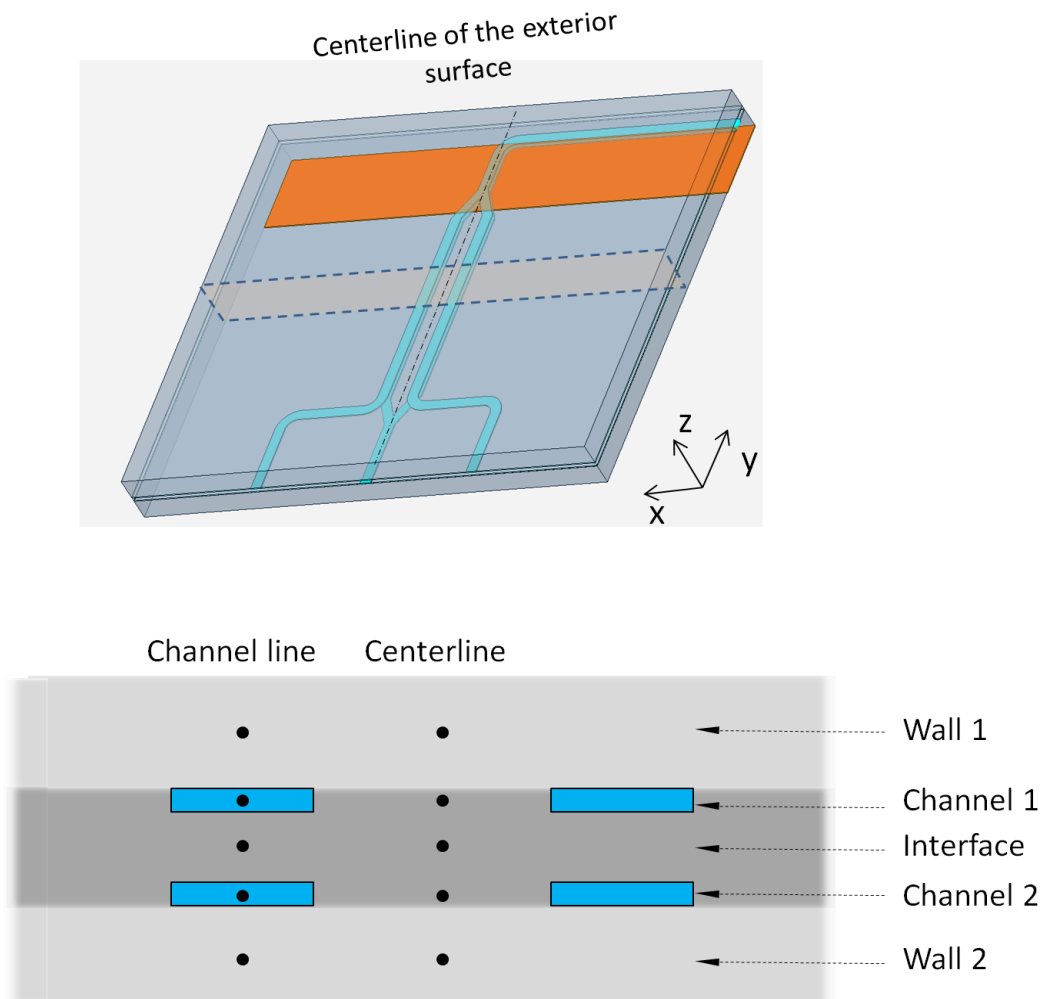


Figure 6-1: CAD of the microfluidic chip with heater attached on back, plotted in the SpaceClaim (Ansys, PA, USA). The orange strip on top is the heater. Bottom figure shows the cross section of the chip at the channels proximity.

The high aspect ratio features in the CAD along with the mismatch between the patterns of front and back makes the mesh generation process very challenging. To address it, the geometry was broken into a series of "sweepable" bodies which were significantly easier to be meshed. As a result, the whole domain was meshed by

hexahedra structured grids. There are two incentives for spending such a significant time for generating a structured hexahedral mesh instead of the automatic unstructured tetrahedral mesh: first the structured hexahedral mesh allows very large aspect ratios while the same aspect ratio in the tetrahedral mesh is equivalent to a very large skewness for the computational cells, which in turn degrades the accuracy and convergence of the simulation; second, a domain meshed by hexahedral mesh occupies noticeably fewer number of cells compared to the tetrahedral meshes which simply means the reduced memory usage [52].

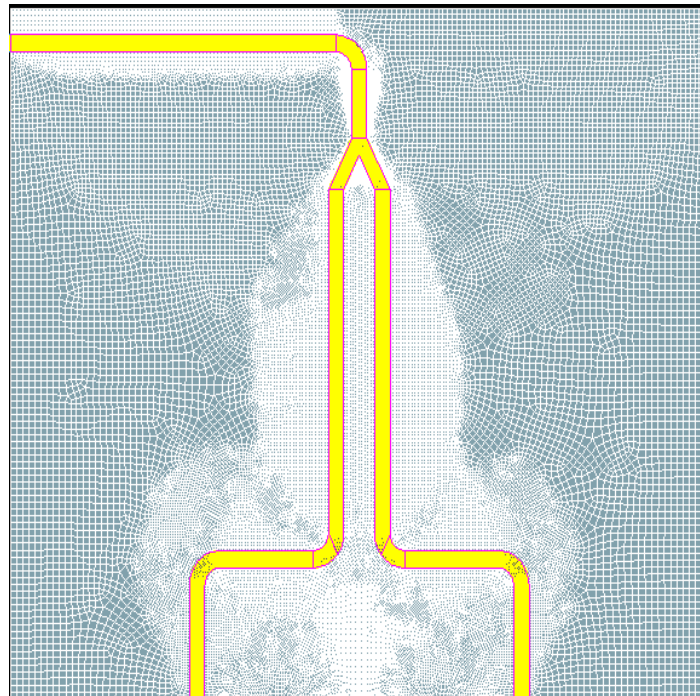


Figure 6-2: Meshed geometry in the Gambit (Fluent®, PA, USA)

6.4 Boundary Conditions

The boundary conditions specified for the heat transfer in the solid were similar to those applied for the thermal gradient chip explained in chapter 3. The most impacting

difference is the method of generating the thermal gradient. Similar to the discussion made in the 1-D analytical solution, depending on the configuration of the heating system, either constant Q or constant T boundary conditions are possible. Applying a stable constant T requires a temperature control system and a special design for the heating platform in order to distribute the temperature uniformly. In contrast, applying a constant Q generates a more stable temperature distribution and is very straightforward. In the experiments, only constant Q boundary condition was applied.

In the simulations and analytical models, thermal behavior of the chips under these two boundary conditions and the thermal performance under the flow condition will be studied. A heat flux proportional to the actual heater was used in the simulations. However, since the heater is not the subject of interest here, the flux was adjusted in a trial and error process for the no flow condition, so that the generated thermal gradient was similar to the experimental data.

All the surfaces exposed to the ambient air were subject to constant convection coefficient:

$$-k \frac{\partial T_s}{\partial n} = h(T_s - T_\infty) \quad \text{Eq. 6-5}$$

As demonstrated in chapter 3, the convection coefficient is remarkably important in the thermal gradient systems. However, as the focus of this chapter is on the impact of the internal flow on the thermal gradient, the typical value of $20 \text{ W/m}^2 \cdot \text{K}$ was considered for the simulations.

The bottom surface of the chip was in contact with the chip holder attached to the heat sink and consequently was not exposed to the ambient air. Estimating the thermal resistance of a complex configuration consisting of the chip holder and heat sink is not

straightforward. Therefore, the temperature of the cold side was extracted from the IR data. In a set of simulations, the convection boundary condition was applied to the bottom surface, while in another set, constant room temperature was applied. It was observed that the constant room temperature boundary condition resulted in better similarity with the IR data.

In the GS experiments with the ice/water mixture, the constant temperature boundary condition was achieved by keeping the heat sink in contact with a large heat capacity medium at a fixed temperature. Therefore, constant T boundary condition at the cold side was applied without hesitation.

For the two inlets, constant volumetric flow rates were assigned and for the outlet, outflow boundary condition was considered. The two inlet temperatures were set at ambient temperature.

6.5 Validation

6.5.1 Validation Procedure

IR data of the experiments is used against the 3-D simulation for validation of the model. As a visual demonstration, temperature contour of both simulation and experimental results were plotted using MATLAB. As explained previously, in the simulation with no flow, the heat flux applied at the surface representing the heating surface of the heater was adjusted in a trial and error procedure so that a similar temperature range (at the centerline of the chip) was generated, and then, the same flux was maintained under the flow condition to imitate the actual experiment. This procedure was repeated for all six chips independently, even for counter-flow and direct-flow versions of the chips due to the fact that the experimental condition was not identical.

Inconsistent attachment of the resistive heaters, angle and distance between the IR camera and the chip, and even the size of the PDMS ports are among the major sources of the difference between the experimental conditions.

6.5.2 Thermal Contours

Here, a visual demonstration is used to display the similarities between the simulation and experimental results. For each set of GG, GQ, and GS chips, thermal contours of no flow and flow condition (10ml/hr) was shown for direct-flow and counter-flow.

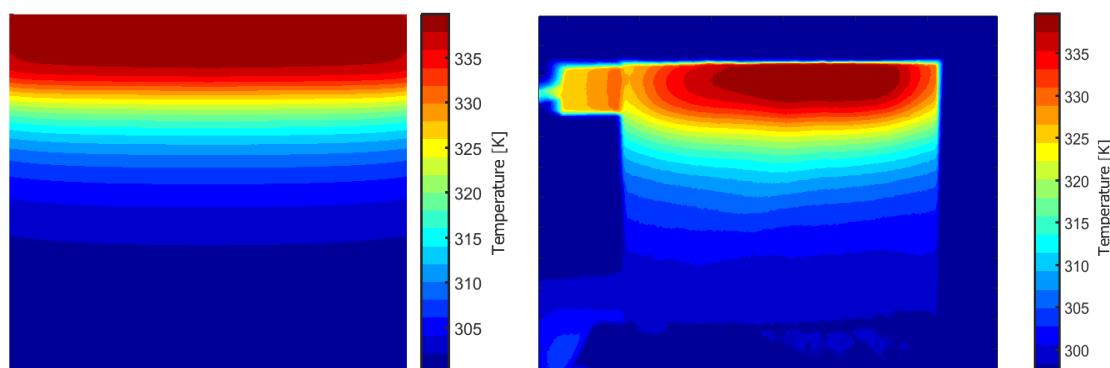


Figure 6-3: Thermal gradient of the exterior surface of the GGCF chip (top surface of **Figure 6-1**) when there is no flow (left) Simulation (right) Experimental

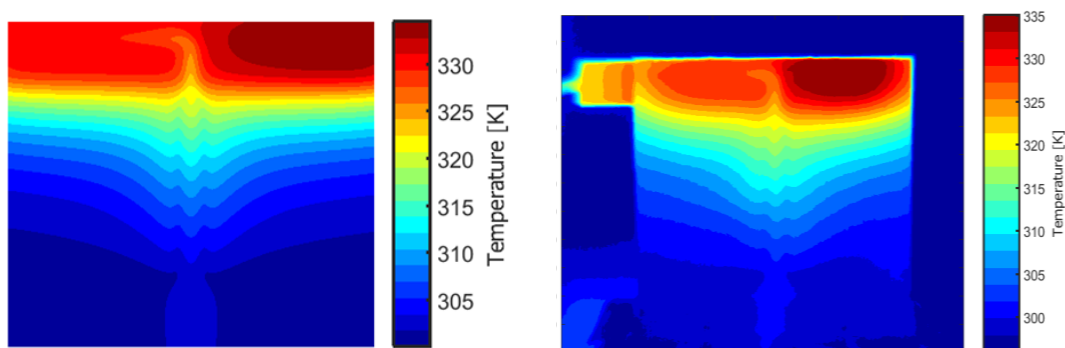


Figure 6-4: Thermal gradient of the exterior surface of the GGCF chip when there

is no flow (left) Simulation (right) Experimental

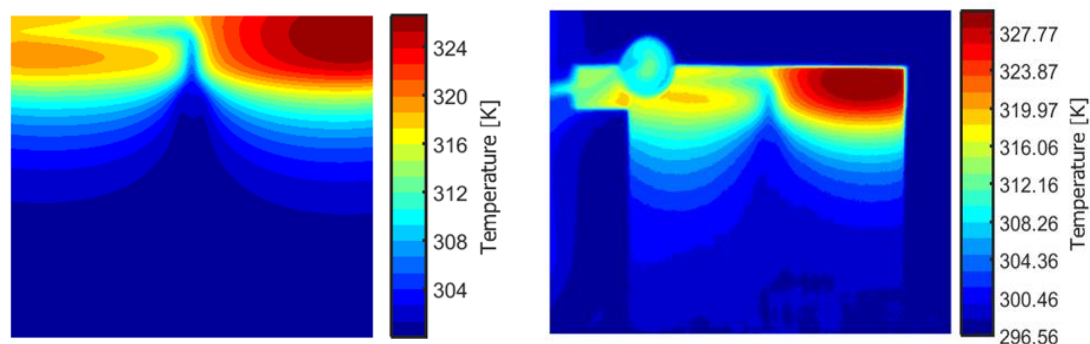


Figure 6-5: Thermal gradient of exterior surface of the GGDF chip affected by flow at 10 ml/hr (left) Simulation (right) Experimental

A Similar set of plots are plotted for the GQ and GS chips. The results of the GQ chips are similar to the GG chip. However, the wider gradient at no flow condition (**Figure 6-3** compared with **Figure 6-6**), which demonstrates the more linear gradient resulted from the higher thermal conductivity of quartz. For GS chips though, the thermal distribution is significantly different, due to the distinguishable high thermal conductivity (**Figure 6-9**).

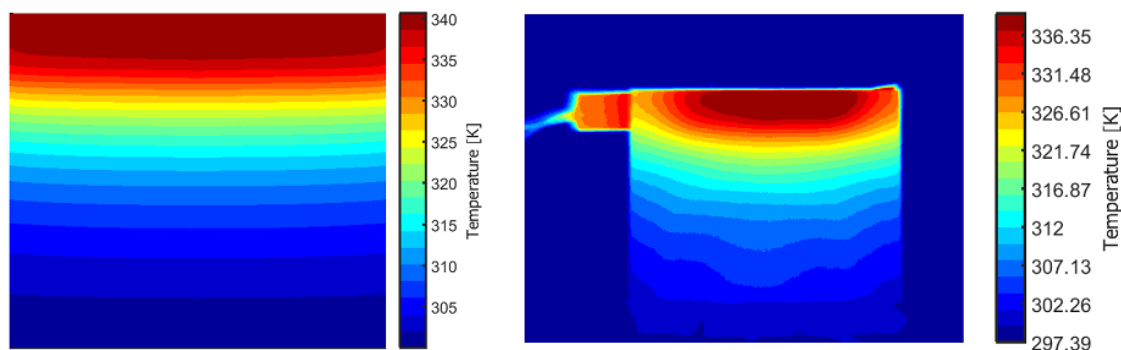


Figure 6-6: Thermal gradient of exterior surface of the GQCF chip when there is no flow (left) Simulation (right) Experimental

The difference between the performance of the GG and GQ chips are more visible under the flow condition.

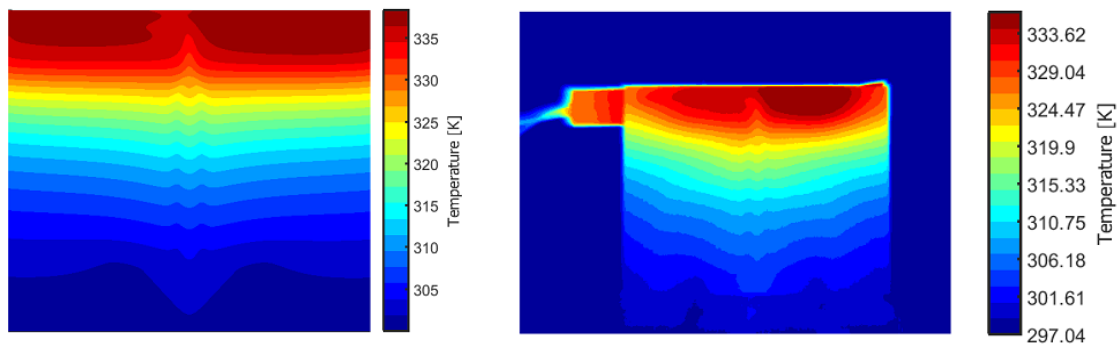


Figure 6-7: Thermal gradient of exterior surface of the GQCF chip affected by flow at 10 ml/hr (left) Simulation (right) Experimental

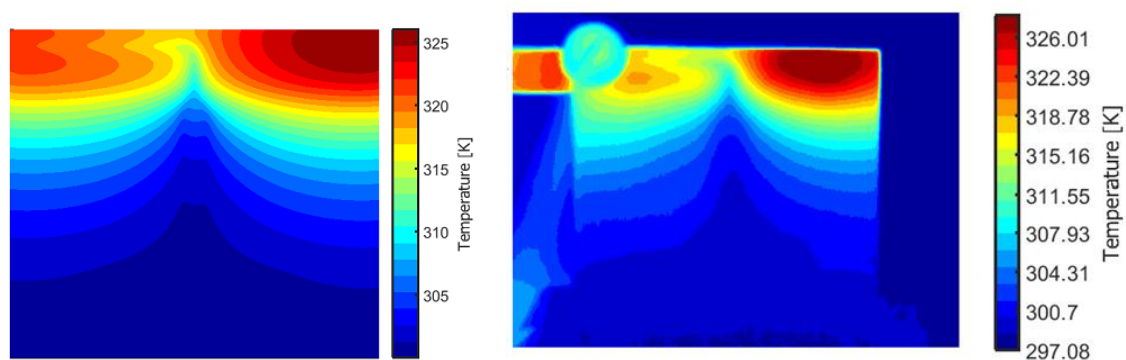


Figure 6-8: Thermal gradient of exterior surface of the GQDF chip affected by flow at 10 ml/hr (left) Simulation (right) Experimental

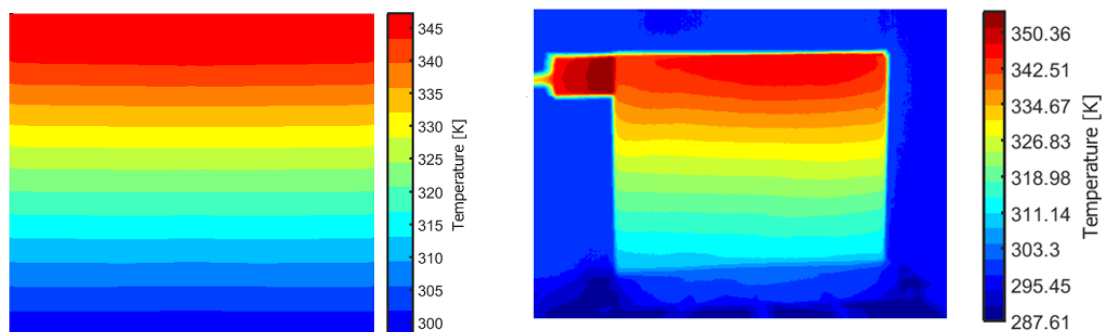


Figure 6-9: Thermal gradient of exterior surface of the GSCF chip when there is no

flow (left) Simulation (right) Experimental

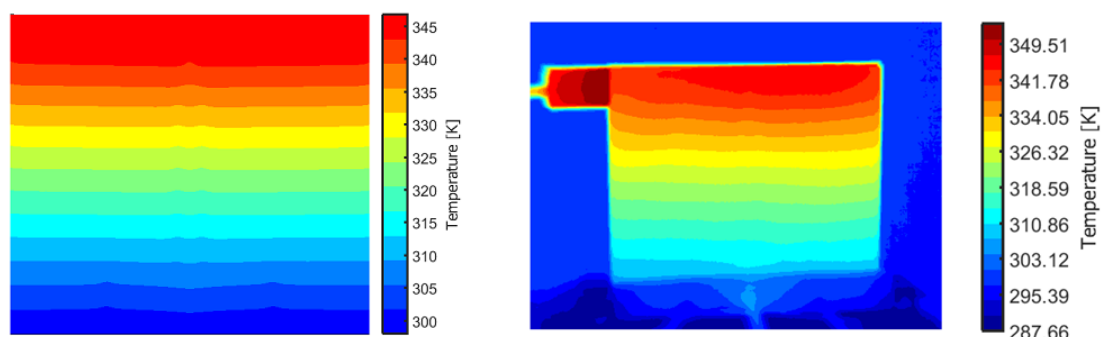


Figure 6-10: Thermal gradient of exterior surface of the GSCF chip affected by flow at 10 ml/hr (left) Simulation (right) Experimental

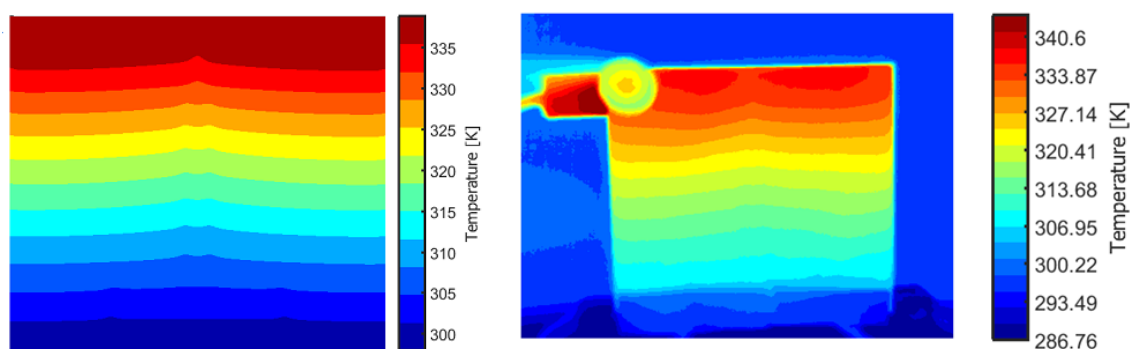


Figure 6-11: Thermal gradient of exterior surface of the GSDF chip affected by flow at 10 ml/hr (left) Simulation (right) Experimental

6.5.3 Centerline Temperature

For a better comparison of the simulation and experimental data, temperature is plotted at the centerline of the chip. The results are in an excellent agreement. The noticeable difference in the temperature at the bottom of the chip is mainly due to the large PDMS inlet ports (4 to 7 mm thick) attached to the cold side.

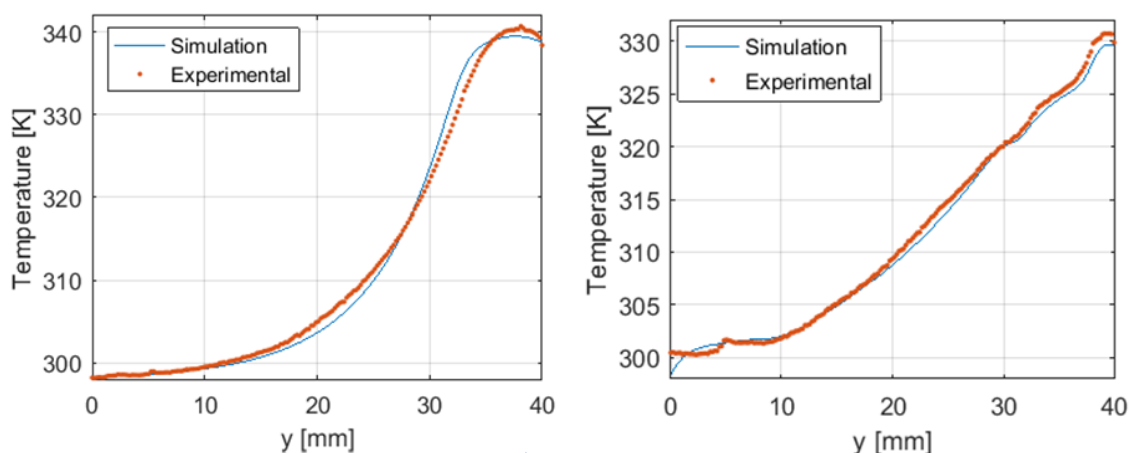


Figure 6-12: Temperature along the centerline of GGCF chips from the simulation and experimental plotted for (left) No flow (right) 10 ml/hr plotted along the centerline of the exterior surface in the y -direction indicated in **Figure 6-1**.

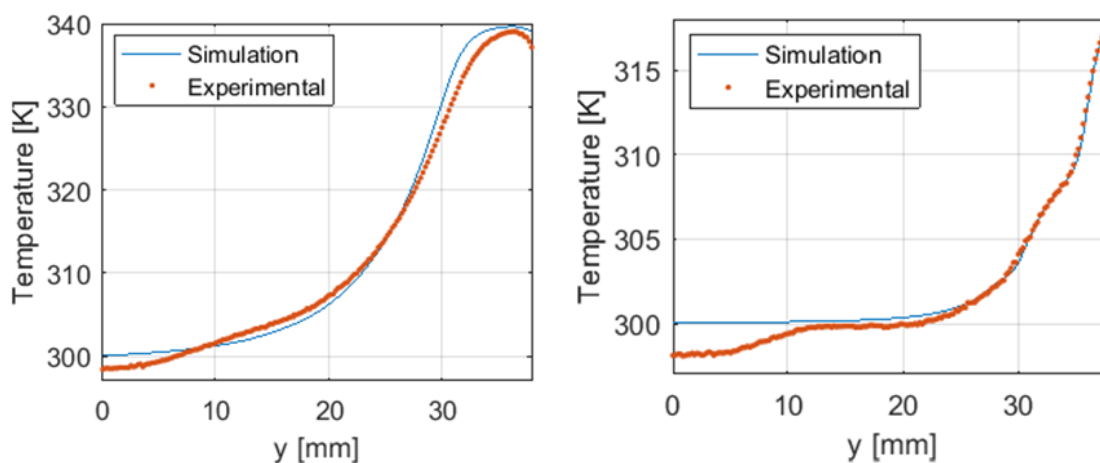


Figure 6-13: Temperature along the centerline of GGDF chips from the simulation and experimental plotted for (left) No flow (right) 10 ml/hr plotted along the centerline of the exterior surface in y -direction as indicated in **Figure 6-1**.

6.6 Results and discussion

6.6.1 Constant T Instead of Constant Q

After validating the simulations using the experimental data, the trustworthy model can be used for predicting the performance of the device at other configurations. In

this part, thermal performance of the device under the constant T instead of constant Q is evaluated. Similar to the procedure for applying the constant Q boundary condition, in a trial and error process, temperature of the heating surface was adjusted to reproduce a thermal distribution on the front face similar to that of constant Q case at no flow condition and then, thermal distribution was examined under the flow.

Centerline temperature of the GGCF and GGDF chips were plotted under the 10 ml/hr flow rate in **Figure 6-14**:

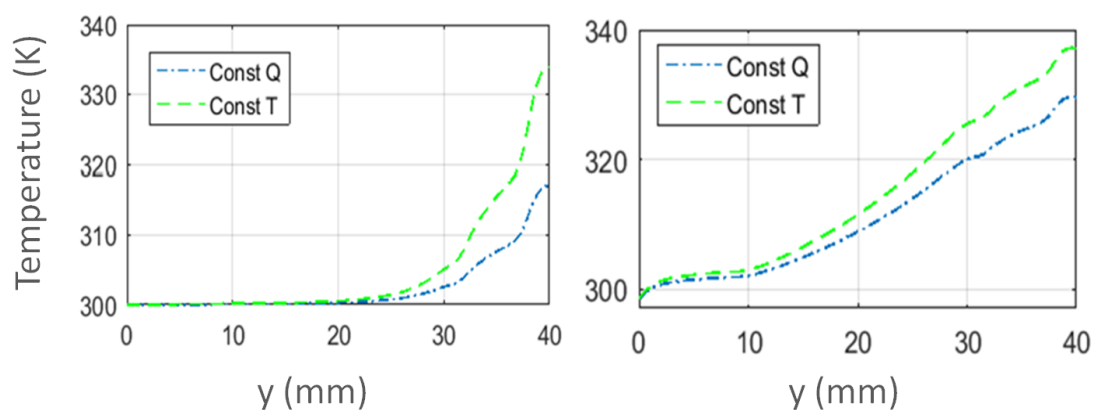


Figure 6-14: Comparison between the constant temperature and constant heat flux condition under the flow of 10ml/hr (left) GGDF and (right) GGCF. The temperature profile was plotted along the centerline of the exterior surface of the chip (y-direction) as indicated in **Figure 6-1**

Evidently, the constant Q boundary condition results in a wider gradient for both CF and DF chips. However, as can be seen, the temperature difference between the constant T and constant Q conditions is much more for the DF chip, especially at the hot side of the chip.

In general, the goal is to establish a fixed thermal gradient and this observation shows how constant T condition better suits this goal. However, if constant Q condition is used instead of constant T (the total heat power required in the constant T is considerably

more than constant Q condition under the flow condition), this will lead to more variation in the DF chip compared to CF chip under the flow condition. In other words, counter-flow chip recycles the dissipated heat (similar to heat regeneration cycle).

6.6.2 Temperature in the Layers of the Chip

One interesting observation which is the outcome of the mathematical modeling is the thermal distribution in the chip layers including the flow channel. It was originally observed in the 1-D analytical solution of chapter 5 that the thermal distribution between the layers of the chip deviates from each other when the flow rate increases (**Figures 5-5 and 5-6**). This suggests that the advection term behaves like a variable thermal resistance term unlike the thermal resistance terms due to the material of the chip and the contact resistance. Regarding the application of the device, it can be deduced that it is an adverse behavior undermining the straightforward relationship between the sensing surface (exterior) and the channel temperature where the thermal event occurs. Therefore, knowing the relationship between the temperature of the surface and the temperature of the flow is important especially for spatial temperature monitoring and device calibration when a sensor is integrated. Simulation is a practical tool for finding this relationship.

To investigate this effect, temperature at the middle of each layer was plotted along the centerline of the GG and GS chips. As it can be seen in **Figure 6-15**, the temperature difference between the layers expands almost uniformly with flow rate.

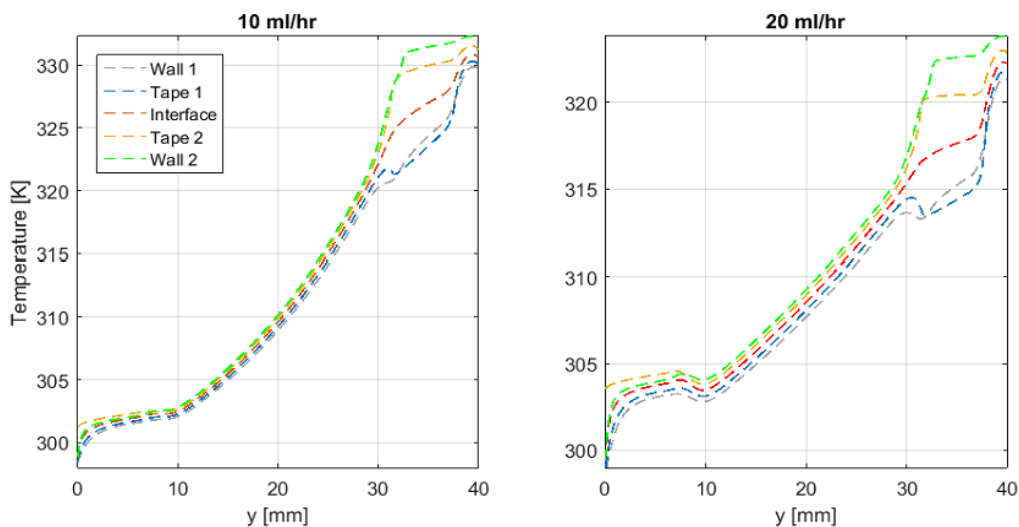


Figure 6-15: Thermal distribution of the GGCF layers plotted along the centerline of the layers of the chip (in y-direction) passing the middle of each layer (as indicated in **Figure 6-1**) for flow rates of (left)10ml/hr (right) 20ml/hr

For the GS chip, temperatures of the layers are almost the same at parallel flow region (10 to 30 cm) (**Figure 6-16**). This is a very good characteristic of the GS chip.

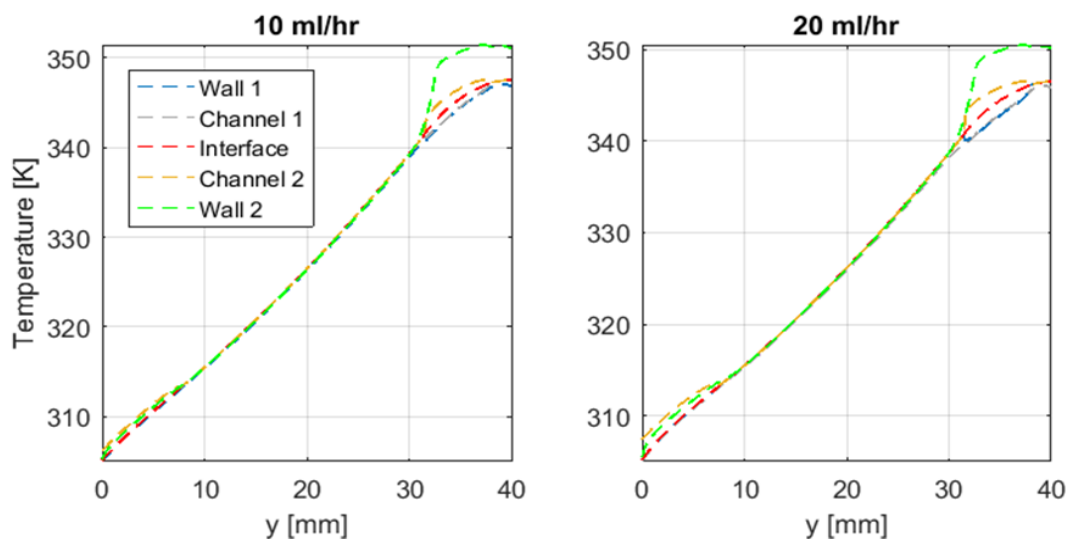


Figure 6-16: Thermal distribution of the GSCF layers plotted along the centerline of the layers of the chip (in y-direction) passing the middle of each layer (as indicated in **Figure 6-1**) for flow rates of (left)10ml/hr (right) 20ml/hr

It should be noted that the centerline of the chip does not pass through the channels. If instead of the centerline, a line passing one of the channels is plotted, the temperature distribution will be very different.

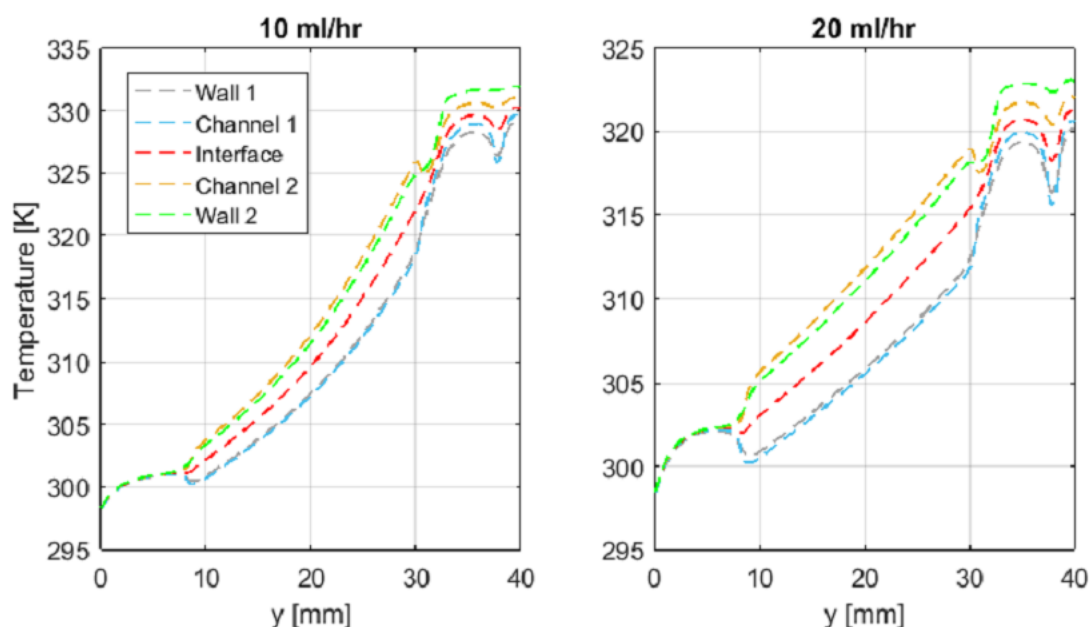


Figure 6-17: Thermal distribution of the GGCF layers plotted along the channel line (indicated and showed in **Figure 6-1**) instead of the centerline in y-direction, for flow rates of 10ml/hr (left) and 20ml/hr (right)

Interestingly, the temperature difference between the layers is not equally spaced; Temperature of the channel and walls are close while the temperature difference between the interface and channels is large. This is totally in agreement with the analytical model (**Figure 5-5** and **Figure 5-6**), and once again, confirms the fact that the analytical model describes the physics of the device at the channel proximity.

Even for the GS chip, if the temperature of the layers is evaluated at the channel instead of the chip centerline, a visible variation will be observed as shown on **Figure 6-18**:

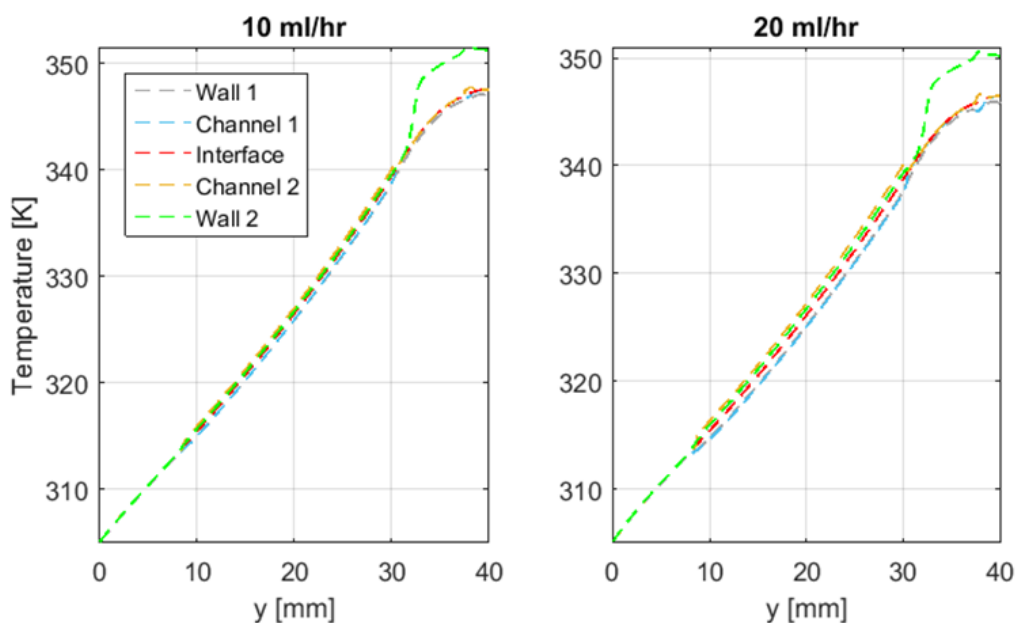


Figure 6-18: Thermal distribution of the GSCF layers plotted along the channel line (indicated and showed in **Figure 6-1**) instead of the centerline in y-direction, for flow rates of 10ml/hr (left) and 20ml/hr (right)

6.6.3 Thermal Distribution in the Depth

The plots of the previous chapter demonstrated how the thermal distribution at the proximity of the channel differs with the centerline of the chip. Here, the temperature in the depth of the chip is investigated at a line passing through the depth of the device (z-direction) at a line crossing a channel in the middle of the chip ($y=20$). The temperature was plotted for GGCF and GSCF chips over different flow rates.

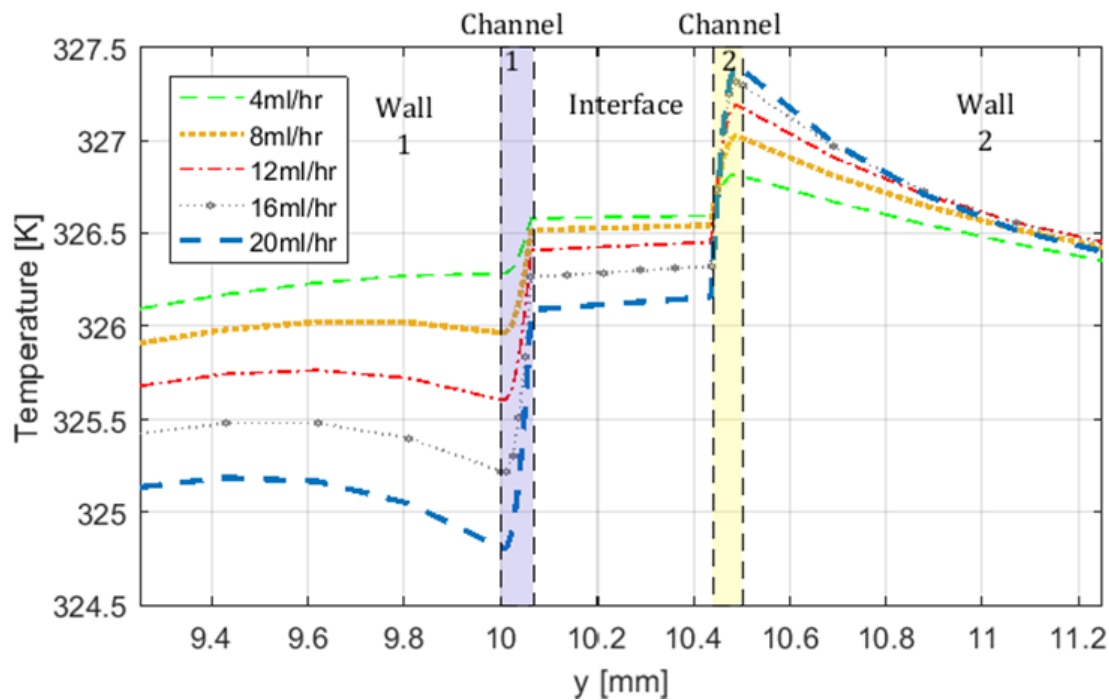


Figure 6-19: Thermal distribution of the GSCF in the depth of the chip (z direction in Figure 6-1) plotted over different flow rates

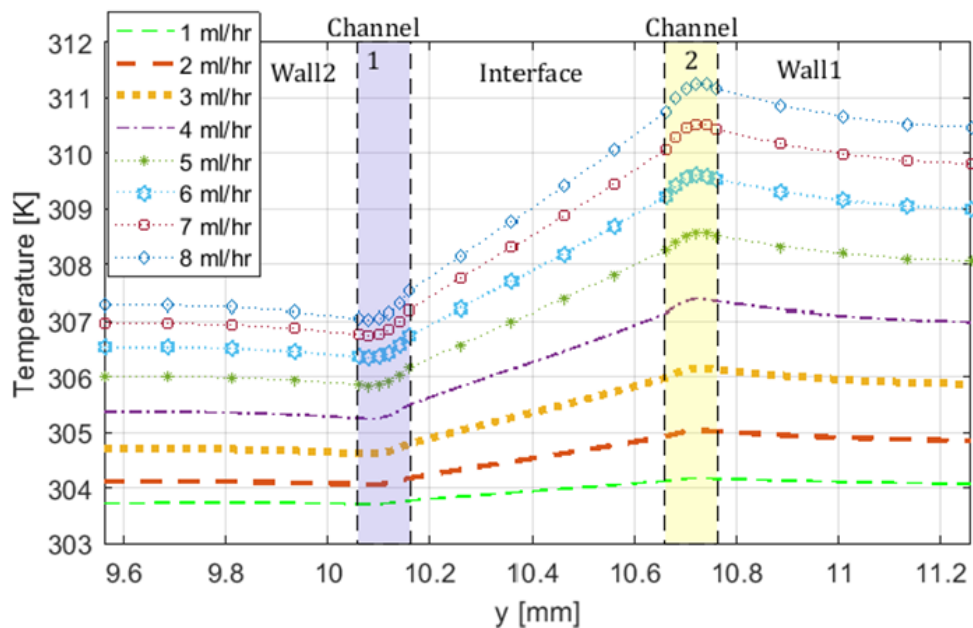


Figure 6-20: Thermal distribution of the GGCF in the depth of the chip (z direction in Figure 6-1) plotted over different flow rates

Although the total temperature change in the depth for the GS chip is much smaller compared to GG chip, the variation in the channel, which is dominantly governed by convection in both GS and GG chips, is in the same order. If the parameter ΔT_{ch} is defined as the maximum temperature variation in the channel depth, at low flow rates, it is almost equal for both chips, and at higher flow rates, it is more for GS chip. The values of ΔT_{ch} of both GG and GS chips are summarized in **Table 6-2**.

Table 6-1: ΔT_{ch} evaluated for GG and GS chips at different flow rates.

Flow rate (ml/hr)	GGCF (ΔT_{ch})(K)	GSCF (ΔT_{ch})(K)
4	0.3	0.3
8	0.5	0.5
12	0.7	0.8
16	0.7	1.1
20	0.7	1.3

In this sense, the GS chip does not outperform. According to the discussion of the Reference [2], in the fully developed region, when the internal flow is governed by constant Q boundary condition, the difference between fluid bulk temperature and the wall temperature linearly depends on the volumetric flow rate:

$$T_w - T_m = C \frac{\dot{V} dT_m}{\alpha dy} \quad \text{Eq. 6-6}$$

where T_m and T_w are bulk (mean) temperature of the fluid and wall temperatures, constant C depends on the cross section geometry.

When the iso-flux term (dT_m/dy) is constant, and for a constant thermal diffusivity α , the temperature difference depends linearly on flow rate. For GS chip, the

iso-flux term is almost constant over all the flow rates used here (consider the slope of the channel temperature in **Figure 6-17**) while in the GG chip, this term decreases with flow rate (consider **Figure 6-18**). Therefore, at low flow rates, the $T_w - T_m$ is almost the same for the two chips, while at flow rates over 12 ml/hr the simultaneous increase of flow rate and the subsequent decrease of iso-flux term in the GG chip results in almost a constant ΔT_{ch} .

6.6.4 The Optimum Flow Rate for the Highest Signal

The counter-flow thermal gradient microfluidic developed in this dissertation is mainly designed for the iso-flux calorimetry explained in the introduction. One prominent application of iso-flux calorimetry is finding the melt temperature of DNA. However, a reversible exo/endermic process such as DNA melt can potentially set a limit on the maximum operational flow rate of the device for the highest signal detection. The condition leading to this scenario is explained here:

Imagine one inlet contains DNA and the other is buffer solution. In the front side of the chip, the two streams get heated up individually and equally when moving from the cold side to the hot side of the chip. The stream containing the DNA experiences an endothermic reaction as it reaches the DNA melt temperature while the other does not. In the back of the chip, the process is reversed with the difference that the DNA extension is an exothermic process and can possibly neutralize the heat released from the endothermic process occurring in front. In the front, the two streams are separate until they mix in the junction. Therefore, if the two streams are mixed completely, the anisotropic sensor does not sense the exothermic event occurring in back due to common mode rejection. However, if the mixing does not occur completely, unfavorable thermal asymmetry

reduces the signal generated on the front side. The problem is that in microfluidic, the mixing occurs through the molecular process rather than the convective process.

Therefore, in the microchannel, the length required for the complete mixing is often very long. The length required for complete mixing can be easily estimated in this way:

The complete mixing through the diffusion can be seen as a particle in one stream diffuses the distance from the interface to the opposite channel wall. For equal flow rate and viscosity, the time scale t_d for it to happen is:

$$t_d = \frac{w^2}{4D} \quad \text{Eq. 6-7}$$

where w is the channel width and D is the diffusion coefficient. For the mean velocity \bar{V} , and channel thickness t , the length of the channel l allowing the complete mixing can be estimated as:

$$l = \frac{\bar{V}w^2}{4D} = \frac{\dot{V} w}{t 4D} \quad \text{Eq. 6-8}$$

The diffusion coefficient of fluids in water is in $\mathcal{O}(10^{-9})$. So, for the dimension of the microchannel used here, when the flow rate is 1 ml/hr, the length needed for the full mixing is about 70 cm, and for 10 ml/hr, it needs to be 700 cm. So, it can be concluded that the two streams only mix completely at flow rates below 1 ml/hr. On the other hand, the higher the flow rate is, the higher rate of heat released due to DNA melt process.

Therefore, there should be an optimum flow rate for the highest signal depending strongly on the channel geometry and diffusion coefficient. Finding such a flow rate for reversible reactions as a function of impacting parameters can be another example for the usefulness of the simulation.

6.7 Conclusion

The thermal behavior of the chips fabricated and tested in Chapter 5 was examined using the 3-D simulations. The simulations show very good agreement with the experimental results in both the features and values. It was noticed that the constant T boundary condition results in a wider and more linear thermal distribution under flow condition compared to constant T for both DF and CF chips. However, if instead of constant T, constant Q is applied, the thermal distribution of the CF chip deviates significantly less from the constant T, compared to DF chip. Temperature distribution of the different layers of the chip was also evaluated, and it was observed if the temperature of the layers is evaluated at the channel proximity, even for the GS chip, there is a detectible difference between the temperature of the channel and solid. The temperature difference between the channel and the channel wall is almost the same for GG and GS chips under the flow rates of up to 12 ml/hr. For higher flow rates, this difference is almost constant for GG chip while for GS it continues to increase linearly with flow rate.

CHAPTER 7

CONCLUSION AND FUTURE WORK

7.1 Conclusion

Thermal linearization and stabilization of a continuous-flow thermal gradient microreactor was accomplished. This was achieved by careful material selection and flow path design. The counter-flow GS chip shows excellent stability in the thermal gradient at very high flow rates. This enables very rapid and stable ramp rates (up to 100 °C/sec). Moreover, the counter-flow design neutralizes the non-linearity imposed by the external convection even for GG chips.

The proposed design has further application in all the continuous-flow microfluidic devices involving the precise thermal control of the fluid for stabilization.

In this dissertation, a balanced cooperation between the idea, theory, and practice demonstrated the best outcome.

7.1.1 Achievements

A practical fabrication process was developed for a hybrid glass/silicon counter-flow chip including the design, photolithography steps, etching, and packaging. A 3-D numerical model for applying the heat of mixing (water/ethanol) was developed. After validation with the experimental data, the model was used for finding the optimum location of an anisotropic thermal sensor for detecting the highest signal. An analytical model for the thermal gradient chip, a time-dependent 3-D numerical model for the

natural convection around a cylinder predicting the result at a wide range of pressures, an analytical model for describing the performance of the counter-flow chip considering the axial conduction in the walls and the interface of the chip, and a 3-D model of the counter-flow and direct-flow thermal gradient chips were developed for deeper understanding of the governing physics and impactful parameters.

7.2 Future Work

This dissertation accomplished one essential step for the realization of an iso-flux calorimeter. Assembling the anisotropic thermopile sensor to the exterior of the chip with reference junctions aligned with the buffer stream and measuring junctions aligned with the stream containing the sample is the next step. Since the temperature sensor detects the temperature of the exterior surface, it is important to reduce the thermal resistance between the sensor and the thermal event. In the thermal sensor modeled in Chapter 3, 130 μm coverslip glass was used to address this issue. However, using a very thin glass to reduce the thermal resistance restricts the physical robustness of the device and therefore places a limit on the maximum allowable flow rate. To avoid it, thicker crystalline quartz of higher thermal conductivity can be used as the capping material on the front side of the silicon.

The indirect bonding using SU-8 showed acceptable performance and was a good technique as it does not need special instruments. However, the mismatch between the CTE of SU-8 and Si/SiO₂ applies stress to device. This is the probable reason for the delamination of some chips when they were used at a large thermal gradient and under high flow rates. Therefore, anodic bonding is recommended for attaching glass to silicon,

and fusion or other direct bonding techniques [100] are recommended for bonding quartz to silicon.

Despite the outstanding linearity in the GS chips, performing the experiments inside the box is still recommended for increased thermal stability. It is expected that the improvement due to enclosure be more significant for the chips with lower overall thermal conductivity.

The bottom surface of the channel etched by KOH anisotropic etch was noticeably rough. This may influence the biological samples containing large molecules such as DNA or proteins. Numerous works have been done by researchers for optimizing the recipe of KOH solution to minimize the roughness [86, 101]. DRIE of silicon using Bosch process and a successive isotropic wet etching for smoothing surface roughness is also a more expensive (but low throughput) alternative for achieving a smoother channel with vertical side walls.

A heating platform plays a central role in the thermal gradient microfluidic chip. From the simulation results, it was demonstrated that the difference between thermal gradient at no-flow and flow condition is less when a constant T condition is applied compared to the constant Q. Therefore, a heating system for establishing a stable and uniform temperature is really beneficial.

During the experiments, it was observed that the bubbles are one of the main sources of thermal irregularities, especially for the CF chips. Addressing this issue is very critical for an accurate temperature measurement. Significant improvement is expected from applying wafer bonding techniques with no adhesive, thereby sealing the microchannel from the diffusion of the outside air. However, besides the degassing of the

sample liquids, seeking bio-compatible surfactants that facilitate the movement of the bubbles is highly suggested.

APPENDIX A

MATLAB CODE FOR 1-D COUNTER-FLOW MODEL

```
function bvp4CFwidth
R = .04; % microchannel length [m]
x1 = 0; x2 = R;
solinit = bvpinit(linspace(x1,x2,1000),320*ones(1,8));
%initialization
sol = bvp4c(@bvp4ode,@bvp4bc,solinit);
xint = linspace(x1,x2,1000);
T = deval(sol,xint);
figure(1)
% subplot(1,3,1)
hold on
for i=[1,3,4,6,7]
plot(xint,T(i,:), 'LineWidth',2);
end
legend('Tw1','Tc1','Tint','Tc2','Tw2')
box on
grid on
xlabel('y [mm]')
ylim auto
ylabel('Temperature [K]')
%-----%
function dydx = bvp4ode( x,y )
%% parameters
w = .001; % channel width [m]
th = .0001; % direct channel thickness [m]
Dhh = 2*(w*th)/(w+th); % hydraulic diameter of the hot channel
Nu = 5; % estimated Nusselt number from the Simulation
kw = 0.6; % thermal conductivity of the working fluid (water)
[W/m.K]
hh = Nu*kw/Dhh; % convection coefficient of the flow
kg1 = 1.38; % glass1 thermal conductivity
tg1 = .0005; % glass1 thickness
hinf = 20; % convection coefficient of air
Tinf = 300; % ambient air temperature [K]
rho = 998.2; % density of water [kg/m^3]
m_in = 20*2.78e-7; % mass flow rate channel 1 [kg/sec]; 2.78e-
7[kg/sec] equals 1ml/Hr in a 1*.1 mm channel section
Vbar1 = m_in/(rho*th*w); % Inlet mean velocity [m/s]
Cp = 4182; % specific heat capacity of water [J/kg.K]
```

```

tint = .0005; % interface material thickness [m]
kint = 10; % interface material thermal conductivity
hc = hh; % convection coefficient of water for constant flux BC
[W/m^2.K]
Vbar2 = Vbar1;
tc = .0001; % counter channel thickness
tg2 = tg1;
kg2 = kg1;
%-----%
%% System of differential equation for a Boundary Value Problem%%
% y(1)=Tg1 & y(2)=dTg1/dx ; y(3)=Th ; y(4)=Tint;
% y(5)=dTint/dx; y(6)=Tc; y(7)=Tg2; y(8)=dTg2/dx
dydx(1) = y(2);
dydx(2) = hh/(kg1*tg1)*(y(1)-y(3))+hinf/(kg1*tg1)*(y(1)-Tinf);
dydx(3) = hh/(rho*Vbar1*th*Cp)*(y(1)+y(4)-2*y(3));
dydx(4) = y(5);
dydx(5) = hh/(kint*tint)*(y(4)-y(3))+hc/(kint*tint)*(y(4)-y(6));
dydx(6) = hc/(rho*Vbar2*tc*Cp)*(2*y(6)-y(7)-y(4));
dydx(7) = y(8);
dydx(8) = hc/(kg2*tg2)*(y(7)-y(6))+hinf/(kg2*tg2)*(y(7)-Tinf);
%-----%
end

function res = bvp4bc(ya,yb)
% Applying the boundary conditions
Tcold1=303; % Temperature of the glass1 at x=0
Tcold2=305 ; % Temperature of the glass1 at x=0
Thot1=340 ; % Temperature of the glass1 at x=R
Thot2=345; % Temperature of the glass2 at x=R
Tin = 300; % Temperature of fluid at inlet
Q = 12e3; % Wall flux Q'' applied at X=R Q value for
establishing a thermal gradient of about-
%- 40 degree at no flow is different for each material. For
GS=55e3,GQ=12e3, GG: 6.5e3 w/m^2
%%%%%%%%%%%%%%%%%%%%%%%%%%%%%%%%%%%%%%%%%%%%%%%%%%%%%%%%%%%%%%%%%%%%%%%%
res(1) = ya(1)-Tcold1; % Tg1(0) = Tcold1
res(2) = yb(2)-Q/kg1; %-kg1*dTg1/dx(R)=Q
% res(2) = yb(1)-Thot1 %For constant T Boundary Condition
res(3) = ya(3)-Tin; % Th(0) = Tin
res(4) = ya(4)-(Tcold1+Tcold2)/2; % Tint(0) = (Tcold1+Tcold2)/2
res(5) = yb(5)-Q/kint; %-kint*dTint/dx(R)=Q
% res(5) = yb(4)-(Thot1+Thot2)/2 %For constant T Boundary
Condition
res(6) = yb(6)-yb(3); % Th(R)=Tc(R)
res(7) = ya(7)-Tcold2; % Tg2(0) = Tcold2
res(8) = yb(8)-Q/kg2; %-kg2*dTg2/dx(R)=Q
% res(8) = yb(7)-Thot2; %For constant T Boundary Condition
end
end

```

BIBLIOGRAPHY

- [1] Bergman, T.L., et al., *Fundamentals of heat and mass transfer*. 2011: John Wiley & Sons.
- [2] Crews, N., et al., *Flow-induced thermal effects on spatial DNA melting*. *Lab on a Chip*, 2008. **8**(11): p. 1922-1929.
- [3] Thomas, S., R.L. Orozco, and T. Ameel, *Microscale thermal gradient continuous-flow PCR: A guide to operation*. *Sensors and Actuators B: Chemical*, 2017. **247**: p. 889-895.
- [4] Crews, N., et al., *Spatial DNA melting analysis for genotyping and variant scanning*. *Analytical chemistry*, 2009. **81**(6): p. 2053-2058.
- [5] Zhang, Y. and P. Ozdemir, *Microfluidic DNA amplification—A review*. *Analytica Chimica Acta*, 2009. **638**(2): p. 115-125.
- [6] Kopp, M.U., A.J. De Mello, and A. Manz, *Chemical amplification: continuous-flow PCR on a chip*. *Science*, 1998. **280**(5366): p. 1046-1048.
- [7] Hashimoto, M., et al., *Rapid PCR in a continuous flow device*. *Lab on a Chip*, 2004. **4**(6): p. 638-645.
- [8] Moschou, D., et al., *All-plastic, low-power, disposable, continuous-flow PCR chip with integrated microheaters for rapid DNA amplification*. *Sensors and Actuators B: Chemical*, 2014. **199**: p. 470-478.
- [9] Crews, N., C. Wittwer, and B. Gale. *Thermal gradient PCR in a continuous-flow microchip*. in *Microfluidics, BioMEMS, and Medical Microsystems V*. 2007. International Society for Optics and Photonics.
- [10] Lagally, E.T., P.C. Simpson, and R.A. Mathies, *Monolithic integrated microfluidic DNA amplification and capillary electrophoresis analysis system*. *Sensors and Actuators B: Chemical*, 2000. **63**(3): p. 138-146.
- [11] Nakayama, T., et al., *Circumventing air bubbles in microfluidic systems and quantitative continuous-flow PCR applications*. *Analytical and bioanalytical chemistry*, 2006. **386**(5): p. 1327-1333.
- [12] Wittwer, C.T., et al., *High-Resolution Genotyping by Amplicon Melting Analysis Using LCGreen*. *Clinical Chemistry*, 2003. **49**(6): p. 853-860.
- [13] Thapa, S., et al., *The thermopile: An anisotropic temperature sensor*. *Sensors and Actuators A: Physical*, 2012. **187**: p. 132-140.
- [14] Bejan, A., *Convection heat transfer*. 2013: John wiley & sons.

- [15] Tritton, D.J., *Physical Fluid Dynamics*. 2nd ed. 1988, New York: Oxford University Press.
- [16] Krishnan, M., et al., *Reactions and Fluidics in Miniaturized Natural Convection Systems*. Analytical Chemistry, 2004. **76**(21): p. 6254-6265.
- [17] Deen, W.M., *Analysis of transport phenomena*. 1998, New York: Oxford University Press.
- [18] Nestorova, G.G., et al., *Thermoelectric lab-on-a-chip ELISA*. Analytical Methods, 2015. **7**(5): p. 2055-2063.
- [19] Zhang, Y. and S. Tadigadapa, *Calorimetric biosensors with integrated microfluidic channels*. Biosensors and Bioelectronics, 2004. **19**(12): p. 1733-1743.
- [20] Duff, M.R., J. Grubbs, and E.E. Howell, *Isothermal Titration Calorimetry for Measuring Macromolecule-Ligand Affinity*. Journal of Visualized Experiments : JoVE, 2011(55): p. 2796.
- [21] Yoon, S.-I., et al., *Neisseria meningitidis detection based on a microcalorimetric biosensor with a split-flow microchannel*. Journal of Microelectromechanical Systems, 2008. **17**(3): p. 590-598.
- [22] Nestorova, G.G., et al., *Lab-on-a-chip thermoelectric DNA biosensor for label-free detection of nucleic acid sequences*. Sensors and Actuators B: Chemical, 2016. **225**: p. 174-180.
- [23] Esfandyarpour, H., R.F.W. Pease, and R.W. Davis, *Picocalorimetric method for DNA sequencing*. Journal of Vacuum Science & Technology B: Microelectronics and Nanometer Structures Processing, Measurement, and Phenomena, 2008. **26**(2): p. 661-665.
- [24] Blise, R., *Micromachined Differential Scanning Calorimeter for Cellular Differentiation and Metabolism Monitoring*. 2011.
- [25] Verhaegen, K., et al., *A high-throughput silicon microphysiometer*. Sensors and Actuators A: Physical, 2000. **82**(1-3): p. 186-190.
- [26] Wang, S., et al., *Micro-differential scanning calorimeter for liquid biological samples*. Review of Scientific Instruments, 2016. **87**(10): p. 105005.
- [27] Bhargava, K.C., et al., *Temperature Sensing in Modular Microfluidic Architectures*. Micromachines, 2016. **7**(1): p. 11.
- [28] Koppa, V.L. and E.J. Guilbeau, *Highly Sensitive Microfluidic Chip Sensor for Biochemical Detection*. IEEE Sensors Journal, 2017. **17**(20): p. 6510-6514.
- [29] Kwak, B., et al., *Dual thermopile integrated microfluidic calorimeter for biochemical thermodynamics*. Microfluidics and Nanofluidics, 2008. **5**(2): p. 255-262.

- [30] Lee, C., et al., *Micro-calorimeter with enclosed parylene chambers for bio/chemical applications*, in *12th International Conference on Miniaturized Systems for Chemistry and Life Sciences (μ TAS)*. 2008: San Diego, CA.
- [31] Lagally, E.T., C.A. Emrich, and R.A. Mathies, *Fully integrated PCR-capillary electrophoresis microsystem for DNA analysis*. *Lab on a Chip*, 2001. **1**(2): p. 102-107.
- [32] Neji, B., et al. *Micro-fabrication of an absolute flow calorimeter for DC to RF power measurement*. in *Circuits and Systems (MWSCAS), 2013 IEEE 56th International Midwest Symposium on*. 2013. IEEE.
- [33] Baier, V., et al., *Highly sensitive thermopile heat power sensor for micro-fluid calorimetry of biochemical processes*. *Sensors and Actuators A: Physical*, 2005. **123**: p. 354-359.
- [34] Lerchner, J., et al., *A new micro-fluid chip calorimeter for biochemical applications*. *Thermochimica Acta*, 2006. **445**(2): p. 144-150.
- [35] Lerchner, J., et al., *Miniaturized calorimetry--A new method for real-time biofilm activity analysis*. *Journal of microbiological methods*, 2008. **74**(2-3): p. 74-81.
- [36] Ahmad, L., et al., *Binding event measurement using a chip calorimeter coupled to magnetic beads*. *Sensors and Actuators B: Chemical*, 2010. **145**(1): p. 239-245.
- [37] Tangutooru, S.M., et al., *Dynamic thermoelectric glucose sensing with layer-by-layer glucose oxidase immobilization*. *Sensors and Actuators B: Chemical*, 2012. **166**: p. 637-641.
- [38] Kopparchy, V.L., S.M. Tangutooru, and E.J. Guilbeau, *Label free detection of L-glutamate using microfluidic based thermal biosensor*. *Bioengineering*, 2015. **2**(1): p. 2-14.
- [39] Nestorova, G.G. and E.J. Guilbeau, *Thermoelectric method for sequencing DNA*. *Lab Chip*, 2011. **11**(10): p. 1761-1769.
- [40] Wang, B. and Q. Lin. *A MEMS differential scanning calorimeter for thermodynamic characterization of biomolecules*. in *Micro Electro Mechanical Systems (MEMS), 2011 IEEE 24th International Conference on*. 2011. IEEE.
- [41] Muehlbauer, M.J., et al., *Thermoelectric enzyme sensor for measuring blood glucose*. *Biosensors and Bioelectronics*, 1990. **5**(1): p. 1-12.
- [42] Zieren, M. and J.M. Kohler. *A micro-fluid channel calorimeter using BiSb/Sb thin film thermopiles*. in *Solid State Sensors and Actuators, 1997. TRANSDUCERS '97 Chicago., 1997 International Conference on*. 1997.

- [43] Conway, A., et al., *Dispersion of a nanoliter bolus in microfluidic co-flow*. Journal of Micromechanics and Microengineering, 2014. **24**(3): p. 034006.
- [44] Sen, M.A., et al., *A continuous flow microfluidic calorimeter: 3-D numerical modeling with aqueous reactants*. Thermochemica Acta, 2015. **603**: p. 184-196.
- [45] Ott, J., et al., *Excess enthalpies for (ethanol+ water) at 298.15 K and pressures of 0.4, 5, 10, and 15 MPa*. The Journal of Chemical Thermodynamics, 1986. **18**(1): p. 1-12.
- [46] Rodríguez de Rivera, M., F. Socorro, and J.S. Matos, *Heats of mixing using an isothermal titration calorimeter: associated thermal effects*. International journal of molecular sciences, 2009. **10**(7): p. 2911-2920.
- [47] Padovani, R., *Thermal microsensors for in vitro and in vivo monitoring of chemical and biological processes*. 2016.
- [48] Modaresifar, M. and G.J. Kowalski, *Microscale calorimetric device for determining reaction parameters*. Thermochemica Acta, 2017.
- [49] Li, R., et al., *Mesoscopic Structuring and Dynamics of Alcohol/Water Solutions Probed by Terahertz Time-Domain Spectroscopy and Pulsed Field Gradient Nuclear Magnetic Resonance*. The Journal of Physical Chemistry B, 2014. **118**(34): p. 10156-10166.
- [50] Peeters, D. and P. Huyskens, *Endothermicity or exothermicity of water/alcohol mixtures*. Journal of molecular structure, 1993. **300**: p. 539-550.
- [51] Pješčić, I., et al., *Glass-composite prototyping for flow PCR with in situ DNA analysis*. Biomedical Microdevices, 2010. **12**(2): p. 333-343.
- [52] Fluent, Ansys., *12.0 User's guide*. Ansys Inc, 2009.
- [53] Orsi, G., et al., *Water-ethanol mixing in T-shaped microdevices*. Chemical Engineering Science, 2013. **95**: p. 174-183.
- [54] Boyne, J. and A.G. Williamson, *Enthalpies of mixture of ethanol and water at 25. degree. C*. Journal of Chemical and Engineering Data, 1967. **12**(3): p. 318-318.
- [55] Bothe, D., A. Lojewski, and H.-J. Warnecke, *Fully resolved numerical simulation of reactive mixing in a T-shaped micromixer using parabolized species equations*. Chemical Engineering Science, 2011. **66**(24): p. 6424-6440.
- [56] Capretto, L., et al., *Micromixing Within Microfluidic Devices*, in *Microfluidics: Technologies and Applications*, B. Lin, Editor. 2011, Springer Berlin Heidelberg: Berlin, Heidelberg. p. 27-68.

- [57] Hossain, S. and K.-Y. Kim, *Mixing Performance of a Serpentine Micromixer with Non-Aligned Inputs*. *Micromachines*, 2015. **6**(7): p. 842.
- [58] Wang, C.-T. and Y.-C. Hu, *Mixing of Liquids Using Obstacles in Y-Type Microchannels*. Vol. 13. 2010. 385-394.
- [59] Kamholz, A.E., et al., *Quantitative Analysis of Molecular Interaction in a Microfluidic Channel: The T-Sensor*. *Analytical Chemistry*, 1999. **71**(23): p. 5340-5347.
- [60] Salmon, J.-B., et al., *An Approach To Extract Rate Constants from Reaction–Diffusion Dynamics in a Microchannel*. *Analytical Chemistry*, 2005. **77**(11): p. 3417-3424.
- [61] Zhao, C.-X., et al., *Nanoparticle synthesis in microreactors*. *Chemical Engineering Science*, 2011. **66**(7): p. 1463-1479.
- [62] Koppaarthi, L.V., M.S. Tangutooru, and J.E. Guilbeau, *Label Free Detection of L-Glutamate Using Microfluidic Based Thermal Biosensor*. *Bioengineering*, 2015. **2**(1).
- [63] Fletcher, P.D.I., S.J. Haswell, and X. Zhang, *Monitoring of chemical reactions within microreactors using an inverted Raman microscopic spectrometer*. *ELECTROPHORESIS*, 2003. **24**(18): p. 3239-3245.
- [64] Kakuta, N., et al., *Simultaneous imaging of temperature and concentration of ethanol–water mixtures in microchannel using near-infrared dual-wavelength absorption technique*. *Measurement Science and Technology*, 2016. **27**(11): p. 115401.
- [65] Osborn, J.L., et al., *Microfluidics without pumps: reinventing the T-sensor and H-filter in paper networks*. *Lab on a Chip*, 2010. **10**(20): p. 2659-2665.
- [66] Chen, J.M., T.-L. Horng, and W.Y. Tan, *Analysis and measurements of mixing in pressure-driven microchannel flow*. *Microfluidics and Nanofluidics*, 2006. **2**(6): p. 455-469.
- [67] Gobby, D., P. Angeli, and A. Gavriilidis, *Mixing characteristics of T-type microfluidic mixers*. *Journal of Micromechanics and Microengineering*, 2001. **11**(2): p. 126.
- [68] Xu, B., et al., *Thermal mixing of two miscible fluids in a T-shaped microchannel*. *Biomicrofluidics*, 2010. **4**(4): p. 044102.
- [69] Pradere, C., et al., *Processing of temperature field in chemical microreactors with infrared thermography*. *Quantitative InfraRed Thermography Journal*, 2006. **3**(1): p. 117-135.
- [70] Pratt, K., *The mutual diffusion coefficient of ethanol–water mixtures: determination by a rapid, new method*. *Proceedings of the Royal*

- Society of London. A. Mathematical and Physical Sciences, 1974. **336**(1606): p. 393.
- [71] Price, W.S., H. Ide, and Y. Arata, *Solution Dynamics in Aqueous Monohydric Alcohol Systems*. The Journal of Physical Chemistry A, 2003. **107**(24): p. 4784-4789.
- [72] Ghoraishi, M., et al., *Clustering mechanism of ethanol-water mixtures investigated with photothermal microfluidic cantilever deflection spectroscopy*. Scientific reports, 2016. **6**: p. 23966.
- [73] Larkin, J., *Thermodynamic properties of aqueous non-electrolyte mixtures I. Excess enthalpy for water+ ethanol at 298.15 to 383.15 K*. The Journal of Chemical Thermodynamics, 1975. **7**(2): p. 137-148.
- [74] Nedić, M., et al., *A combined Raman- and infrared jet study of mixed methanol–water and ethanol–water clusters*. Physical Chemistry Chemical Physics, 2011. **13**(31): p. 14050-14063.
- [75] Thomas, S., R.L. Orozco, and T. Ameen, *Thermal gradient continuous-flow PCR: a guide to design*. Microfluidics and nanofluidics, 2014. **17**(6): p. 1039-1051.
- [76] Li, S., et al., *A Continuous-Flow Polymerase Chain Reaction Microchip With Regional Velocity Control*. Journal of microelectromechanical systems : a joint IEEE and ASME publication on microstructures, microactuators, microsensors, and microsystems, 2006. **15**(1): p. 223-236.
- [77] Pješčić, I., et al., *Glass-composite prototyping for flow PCR with in situ DNA analysis*. Biomedical microdevices, 2010. **12**(2): p. 333-343.
- [78] Crews, N., C. Wittwer, and B. Gale, *Continuous-flow thermal gradient PCR*. Biomedical microdevices, 2008. **10**(2): p. 187-195.
- [79] Aminuddin, M. and S.M. Zubair, *Analytical solutions to counter-flow heat exchanger subjected to external heat flux and axial conduction*. International Journal of Refrigeration, 2017. **74**: p. 22-37.
- [80] C. Jaeger, R., *Introduction to Microelectronic Fabrication / R.C. Jaeger*. 2018.
- [81] Patwa, R., et al. *Laser drilling up to 15,000 holes/sec in silicon wafer for PV solar cells*. in *SPIE Solar Energy + Technology*. 2013. SPIE.
- [82] Gosálvez, M.A., I. Zubel, and E. Viinikka, *Chapter 22 - Wet Etching of Silicon*, in *Handbook of Silicon Based MEMS Materials and Technologies (Second Edition)*, M. Tilli, et al., Editors. 2015, William Andrew Publishing: Boston. p. 470-502.
- [83] Iliescu, C., et al., *A practical guide for the fabrication of microfluidic devices using glass and silicon*. Biomicrofluidics, 2012. **6**(1): p. 016505.

- [84] Jaeger, R.C. *Introduction to microelectronic fabrication*. Upper Saddle River, N.J.: Prentice Hall.
- [85] Palik, E.D., et al., *Etching roughness for (100) silicon surfaces in aqueous KOH*. *Journal of Applied Physics*, 1991. **70**(6): p. 3291-3300.
- [86] Yang, C.-R., et al., *Effects of various ion-typed surfactants on silicon anisotropic etching properties in KOH and TMAH solutions*. *Sensors and Actuators A: Physical*, 2005. **119**(1): p. 271-281.
- [87] Kandlikar, S.G., *Chapter 3 - Single-phase liquid flow in minichannels and microchannels*, in *Heat Transfer and Fluid Flow in Minichannels and Microchannels*, S.G. Kandlikar, et al., Editors. 2006, Elsevier Science Ltd: Oxford. p. 87-136.
- [88] Becker, H. and C. Gärtner, *Polymer microfabrication technologies for microfluidic systems*. *Analytical and Bioanalytical Chemistry*, 2008. **390**(1): p. 89-111.
- [89] Lapadatu, A.C. and H. Jakobsen, *Chapter 30 - Anodic Bonding*, in *Handbook of Silicon Based MEMS Materials and Technologies (Second Edition)*, M. Tilli, et al., Editors. 2015, William Andrew Publishing: Boston. p. 599-610.
- [90] Dragoi, V., et al., *Triple-stack anodic bonding for MEMS applications*. Vol. 19. 2003.
- [91] Iliescu, C., et al., *Fabrication of a dielectrophoretic chip with 3D silicon electrodes*. Vol. 15. 2005. 494-500.
- [92] Cunningham, S.J. and M. Kupnik, *Wafer Bonding*, in *MEMS Materials and Processes Handbook*, R. Ghodssi and P. Lin, Editors. 2011, Springer US: Boston, MA. p. 817-877.
- [93] Iannacci, J., *Low Temperature Wafer Level Packaging of RF-MEMS Using SU-8 Contact Printing*. 2006. 55-56.
- [94] Lima, R.S., et al., *Sacrificial adhesive bonding: a powerful method for fabrication of glass microchips*. *Scientific Reports*, 2015. **5**: p. 13276.
- [95] Liming, Y., et al., *Adhesive bonding with SU-8 at wafer level for microfluidic devices*. *Journal of Physics: Conference Series*, 2006. **34**(1): p. 776.
- [96] Das, S.K., et al., *A microfluidic platform for studying the effects of small temperature gradients in an incubator environment*. *Biomicrofluidics*, 2008. **2**(3): p. 034106.
- [97] Chen, J.J., C.M. Shen, and Y.W. Ko, *Analytical study of a microfluidic DNA amplification chip using water cooling effect*. *Biomedical Microdevices*, 2013. **15**(2): p. 261-278.
- [98] Hajmohammadi, M.R., S.S. Nourazar, and A.H. Manesh, *Semi-analytical treatments of conjugate heat transfer*. *Proceedings of the*

- Institution of Mechanical Engineers, Part C: Journal of Mechanical Engineering Science, 2012. **227**(3): p. 492-503.
- [99] Liu, D. and S.V. Garimella, *Analysis and Optimization of the Thermal Performance of Microchannel Heat Sinks*. 2003(36908b): p. 557-565.
- [100] Wang, C., et al., *Room-temperature direct bonding of silicon and quartz glass wafers*. Applied Physics Letters, 2017. **110**(22): p. 221602.
- [101] Tanaka, H., et al., *Fast etching of silicon with a smooth surface in high temperature ranges near the boiling point of KOH solution*. Sensors and Actuators A: Physical, 2004. **114**(2): p. 516-520.